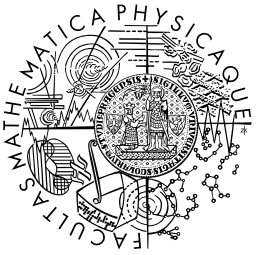

FACULTY
OF MATHEMATICS
AND PHYSICS
Charles University

MASTER THESIS

Bc. Lenka Košárková

Modelling of flow in the aortic root

Mathematical Institute of Charles University

Supervisor of the master thesis: RNDr. Jaroslav Hron, Ph.D.

Study programme: Mathematical Modelling in Physics and Technology

Study branch: Mathematical Modelling in Physics and Technology

Prague 2024

I declare that I carried out this master thesis independently, and only with the cited sources, literature and other professional sources. It has not been used to obtain another or the same degree.

I understand that my work relates to the rights and obligations under the Act No. 121/2000 Sb., the Copyright Act, as amended, in particular the fact that the Charles University has the right to conclude a license agreement on the use of this work as a school work pursuant to Section 60 subsection 1 of the Copyright Act.

In ..... date ....

Author's signature

I would like to thank my supervisor RNDr. Jaroslav Hron, Ph.D. for his time and patience and help with the numerical implementation of scripts. I would also like to thank to my consultant prof. RNDr. Josef Málek, CSc., DSc. for introducing me to the analytical part of this thesis.

Title: Modelling of flow in the aortic root

Author: Bc. Lenka Košárková

Department: Mathematical Institute of Charles University

Supervisor: RNDr. Jaroslav Hron, Ph.D., Mathematical Institute of Charles University

Abstract: Three-dimensional unsteady Navier-Stokes equations of an incompressible Navier–Stokes fluid in tube containing a sinusoidal extension is used for modelling the flow in the aortic root. Firstly, the proof of the existence of the weak solution is provided. The main aim of this thesis is to understand the formation of vortices and other flow characteristics such as dissipation, vorticity, wall shear stress and pressure drop. We extend the results presented in Chabionik et al. (2022) International Journal of Engineering Science, 180(103749) by focusing on three following aspects. The first is to use the extension with three sinuses describing a more realistic aortic root geometry. The second aspect is to approximate the boundary of the discretised computational domain by piecewise higher order polynomials to better capture the imposed boundary conditions. Thirdly, we discuss the choice of the finite element discretisations such as Taylor-Hood element and Brezzi-Douglas-Marini element. For all these aspects we investigate the character of the solutions and how the flow characteristics changes with the allowed slip at the wall.

Keywords: blood flow, FEM, Navier-Stokes, slip boundary condition

Contents

Introduction

Right after the oxygenated blood exits the left ventricle through the aortic valve it enters the aorta, including a region known as the Sinus of Valsalva, consisting of three so called sinuses. The flow in this region was already studied by Leonardo Da Vinci, who made two conjectures, see [6]. Firstly, through experiments involving an artificial glass model of the aortic root, he observed the formation of vortices in this area. Secondly, he believed that these vortices play a crucial role in the proper functioning of the aortic valve, which is underneath. The first of da Vinci's conjectures is supported by general observations. However the second conjecture is not truly valid. It was demonstrated that the straight artificial aortic root without any sinus extensions can function normally, even for longer period (above 15 years). However further experiments, see [15], showed that the real shape of the aortic root with three sinuses has some effects on the aortic valve. Specifically, the three leaflets of the aortic valve can close more smoothly, and the stresses acting on them are lower compared to a straight aortic root without these sinuses. Moreover, aortic root is also a critical space for formation of sclerosis.

This thesis follows the articles [9] and [10]. Their aim is to investigate flow in the aortic root and to understand the formation of vortices and other flow characteristics such as dissipation, vorticity, wall shear stress and pressure drop. They start from the most simplified case and then step by step add some modification, which can be of many types. For each modification they investigate the character of the solutions. At first, [9] investigated incompressible Navier-Stokes fluid in a tube with Navier's slip boundary condition imposed on impermeable wall. Because the analytical solution for this problem is known, the simplified geometry serves as a benchmark test to select numerical methods for their developed computational code. With knowledge of these suitable numerical methods, [10] focus on computing the blood flow in geometry with sinus extension, but only axially symmetric one. An interesting results show the importance of the choice of the Navier's slip parameter, enabling slip of the fluid on the wall also with the limiting cases (no-slip on the one side and perfect slip on the other side). Therefore we also take into account in our model this assumption of more general boundary condition, rather than traditional assumption that the blood adheres to the wall and exhibits the no-slip.

This thesis is divided into two parts, analytical and numerical. In the first analytical part we provide a detailed proof of the existence of the weak solution to the initial-boundary-value problem of unsteady three-dimensional flows in domain typical for the aortic root.

The second part concentrates on numerical and computational aspects. We follow the above mentioned approach in [9], [10], and we focus on three following extensions. The first is to use the domain with three sinuses describing a more realistic aortic root geometry. Further, we study the influence of the boundary of the discretised computational domain approximated by piecewise higher order polynomials to better capture the imposed boundary conditions. And thirdly, concerning discretisation in space, we also study pros and cons using the $\mathbf{H}(\mathrm{div}, \Omega)$-conforming finite elements with comparison to Taylor-Hood finite element. Our objective is to investigate how significant effect these modifications can have on all flow characteristics analysed in the earlier studies [10], [9]. The main goal is to deduce if these

modifications have a significant effect on the flow and whether they should be taken into account or neglected for further investigation of the flows in the aortic root. To do all these steps, we have implemented several scripts: for generating the geometry of the aortic root, for computing flows in such regions and also for providing post-process manipulations to obtain numerical simulations and convergence graphs for final comparisons.

1. Description of the problem

1.1 The initial-boundary-value-problem (IBVP)

We investigate the three-dimensional unsteady flows of the incompressible homogeneous Navier-Stokes fluid over the time interval $(0,T)$ flowing in set Ω.
We assume that $\Omega \subset \mathbb{R}^3$ is an open bounded connected set with Lipschitz continuous boundary, i.e. $\Omega \in C^{0,1}$. The boundary $\partial\Omega$ of the flow domain is split into three non-overlapping parts, the inlet Γ_{in}, outlet Γ_{out} and wall Γ_{wall}, see Figure 1.1. Such sketch of the domain is motivated by the geometry of the aortic root. The precise description of the shape of the aortic root will be discussed in section 3.3.
We look for the unknown velocity $\mathbf{v} : (0,T) \times \Omega \to \mathbb{R}^3$ and the pressure $p : (0,T) \times \Omega \to \mathbb{R}$, satisfying the equations

$$\operatorname{div} \mathbf{v} = 0 \qquad \text{in } (0,T) \times \Omega, \tag{1.1}$$

$$\rho_* \frac{\partial \mathbf{v}}{\partial t} + \rho_* (\nabla \mathbf{v})\, \mathbf{v} = \operatorname{div} \mathbb{T} \qquad \text{in } (0,T) \times \Omega, \tag{1.2}$$

$$\mathbb{T} = -p\mathbb{I} + \mu_* \left(\nabla \mathbf{v} + \nabla \mathbf{v}^T \right) \qquad \text{in } (0,T) \times \Omega, \tag{1.3}$$

together with initial and boundary conditions

$$\mathbf{v}(0,\cdot) = \mathbf{v}_0 \qquad \text{in } \Omega, \tag{1.4}$$

$$\mathbf{v} = \mathbf{v}_{\text{in}} \qquad \text{on } (0,T) \times \Gamma_{\text{in}}, \tag{1.5}$$

$$\mathbb{T}\mathbf{n} = -P\mathbf{n} + \frac{1}{2}\rho_* (\mathbf{v} \cdot \mathbf{n})_- \mathbf{v} \qquad \text{on } (0,T) \times \Gamma_{\text{out}}, \tag{1.6}$$

$$\mathbf{v} \cdot \mathbf{n} = 0 \qquad \text{on } (0,T) \times \Gamma_{\text{wall}}, \tag{1.7}$$

$$\theta \mathbf{v}_\tau + \gamma_* (1-\theta) \left(\mathbb{T}\mathbf{n}\right)_\tau = \mathbf{0} \qquad \text{on } (0,T) \times \Gamma_{\text{wall}}, \tag{1.8}$$

for given functions $\mathbf{v}_0$, $\mathbf{v}_{\text{in}}$ and P with properties specified later. Here $\theta \in [0,1]$, $\gamma_* \in (0,\infty)$, $\mathbf{n}$ is a unit normal vector at the boundary and for arbitrary $x \in \mathbb{R}$, $x_- = \min\{0,x\}$, $x_+ = \max\{0,x\}$, hence $x = x_+ + x_-$. The arbitrary vector $\mathbf{z} \in \mathbb{R}^3$ can be decomposed into the normal and tangential direction $\mathbf{z} = \mathbf{z}_\mathbf{n} + \mathbf{z}_\tau$, where $\mathbf{z}_\mathbf{n} = (\mathbf{z} \cdot \mathbf{n})\mathbf{n}$.
The governing equations consist of the incompressibility condition (1.1), of the balance of linear momentum (1.2) with constant density ρ_* and without considering external body forces acting on Ω and of the constitutive relation for the Navier-Stokes fluid (1.3), where $\mu_* > 0$ is a given constant dynamic viscosity. Now we provide more comments on each initial and boundary condition in (1.4)-(1.8).

The initial condition

We prescribe general initial condition $\mathbf{v}_0 : \Omega \to \mathbb{R}^3$, however for numerical computations we start from zero solution, i.e. we set $\mathbf{v}_0 = 0$.

Inflow boundary condition

On the inlet Γ_{in} the Dirichlet boundary condition is prescribed generally as $\mathbf{v}\big|_{\Gamma_{\text{in}}} = \mathbf{v}_{\text{in}} : [0,T] \times \Gamma_{\text{in}} \to \mathbb{R}^3$. In our problem $\mathbf{v}_{\text{in}}$ represents the only term generating

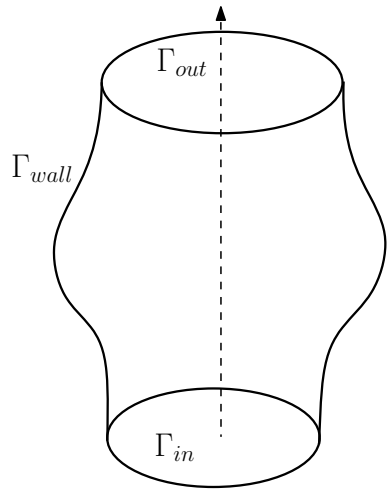

Figure 1.1: Computational domain

the flow. As our domain, motivated by shape of the aortic root, starts from almost narrow tube (see Figure 1.1), it makes sense to consider the parabolic velocity profile on inflow, that would evolve from the Poiseuille flow in infinite tube. Such idea is used in [10], where the flow is driven by gradually increasing parabolic profile, imposed on the inflow. Specifically, the time-dependent inflow $\mathbf{v}_{\text{in}}$ starts from zero and increases to one second to the parabolic profile with set mean inflow velocity, which then remains for the rest of the time. We will proceed in the same manner in our computations with the exact formulation for the inflow $\mathbf{v}_{\text{in}}$ provided in section 4.2.

Outflow boundary condition

For problems with outflow, the artificial boundary need to be set. The condition on this artificial boundary should be chosen to have good mathematical properties and also to have some physical interpretation. One of the most common is the so called *do-nothing* condition $(\nabla \mathbf{v})\mathbf{n}|_{\Gamma_{\text{out}}} = 0$ or similarly the *constant traction* condition $\mathbb{T}\mathbf{n}|_{\Gamma_{\text{out}}} = 0$, representing no forces acting on the outlet. Both of these condition are also often used with some prescribed function b on the right hand side. However for such conditions on the outlet, it is known, that the energy estimates for the weak solution can not be guaranteed and some smallness condition on the data has to be imposed to perform the PDE analysis, see [28]. Moreover in the article [25], the numerical results also shows that for some cases (here with two outlets) there exist multiple solutions for the stationary Navier-Stokes equations in three dimensions, where the uniqueness/non-uniqueness is not yet proven analytically. We thus modify this condition, despite the fact that the *do-nothing* or *constant traction* conditions are still often used in many computations, where giving reliable results.
Therefore, in this thesis we prescribe the force acting on the outlet generally as some prescribed pressure $P : [0, T] \to \mathbb{R}$ times the normal, plus specific non-linear correction $\frac{1}{2}\rho_* (\mathbf{v} \cdot \mathbf{n})_- \mathbf{v}$. In numerical computations we consider $P = 0$, but it does not limit applicability of the method for general outflow pressure. The additional non-linear term is necessary, since in the energy estimates it cancels out with the negative part of the convective term on the outlet Γ_{out}, which generally doesn't have to be under control. Hence with the additional term we can get the boundedness of

the energy of the whole system. This problematic is in more detail described in the article [28], where they also show the improvement of numerical properties for such condition. Note that for problems with pure outflow, $(\mathbf{v}\cdot\mathbf{n})_-\big|_{\Gamma_{\text{out}}} = 0$ and the term $\frac{1}{2}\rho_*\,(\mathbf{v}\cdot\mathbf{n})_-\,\mathbf{v}$ vanishes.

The impermeability condition

The impermeability condition is imposed on the boundary Γ_{wall} and is natural condition for our problem. It says no fluid can go through, thus we get the constraint for the normal velocity component as

$$\mathbf{v}\cdot\mathbf{n}\Big|_{\Gamma_{\text{wall}}} = 0.$$

Navier's slip boundary condition

Navier's slip boundary condition enables the fluid to slip on the wall. It is defined that the tangential velocity at the wall is proportional to the tangent force acting on the boundary. It can be written as

$$\theta\mathbf{v}_\tau + \gamma_*(1-\theta)\,(\mathbb{T}\mathbf{n})_\tau\,\Big|_{\Gamma_{\text{wall}}} = \mathbf{0}, \tag{1.9}$$

where $\mathbf{n}$, $\boldsymbol{\tau}$ denotes the normal and tangential direction to the boundary Γ_{wall} respectively. Here $\theta \in (0,1)$ is non-dimensional weight, representing all possible values of slip on the wall. It can be also extend for the limiting cases to no-slip with $\theta = 1$ and free slip with $\theta = 0$. Further in this thesis, we will refer to the Navier's slip condition as (1.9) with $\theta \in [0,1]$. Value $\gamma_* \in (0,\infty)$ is the slip parameter.

1.2 Weak formulation

First, let us define notation for Sobolev function spaces and some other basic notation, that we will frequently use. Firstly,

$$\mathbf{V} := \mathbf{W}^{1,2}(\Omega)\left(= \mathbf{H}^1(\Omega)\right) \tag{1.10}$$

$$\tilde{\mathbf{V}} := \mathbf{W}^{1,2}_{\text{div, bc}}(\Omega) := \{\boldsymbol{\phi}\in\mathbf{V};\ \operatorname{div}\boldsymbol{\phi} = 0,\ \boldsymbol{\phi} = \mathbf{0} \text{ on } \Gamma_{\text{in}},\ \boldsymbol{\phi}\cdot\mathbf{n} = 0 \text{ on } \Gamma_{\text{wall}}\}\,. \tag{1.11}$$

Bold symbols $\mathbf{W}^{k,p}(\Omega)$, $\mathbf{L}^p(\Omega)$ denote vector-valued Sobolev and Lebesgue spaces respectively. Further $(\cdot,\cdot)$ is the L^2 inner product in Ω and $\langle\cdot,\cdot\rangle := \langle\cdot,\cdot\rangle_{X^*,X}$ is the duality between space X and its dual space X^*. Scalar product for tensors is denoted as $\mathbb{A} : \mathbb{B} = \sum_{i,j=1}^3 A_{ij}B_{ij}$. Also, later, we will need space $\mathbf{L}^2_{0,\text{div}}(\Omega)$, which can be characterised as

$$\mathbf{L}^2_{0,\text{div}}(\Omega) = \overline{\{\mathbf{v}\in\mathbf{C}_0^\infty(\Omega);\operatorname{div}\mathbf{v}=0\}}^{\|\cdot\|_{L^2}}. \tag{1.12}$$

To pass to the weak formulation, we integrate (1.2) over Ω and test by function $\boldsymbol{\phi}\in\tilde{\mathbf{V}}$. Hence we have

$$\rho_*\left\langle\frac{\partial\mathbf{v}}{\partial t},\boldsymbol{\phi}\right\rangle + \rho_*\int_\Omega(\nabla\,\mathbf{v})\,\mathbf{v}\cdot\boldsymbol{\phi}\,\mathrm{d}x = \int_\Omega \operatorname{div}\mathbb{T}\cdot\boldsymbol{\phi}\,\mathrm{d}x,$$

where we replaced the scalar product in the first term by duality. Applying integration by parts on the right hand side yields to

$$\int_\Omega \operatorname{div} \mathbb{T} \cdot \boldsymbol{\phi} \, \mathrm{d}x = \int_{\partial\Omega} \mathbb{T}\mathbf{n} \cdot \boldsymbol{\phi} \, \mathrm{d}S - \int_\Omega \mathbb{T} : \nabla \boldsymbol{\phi} \, \mathrm{d}x = \int_{\partial\Omega} \mathbb{T}\mathbf{n} \cdot \boldsymbol{\phi} \, \mathrm{d}S - \int_\Omega \mathbb{T} : \mathbb{D}(\boldsymbol{\phi}) \, \mathrm{d}x,$$

using $\mathbb{T} : \nabla \boldsymbol{\phi} = \mathbb{T} : \mathbb{D}(\boldsymbol{\phi})$ due to the symmetry of $\mathbb{T}$. Terms on the boundary can be separated as follows

$$\begin{aligned}\int_{\partial\Omega} \mathbb{T}\mathbf{n} \cdot \boldsymbol{\phi} \, \mathrm{d}S &= \int_{\Gamma_{\mathrm{in}} \cap \Gamma_{\mathrm{out}}} \mathbb{T}\mathbf{n} \cdot \boldsymbol{\phi} \mathrm{d}S + \int_{\Gamma_{\mathrm{wall}}} (\mathbb{T}\mathbf{n})_n \cdot \boldsymbol{\phi}_n \, \mathrm{d}S + \int_{\Gamma_{\mathrm{wall}}} (\mathbb{T}\mathbf{n})_\tau \cdot \boldsymbol{\phi}_\tau \, \mathrm{d}S \\ &= \int_{\Gamma_{\mathrm{out}}} \mathbb{T}\mathbf{n} \cdot \boldsymbol{\phi} \, \mathrm{d}S + \int_{\Gamma_{\mathrm{wall}}} (\mathbb{T}\mathbf{n})_\tau \cdot \boldsymbol{\phi}_\tau \, \mathrm{d}S,\end{aligned}$$

where the last identity follows from $\boldsymbol{\phi} \in \tilde{\mathbf{V}}$.
Now applying the constitutive relation (1.3), we get $\mathbb{T} : \mathbb{D}(\boldsymbol{\phi}) = (-p\mathbb{I} + 2\mu_* \mathbb{D}(\mathbf{v})) : \mathbb{D}(\boldsymbol{\phi}) = -p \operatorname{div} \boldsymbol{\phi} + 2\mu_* \mathbb{D}(\mathbf{v}) : \mathbb{D}(\boldsymbol{\phi}) = 2\mu_* \mathbb{D}(\mathbf{v}) : \mathbb{D}(\boldsymbol{\phi})$, due to $\operatorname{div} \boldsymbol{\phi} = 0$. Using outflow condition (1.6) on Γ_{out} and Navier's slip condition (1.8) on Γ_{wall}, we can finally get

$$\begin{aligned}&\rho_* \left\langle \frac{\partial \mathbf{v}}{\partial t}, \boldsymbol{\phi} \right\rangle + \rho_* \int_\Omega (\nabla \mathbf{v}) \, \mathbf{v} \cdot \boldsymbol{\phi} \, \mathrm{d}x + 2\mu_* \int_\Omega \mathbb{D}(\mathbf{v}) \cdot \mathbb{D}(\boldsymbol{\phi}) \, \mathrm{d}x \\ &+ \frac{\theta}{\gamma_*(1-\theta)} \int_{\Gamma_{\mathrm{wall}}} \mathbf{v}_\tau \cdot \boldsymbol{\phi}_\tau \, \mathrm{d}S = -P(t) \int_{\Gamma_{\mathrm{out}}} \boldsymbol{\phi} \cdot \mathbf{n} \, \mathrm{d}S + \int_{\Gamma_{\mathrm{out}}} \frac{\rho_*}{2} (\mathbf{v} \cdot \mathbf{n})_- \mathbf{v} \cdot \boldsymbol{\phi} \, \mathrm{d}S,\end{aligned} \tag{1.13}$$

valid for all $\boldsymbol{\phi} \in \tilde{\mathbf{V}}$ and a.a. $t \in (0, T)$.
The incompressibility condition, which weak formulation reads

$$\int_\Omega -q \operatorname{div} \mathbf{v} \, \mathrm{d}x = 0 \quad \forall q \in L^2(\Omega), \tag{1.14}$$

is hidden in the space $\tilde{\mathbf{V}}$, where we look for the velocity $\mathbf{v}(t)$.

Requirements on $\mathbf{v}_{\mathrm{in}}$

For the analysis, we assume the existence of an extension $\mathbf{v}_{\mathrm{in}}^*$ of $\mathbf{v}_{\mathrm{in}}$, i.e. we require that there exists a continuous function $\mathbf{v}_{\mathrm{in}}^* : (0, T) \times \overline{\Omega} \to \mathbf{R}^3$, $\overline{\Omega}$ being the closure of Ω, such that

$$\begin{aligned}\operatorname{div} \mathbf{v}_{\mathrm{in}}^* &= 0 && \text{in } (0,T) \times \Omega, \\ \mathbf{v}_{\mathrm{in}}^* &= \mathbf{v}_{\mathrm{in}} && \text{on } \Gamma_{\mathrm{in}}, \\ \mathbf{v}_{\mathrm{in}}^* \cdot \mathbf{n} &= 0 && \text{on } \Gamma_{\mathrm{wall}}, \\ \mathbf{v}_{\mathrm{in}}^* &= \mathbf{0} && \text{on } \Gamma_{\mathrm{out}}, \\ \frac{\partial \mathbf{v}_{\mathrm{in}}^*}{\partial t} \in L^2((0,T) \times \Omega)^3 \quad &\text{and} \quad \nabla \mathbf{v}_{\mathrm{in}}^* \in L^\infty((0,T) \times \Omega)^{3\times 3}.\end{aligned} \tag{1.15}$$

Definition 1 (Weak solution)**.** *Let* $\Omega \in C^{0,1}$, $\mathbf{v}_0 \in \mathbf{L}^2_{0,\mathrm{div}}(\Omega)$ *and* $\mathbf{v}_{\mathrm{in}}$ *fulfils* (1.15)*. We say that* $\mathbf{v}$ *is a* weak solution *to* (1.1)-(1.8) *provided that*

$$\begin{aligned}\mathbf{v} - \mathbf{v}_{\mathrm{in}}^* &\in L^2(0, T; \tilde{\mathbf{V}}) \cap L^\infty(0, T; \mathbf{L}^2_{0,\mathrm{div}}(\Omega)), \\ \frac{\partial \mathbf{v}}{\partial t} &\in L^{\frac{4}{3}}(0, T; \tilde{\mathbf{V}}^\star), \\ \lim_{t \to 0+} \|\mathbf{v}(t, \cdot) - \mathbf{v}_0\|_{L^2} &= 0,\end{aligned} \tag{1.16}$$

satisfying the weak formulation (1.13) *for all* $\boldsymbol{\phi} \in \tilde{\mathbf{V}}$ *and a.a.* $t \in (0,T)$ *and satisfying the energy inequality*

$$
\begin{aligned}
&\frac{\rho_*}{2}\|(\mathbf{v}-\mathbf{v}_{\mathrm{in}}^*)(t,\cdot)\|^2_{\mathbf{L}^2(\Omega)} + 2\mu_* \int_0^t \|\mathbb{D}(\mathbf{v}-\mathbf{v}_{\mathrm{in}}^*)\|^2_{\mathbf{L}^2(\Omega)}\,\mathrm{d}s \\
&+ \frac{\theta}{\gamma_*(1-\theta)}\int_0^t \int_{\Gamma_{\mathrm{wall}}} |\mathbf{v}_\tau|^2\,\mathrm{d}S\,\mathrm{d}s + \int_0^t \int_{\Gamma_{\mathrm{out}}} \frac{|\mathbf{v}|^2}{2}(\mathbf{v}\cdot\mathbf{n})_+\,\mathrm{d}S\,\mathrm{d}s \\
&\le \frac{\rho_*}{2}\|\mathbf{v}_0-\mathbf{v}_{\mathrm{in}}^*(0)\|^2_{\mathbf{L}^2(\Omega)} + \frac{\theta}{\gamma_*(1-\theta)}\int_0^t \int_{\Gamma_{\mathrm{wall}}} \mathbf{v}_\tau\cdot(\mathbf{v}_{\mathrm{in}}^*)_\tau\,\mathrm{d}S\,\mathrm{d}s \\
&- \int_0^t \int_\Omega \rho_*(\mathbf{v}-\mathbf{v}_{\mathrm{in}}^*)\otimes(\mathbf{v}-\mathbf{v}_{\mathrm{in}}^*) : \nabla \mathbf{v}_{\mathrm{in}}^*\,\mathrm{d}x\,\mathrm{d}s \\
&+ \int_0^t \int_\Omega \rho_*(\mathbf{v}_{\mathrm{in}}^*\otimes\mathbf{v}_{\mathrm{in}}^*) : \mathbb{D}(\mathbf{v}-\mathbf{v}_{\mathrm{in}}^*)\,\mathrm{d}x\,\mathrm{d}s - \int_0^t \int_\Omega \rho_* \frac{\partial \mathbf{v}_{\mathrm{in}}^*}{\partial t}\cdot(\mathbf{v}-\mathbf{v}_{\mathrm{in}}^*)\,\mathrm{d}x\,\mathrm{d}s \\
&- P(t)\int_0^t \int_{\Gamma_{\mathrm{in}}} \mathbf{v}\cdot\mathbf{n}\,\mathrm{d}S\,\mathrm{d}s - 2\mu_*\int_0^t \int_\Omega \mathbb{D}(\mathbf{v}_{\mathrm{in}}^*) : \mathbb{D}(\mathbf{v}-\mathbf{v}_{\mathrm{in}}^*)\,\mathrm{d}x\,\mathrm{d}s,
\end{aligned}
\tag{1.17}
$$

for a.a. $t \in (0,T)$.

2. Existence of the weak solution of IBVP

Nowadays the results and proofs of existence of the weak solution for internal three-dimensional unsteady Navier-Stokes equations with Dirichlet boundary condition are provided in many textbooks for example in [35], [36] and are also available in lecture notes [31]. The existence theory considering also Navier's slip boundary condition seems to be firstly analysed in [26], where more complex fluids were considered, or see also [4]. To our knowledge, first results with general outflow conditions on artificial boundaries are established in [7]. The existence including the outflow condition in a form (1.6), is stated in [28], but without a detailed proof.
In this thesis, we provide a detailed proof for the specific problem (1.1)-(1.6), containing non-homogeneous inflow Dirichlet boundary condition, Navier's slip boundary condition and outflow boundary condition in form (1.6), on different parts of the boundary. The existential theorem is as follows.

Theorem 1. *Let $\Omega \in C^{0,1}$ be a bounded domain in $\mathbb{R}^3$, $\mathbf{v}_0 \in \mathbf{L}^2_{0,\mathrm{div}}(\Omega)$ and $\mathbf{v}_{\mathrm{in}}$ fulfils* (1.15) *and $0 < T < \infty$. Then there exists a weak solution defined in definition* (1).

This whole chapter covers the proof of the theorem (1). A priori energy estimates for velocity are established in the first section and rigorous proof of the existence of the weak solution is provided in the second section.

2.1 A priori energy estimates

A part of the energy estimates is already in detail provided in [9]. In summary, they formed a scalar product of (1.2) with $\mathbf{v} - \mathbf{v}^*_{\mathrm{in}}$, integrated over the domain Ω, used Gauss's theorem, incompressibility condition (1.1), boundary conditions (1.5)-(1.8), properties of $\mathbf{v}^*_{\mathrm{in}}$ and finally, integrated w.r.t. time over $(0,T)$, used Cauchy-Schwartz, Young and Hölder inequalities and Gronwall lemma to finally show that

$$\begin{aligned} &\rho_* \sup_{t\in[0,T]} \|(\mathbf{v}-\mathbf{v}^*_{\mathrm{in}})(t,\cdot)\|_2^2 + \mu_* \int_0^T \|\mathbb{D}(\mathbf{v}-\mathbf{v}^*_{\mathrm{in}})\|_2^2 \,\mathrm{d}t \\ &+ \frac{\theta}{\gamma_*(1-\theta)} \int_0^T \int_{\Gamma_{\mathrm{wall}}} |\mathbf{v}_\tau|^2 \,\mathrm{d}S\,\mathrm{d}t + \int_0^T \int_{\Gamma_{\mathrm{out}}} \rho_* |\mathbf{v}|^2 (\mathbf{v}\cdot\mathbf{n})_+ \,\mathrm{d}S\,\mathrm{d}t \\ &\leq C\left(T, \|\mathbf{v}_0 - \mathbf{v}^*_{\mathrm{in}}(0,\cdot)\|_2^2, C(\mathbf{v}^*_{\mathrm{in}})\right) < \infty, \end{aligned} \tag{2.1}$$

where the constant $C(\mathbf{v}^*_{\mathrm{in}})$ depends on ρ_*, μ_*, $\int_0^T \left\|\frac{\partial \mathbf{v}^*_{\mathrm{in}}}{\partial t}\right\|_2^2 \mathrm{d}s$, $\int_0^T \|\mathbb{D}(\mathbf{v}^*_{\mathrm{in}})\|_2^2 \,\mathrm{d}s$ and $\sup_{t\in(0,T)} \|\nabla \mathbf{v}^*_{\mathrm{in}}\|_\infty$ ans is finite due to the assumptions on $\mathbf{v}^*_{\mathrm{in}}$ stated in (1.15) [1].

[1] For clarity, let us just show how in [9] treat the convective term multiplied by $\mathbf{v} - \mathbf{v}^*_{\mathrm{in}}$:

$$\int_\Omega ((\nabla \mathbf{v})\mathbf{v})\cdot(\mathbf{v}-\mathbf{v}^*_{\mathrm{in}})\,\mathrm{d}x = \int_\Omega ((\mathbf{v}-\mathbf{v}^*_{\mathrm{in}})\otimes\mathbf{v}) : \nabla\mathbf{v}\,\mathrm{d}x = \int_\Omega ((\mathbf{v}-\mathbf{v}^*_{\mathrm{in}})\otimes\mathbf{v}) : \nabla(\mathbf{v}-\mathbf{v}^*_{\mathrm{in}})\,\mathrm{d}x$$
$$+ \int_\Omega ((\mathbf{v}-\mathbf{v}^*_{\mathrm{in}})\otimes\mathbf{v}) : \nabla\mathbf{v}^*_{\mathrm{in}}\,\mathrm{d}x = \int_\Omega \mathrm{div}\left(\frac{|\mathbf{v}-\mathbf{v}^*_{\mathrm{in}}|^2}{2}\mathbf{v}\right)\mathrm{d}x + \int_\Omega ((\mathbf{v}-\mathbf{v}^*_{\mathrm{in}})\otimes\mathbf{v}) : \nabla\mathbf{v}^*_{\mathrm{in}}\,\mathrm{d}x.$$

2.1.1 Function spaces for $\mathbf{v} - \mathbf{v}^*_{\text{in}}$

Specifically, (2.1) provides estimates

$$\sup_{t\in[0,T]} \|(\mathbf{v} - \mathbf{v}^*_{\text{in}})(t,\cdot)\|_2^2 < \infty, \tag{2.2}$$

$$\int_0^T \|\mathbb{D}(\mathbf{v} - \mathbf{v}^*_{\text{in}})\|_2^2 \,\mathrm{d}t < \infty, \tag{2.3}$$

$$\int_0^T \|\mathbf{v}_\tau\|^2_{\mathbf{L}^2(\Gamma_{\text{wall}})} \,\mathrm{d}t < \infty. \tag{2.4}$$

Then (2.3) and (2.2) respectively gives natural spaces for $\mathbf{v} - \mathbf{v}^*_{\text{in}}$ as

$$\mathbf{v} - \mathbf{v}^*_{\text{in}} \in L^2(0,T;\tilde{\mathbf{V}}), \tag{2.5}$$

$$\mathbf{v} - \mathbf{v}^*_{\text{in}} \in L^\infty(0,T;\mathbf{L}^2_{0,\text{div}}(\Omega)). \tag{2.6}$$

From the continuous embedding of Sobolev spaces in $\Omega \in C^{0,1}$, see [1], $\mathbf{W}^{1,2}(\Omega) \hookrightarrow \mathbf{L}^q(\Omega)$ for $q \le 6$ we get

$$\mathbf{v} - \mathbf{v}^*_{\text{in}} \in L^2(0,T;\mathbf{L}^q(\Omega)) \quad \text{ for } 1 \le q \le 6. \tag{2.7}$$

We shall show that for $s_2 \in [2,6]$ we also get the estimate

$$\mathbf{v} - \mathbf{v}^*_{\text{in}} \in L^{s_1}(0,T;\mathbf{L}^{s_2}(\Omega)) \quad \text{ for } s_2 = \frac{6s_1}{3s_1 - 4}. \tag{2.8}$$

Proof. By standard interpolation for Lebesgue spaces (coming from Hölder inequality), for $s \in [2,6]$, requiring $\frac{1}{s_2} = \frac{\lambda}{2} + \frac{1-\lambda}{6}$, with $\lambda \in [0,1]$, we have

$$\begin{aligned}\int_0^T \|\mathbf{v} - \mathbf{v}^*_{\text{in}}\|_{s_2}^{s_1} \,\mathrm{d}t &\le \int_0^T \|\mathbf{v} - \mathbf{v}^*_{\text{in}}\|_2^{\lambda s_1} \|\mathbf{v} - \mathbf{v}^*_{\text{in}}\|_6^{(1-\lambda)s_1} \,\mathrm{d}t \\ &\le \sup_{t\in[0,T]} \|(\mathbf{v} - \mathbf{v}^*_{\text{in}})(t,\cdot)\|_2^{\lambda s_1} \int_0^T \|\mathbf{v} - \mathbf{v}^*_{\text{in}}\|_6^{(1-\lambda)s_1} \,\mathrm{d}t.\end{aligned}$$

Due to (2.6), (2.7), the first term is finite and the second term is finite for $(1-\lambda)s_1 = 2$, thus together giving the constraint $s_2 = \frac{6s_1}{3s_1-4}$. □

In the first equality is used a little different notation and in last equality is applied the following observation: $\int_\Omega ((\mathbf{v} - \mathbf{v}^*_{\text{in}}) \otimes \mathbf{v}) : \nabla(\mathbf{v} - \mathbf{v}^*_{\text{in}}) \,\mathrm{d}x = \int_\Omega v_j \frac{\partial(v - v^*_{\text{in}})_i}{\partial x_j}(v - v^*_{\text{in}})_i \,\mathrm{d}x = \int_\Omega v_j \frac{1}{2} \frac{\partial |\mathbf{v} - \mathbf{v}^*_{\text{in}}|^2}{\partial x_j} \,\mathrm{d}x = \int_\Omega \operatorname{div}(\frac{|\mathbf{v} - \mathbf{v}^*_{\text{in}}|^2}{2}\mathbf{v}) \,\mathrm{d}x$, due to incompressibility condition (1.1). Further

$$\begin{aligned}&\int_\Omega \operatorname{div}\left(\frac{|\mathbf{v} - \mathbf{v}^*_{\text{in}}|^2}{2}\mathbf{v}\right) \mathrm{d}x + \int_\Omega ((\mathbf{v} - \mathbf{v}^*_{\text{in}}) \otimes \mathbf{v}) : \nabla \mathbf{v}^*_{\text{in}} \,\mathrm{d}x = \int_{\Gamma_{\text{out}}} \frac{|\mathbf{v} - \mathbf{v}^*_{\text{in}}|^2}{2}(\mathbf{v}\cdot\mathbf{n}) \,\mathrm{d}S + \\ &\int_\Omega ((\mathbf{v} - \mathbf{v}^*_{\text{in}}) \otimes (\mathbf{v} - \mathbf{v}^*_{\text{in}})) : \nabla \mathbf{v}^*_{\text{in}} \,\mathrm{d}x + \int_\Omega ((\mathbf{v} - \mathbf{v}^*_{\text{in}}) \otimes \mathbf{v}^*_{\text{in}}) : \nabla \mathbf{v}^*_{\text{in}} \,\mathrm{d}x \\ &= \int_{\Gamma_{\text{out}}} \frac{|\mathbf{v} - \mathbf{v}^*_{\text{in}}|^2}{2}(\mathbf{v}\cdot\mathbf{n}) \,\mathrm{d}S + \int_\Omega ((\mathbf{v} - \mathbf{v}^*_{\text{in}}) \otimes (\mathbf{v} - \mathbf{v}^*_{\text{in}})) : \nabla \mathbf{v}^*_{\text{in}} \,\mathrm{d}x - \\ &\int_\Omega (\mathbf{v}^*_{\text{in}} \otimes \mathbf{v}^*_{\text{in}}) : \nabla(\mathbf{v} - \mathbf{v}^*_{\text{in}}) \,\mathrm{d}x + \int_\Omega \operatorname{div}\left((\mathbf{v}^*_{\text{in}} \cdot (\mathbf{v} - \mathbf{v}^*_{\text{in}}))\mathbf{v}^*_{\text{in}}\right) \mathrm{d}x,\end{aligned}$$

using integration by parts in the last equality. Note that the last term vanishes due to properties of $\mathbf{v}^*_{\text{in}}$ in (1.15). Further, term on Γ_{out} can be written as $\int_{\Gamma_{\text{out}}} \frac{|\mathbf{v} - \mathbf{v}^*_{\text{in}}|^2}{2}(\mathbf{v}\cdot\mathbf{n}) \,\mathrm{d}S = \int_{\Gamma_{\text{out}}} \frac{|\mathbf{v}|^2}{2}(\mathbf{v}\cdot\mathbf{n}) \,\mathrm{d}S$ and its negative part cancels out with non-linear term of the outflow condition (1.6), which is the essential part for establishing the energy estimates.

Once we know (2.5), (2.6) and (2.8), we can also get (by considering $\mathbf{v} = \mathbf{v} - \mathbf{v}^*_{\text{in}} + \mathbf{v}^*_{\text{in}}$, using triangle inequality and properties of $\mathbf{v}^*_{\text{in}}$ stated in (1.15)) the estimates for $\mathbf{v}$ as

$$\mathbf{v} \in L^2(0,T;\tilde{\mathbf{V}}_{\mathbf{n}}), \tag{2.9}$$

$$\mathbf{v} \in L^\infty(0,T;\mathbf{L}^2_{0,\text{div}}(\Omega)), \tag{2.10}$$

$$\mathbf{v} \in L^{s_1}(0,T;\mathbf{L}^{s_2}(\Omega)) \quad \text{for } s_2 = \frac{6s_1}{3s_1-4},\ s_2 \in [2,6]. \tag{2.11}$$

With notation

$$\tilde{\mathbf{V}}_{\mathbf{n}} := \{\boldsymbol{\phi} \in \mathbf{V};\ \operatorname{div}\boldsymbol{\phi} = 0,\ \boldsymbol{\phi}\cdot\mathbf{n} = 0 \text{ on } \Gamma_{\text{wall}}\}. \tag{2.12}$$

Function spaces on Γ_{out}

For $\Omega \in C^{0,1}$, $p \in [1,\infty]$, $r \in \left(\frac{1}{p},1\right]$, there exist a continuous trace operator tr s.t.

$$\text{tr} : W^{r,p}(\Omega) \to W^{r-\frac{1}{p},p}(\partial\Omega), \tag{2.13}$$

see for example [1]. Also we have the following general embedding for $p \in [1,\infty]$ and $k \geq 0$

$$W^{k,p}(\partial\Omega) \hookrightarrow L^{\frac{dp}{d-pk}}(\partial\Omega) \quad \text{for } pk < d. \tag{2.14}$$

We shall show that for velocity $\mathbf{v}$ on Γ_{out} holds [2]

$$\mathbf{v} \in L^{\frac{8}{3}}(0,T;\mathbf{L}^{\frac{8}{3}}(\Gamma_{\text{out}})). \tag{2.15}$$

Proof. Denoting $s := \frac{dp}{d-pk} \geq 1$ and substituting $d = 2$ for surface $\partial\Omega$ and $p = 2$, we get $k = \frac{s-2}{s} < 1$. Hence for us, for $s \geq 2$

$$W^{\frac{s-2}{s},2}(\partial\Omega) \hookrightarrow L^s(\partial\Omega). \tag{2.16}$$

Together we get the estimate for velocity on Γ_{out} (for $p = 2$)

$$\begin{aligned}\int_0^T \|\text{tr }\mathbf{v}\|^s_{\mathbf{L}^s(\Gamma_{\text{out}})}\,\mathrm{d}t &\leq \int_0^T \|\text{tr }\mathbf{v}\|^s_{\mathbf{L}^s(\partial\Omega)}\,\mathrm{d}t \leq C\int_0^T \|\text{tr }\mathbf{v}\|^s_{\mathbf{W}^{\frac{s-2}{s},2}(\partial\Omega)}\,\mathrm{d}t \\ &\leq \tilde{C}\int_0^T \|\mathbf{v}\|^s_{\mathbf{W}^{\frac{3s-4}{2s},2}(\Omega)}\,\mathrm{d}t,\end{aligned} \tag{2.17}$$

where we use (2.16) in the second inequality. Last inequality is due to boundedness of the trace operator (2.13) for $r = \frac{3s-4}{2s}$, giving constrain $s \in (2,4]$. Here $\tilde{C}$ is the embedding constant times constant from boundedness of the trace operator.
The last term in (2.17) can be handled due to following interpolation, see [13], for $l \leq k$ as

$$\|v\|_{W^{l,2}(\Omega)} \leq \|v\|^{l/k}_{W^{1,2}(\Omega)}\|v\|^{1-l/k}_{L^2(\Omega)}. \tag{2.18}$$

In our case $l = \frac{3s-4}{2s}$. Thus using inequality above for $s \in (2,4]$ in (2.17) yields to

$$\begin{aligned}\int_0^T \|\text{tr }\mathbf{v}\|^s_{\mathbf{L}^s(\Gamma_{\text{out}})}\,\mathrm{d}t &\leq \tilde{C}\int_0^T \|\mathbf{v}\|^s_{\mathbf{W}^{\frac{3s-4}{2s},2}(\Omega)}\,\mathrm{d}t \leq \tilde{C}\int_0^T \|\mathbf{v}\|^{\frac{4-s}{2}}_{\mathbf{L}^2(\Omega)}\|\mathbf{v}\|^{\frac{3s-4}{2}}_{\mathbf{W}^{1,2}(\Omega)} \\ &\leq \tilde{C}\sup_{t\in[0,T]}\|\mathbf{v}(t,\cdot)\|^{\frac{4-s}{2}}_{\mathbf{L}^2(\Omega)}\int_0^T \|\mathbf{v}\|^{\frac{3s-4}{2}}_{\mathbf{W}^{1,2}(\Omega)} < \infty,\end{aligned}$$

due to (2.9) and (2.10) for $\frac{3s-4}{2} = 2$, i.e. $s = \frac{8}{3}$. □

[2] Note that from (1.15), $\mathbf{v}^*_{\text{in}} = 0$ on Γ_{out}.

2.1.2 Function space for $\frac{\partial \mathbf{v}}{\partial t}$

We shall show that holds

$$\frac{\partial \mathbf{v}}{\partial t} \in L^{\frac{4}{3}}\left(0,T;(\tilde{\mathbf{V}})^\star\right). \tag{2.19}$$

Proof. Firstly, the convective term $\rho_* \int_\Omega (\nabla \mathbf{v})\mathbf{v}\cdot\boldsymbol{\phi}\,\mathrm{d}x$ can be treated as (using Gauss's theorem and boundary condition (1.7) for $\mathbf{v}$)

$$\rho_* \int_\Omega (\nabla \mathbf{v})\mathbf{v}\cdot\boldsymbol{\phi}\,\mathrm{d}x = -\rho_* \int_\Omega (\mathbf{v}\otimes\mathbf{v}) : \nabla\boldsymbol{\phi}\,\mathrm{d}x + \rho_* \int_{\Gamma_{\mathrm{out}}} (\mathbf{v}\cdot\boldsymbol{\phi})\,(\mathbf{v}\cdot\mathbf{n})\,\mathrm{d}S, \tag{2.20}$$

for $\boldsymbol{\phi}\in\tilde{\mathbf{V}}$. We want to estimate

$$\begin{aligned}\|\partial_t \mathbf{v}\|_{L^{\frac{4}{3}}\left(0,T;(\tilde{\mathbf{V}})^\star\right)} &= \|\partial_t \mathbf{v}\|_{\left[L^4\left(0,T;\tilde{\mathbf{V}}\right)\right]^\star}\\ &:= \sup_{\|\boldsymbol{\varphi}\|_{L^4(0,T;\tilde{\mathbf{V}})}=1} \int_0^T \left\langle \frac{\partial \mathbf{v}}{\partial t}, \boldsymbol{\varphi}\right\rangle \mathrm{d}t.\end{aligned}$$

Substituting for the weak formulation (1.13) and using notation (2.20) for the convective term, we get

$$\begin{aligned}&\|\partial_t \mathbf{v}\|_{L^{\frac{4}{3}}\left(0,T;(\tilde{\mathbf{V}})^\star\right)} = \sup_{\|\boldsymbol{\varphi}\|_{L^4(0,T;\tilde{\mathbf{V}})}=1} \int_0^T \left\langle \frac{\partial \mathbf{v}}{\partial t}, \boldsymbol{\varphi}\right\rangle \mathrm{d}t\\
&= \sup_{\|\boldsymbol{\varphi}\|_{L^4(0,T;\tilde{\mathbf{V}})}=1} \frac{1}{\rho_*}\Bigg[\rho_* \int_0^T\int_\Omega (\mathbf{v}\otimes\mathbf{v}) : \nabla\boldsymbol{\varphi}\,\mathrm{d}x\,\mathrm{d}t - \rho_* \int_0^T\int_{\Gamma_{\mathrm{out}}} (\mathbf{v}\cdot\boldsymbol{\varphi})\,(\mathbf{v}\cdot\mathbf{n})\,\mathrm{d}S\,\mathrm{d}t\\
&- 2\mu_* \int_0^T\int_\Omega \mathbb{D}(\mathbf{v})\cdot\mathbb{D}(\boldsymbol{\varphi})\,\mathrm{d}x\,\mathrm{d}t - \frac{\theta}{\gamma_*(1-\theta)} \int_0^T\int_{\Gamma_{\mathrm{wall}}} \mathbf{v}_\tau\cdot\boldsymbol{\varphi}_\tau\,\mathrm{d}S\,\mathrm{d}t\\
&- P(t)\int_0^T\int_{\Gamma_{\mathrm{out}}} \boldsymbol{\varphi}\cdot\mathbf{n}\,\mathrm{d}S\,\mathrm{d}t + \rho_* \int_0^T\int_{\Gamma_{\mathrm{out}}} \frac{1}{2}(\mathbf{v}\cdot\mathbf{n})_-\mathbf{v}\cdot\boldsymbol{\varphi}\,\mathrm{d}S\,\mathrm{d}t\Bigg].\end{aligned}$$

This can be by Hölder inequality estimated as follows

$$\begin{aligned}&\|\partial_t \mathbf{v}\|_{\left[L^4\left(0,T;\tilde{\mathbf{V}}\right)\right]^\star} \le \sup_{\|\boldsymbol{\varphi}\|_{L^4(0,T;\tilde{\mathbf{V}})}=1} \frac{1}{\rho_*}\Bigg[\rho_* \int_0^T\int_\Omega |\mathbf{v}|^2|\nabla\boldsymbol{\varphi}|\,\mathrm{d}x\,\mathrm{d}t\\
&+ \rho_*\frac{3}{2}\int_0^T\int_{\Gamma_{\mathrm{out}}} |\mathbf{v}|^2|\boldsymbol{\varphi}|\,\mathrm{d}S\,\mathrm{d}t + 2\mu_*\|\mathbb{D}(\mathbf{v})\|_{L^2(0,T;\mathbf{L}^2(\Omega))}\|\mathbb{D}(\boldsymbol{\varphi})\|_{L^2(0,T;\mathbf{L}^2(\Omega))}\\
&+ \frac{\theta}{\gamma_*(1-\theta)}\|\mathbf{v}_\tau\|_{L^2(0,T;\mathbf{L}^2(\Gamma_{\mathrm{out}}))}\|\boldsymbol{\varphi}\|_{L^2(0,T;\mathbf{L}^2(\Gamma_{\mathrm{out}}))} + |P(t)|\|\boldsymbol{\varphi}\|_{L^1(0,T;L^1(\Omega))}\Bigg].\end{aligned} \tag{2.21}$$

Now let us focus on the first two terms on right hand side of the inequality, which are most problematic.

Estimation of $\int_0^T\int_\Omega |\mathbf{v}|^2|\nabla\boldsymbol{\varphi}|\,\mathrm{d}x\,\mathrm{d}t$. By Hölder inequality in space for $p=2$, $p'=2$ and then Hölder inequality in time for $p=\frac{q}{2}$, $p'=\frac{q}{q-2}$, we get

$$\int_0^T\int_\Omega |\mathbf{v}|^2|\nabla\boldsymbol{\varphi}|\,\mathrm{d}x\,\mathrm{d}t \le \int_0^T \|\mathbf{v}\|_4^2\|\nabla\boldsymbol{\varphi}\|_2\,\mathrm{d}t \le \left(\int_0^T \|\mathbf{v}\|_4^q\,\mathrm{d}t\right)^{\frac{2}{q}}\left(\int_0^T \|\nabla\boldsymbol{\varphi}\|_2^{\frac{q}{q-2}}\,\mathrm{d}t\right)^{\frac{q-2}{q}}.$$

Due to (2.11) for $s_2 = 4$, use $s_1 = q = \frac{8}{3}$, leading to

$$\begin{aligned}\int_0^T \int_\Omega |\mathbf{v}|^2 |\nabla \boldsymbol{\varphi}| \,\mathrm{d}x \,\mathrm{d}t &\leq \|\mathbf{v}\|^2_{L^{\frac{8}{3}}(0,T;\mathbf{L}^4(\Omega))} \|\nabla \boldsymbol{\varphi}\|_{L^4(0,T;\mathbf{L}^2(\Omega))} \\ &\leq \|\mathbf{v}\|^2_{L^{\frac{8}{3}}(0,T;\mathbf{L}^4(\Omega))} \|\boldsymbol{\varphi}\|_{L^4\left(0,T;\tilde{\mathbf{V}}\right)}.\end{aligned} \tag{2.22}$$

Estimation of $\int_0^T \int_{\Gamma_{\text{out}}} |\mathbf{v}|^2 |\boldsymbol{\varphi}| \,\mathrm{d}S \,\mathrm{d}t$. Using Hölder inequality for $p = \frac{4}{3}$, $p' = 4$ leads to

$$\begin{aligned}\int_0^T \int_{\Gamma_{\text{out}}} |\mathbf{v}|^2 |\boldsymbol{\varphi}| \,\mathrm{d}S \,\mathrm{d}t &\leq \|\mathbf{v}\|^2_{L^{\frac{8}{3}}\left(0,T;\mathbf{L}^{\frac{8}{3}}(\Gamma_{\text{out}})\right)} \|\boldsymbol{\varphi}\|_{L^4(0,T;L^4(\Gamma_{\text{out}}))} \\ &\leq \|\mathbf{v}\|^2_{L^{\frac{8}{3}}\left(0,T;\mathbf{L}^{\frac{8}{3}}(\Gamma_{\text{out}})\right)} \|\boldsymbol{\varphi}\|_{L^4\left(0,T;\tilde{\mathbf{V}}\right)}.\end{aligned} \tag{2.23}$$

The second inequality is possible due to (2.16) for $s = 4$ together with (2.13).
All together, (2.21) with results (2.22) and (2.23) (estimation of the other terms are trivial with help of the Sobolev embeddings, trace theorem and Korn inequality) reads

$$\begin{aligned}\|\partial_t \mathbf{v}\|_{\left[L^4\left(0,T;\tilde{\mathbf{V}}\right)\right]^\star} \leq \sup_{\|\boldsymbol{\varphi}\|_{L^4(0,T;\tilde{\mathbf{V}})}=1} \frac{1}{\rho_*} \|\boldsymbol{\varphi}\|_{L^4\left(0,T;\tilde{\mathbf{V}}\right)} \cdot \Bigg[& \rho_* \|\mathbf{v}\|^2_{L^{\frac{8}{3}}(0,T;\mathbf{L}^4(\Omega))} \\ & + \rho_* \frac{3}{2} \|\mathbf{v}\|^2_{L^{\frac{8}{3}}\left(0,T;\mathbf{L}^{\frac{8}{3}}(\Gamma_{\text{out}})\right)} + 2\mu_* \|\mathbb{D}(\mathbf{v})\|_{L^2(0,T;\mathbf{L}^2(\Omega))} \\ & + \frac{\theta}{\gamma_*(1-\theta)} \|\mathbf{v}_\tau\|_{L^2(0,T;\mathbf{L}^2(\Gamma_{\text{wall}}))} + |P(t)| \Bigg].\end{aligned}$$

Terms in bracket are finite due to (2.11), (2.15), (2.9) and (2.4). □

2.2 Existence of the weak solution

Proof of the existence follows by standard procedure. First, we define the approximate solution using the Galerkin method. Then, we show the existence of this approximate solution, establish uniform estimates, and obtain the existence of a weak solution by taking the limit in the weak formulation of the approximate solution. Additionally, we show the energy inequality and verify that the initial condition is satisfied. In [31] the proof of the existence of weak solution following this procedure is provided in detail, however only for the evolutionary Navier-Stokes equations with purely homogeneous boundary conditions on $\partial\Omega$. We will partially follow this reference, as many of the manipulations are similar or even coincides.

2.2.1 Galerkin aprroximation

Let us have the problem

$$\begin{aligned} -\operatorname{div}\mathbb{T} = -\mu_*\Delta\mathbf{w} + \nabla p &= \tilde{\lambda}\mathbf{w} && \text{in } \Omega \\ \operatorname{div}\mathbf{w} &= 0 && \text{in } \Omega \\ \mathbf{w} &= 0 && \text{on } \Gamma_{\text{in}} \\ \mathbf{w}\cdot\mathbf{n} &= 0 && \text{on } \Gamma_{\text{wall}} \\ (\mathbb{T}\mathbf{n})_\tau &= 0 && \text{on } \Gamma_{\text{wall}} \\ \mathbb{T}\mathbf{n} &= 0 && \text{on } \Gamma_{\text{out}}, \end{aligned}$$

where $\mathbb{T}$ is define as (1.3). Thus we want to find eigenvalues $\lambda \in \mathbb{R}$, s.t. $\lambda = \frac{\tilde{\lambda}}{\mu_*}$, and corresponding eigenfunctions $\mathbf{w} \in \tilde{\mathbf{V}}$, definition of $\tilde{\mathbf{V}}$ in (1.11), such that they satisfy the spectral problem

$$((\mathbf{w}, \boldsymbol{\varphi})) = \lambda(\mathbf{w}, \boldsymbol{\varphi}) \quad \forall\, \boldsymbol{\varphi} \in \tilde{\mathbf{V}}, \tag{2.24}$$

where $((\mathbf{w}, \boldsymbol{\varphi})) := (\nabla\,\mathbf{w}, \nabla\,\boldsymbol{\varphi}) = \int_\Omega \nabla\,\mathbf{w} : \nabla\,\boldsymbol{\varphi}\,\mathrm{d}x$. In a similar manner as in [27] we get the existence of eigenvalues $\{\lambda_i\}_{i=1}^\infty$ and corresponding eigenfunctions $\{\mathbf{w}_i\}_{i=1}^\infty$, satisfying (2.24). It holds that $(\mathbf{w}_i, \mathbf{w}_j) = \delta_{ij}$, $\left(\left(\frac{\mathbf{w}_i}{\sqrt{\lambda_i}}, \frac{\mathbf{w}_j}{\sqrt{\lambda_j}}\right)\right) = \delta_{ij}$ and $\{\mathbf{w}_i\}_{i=1}^\infty$ form basis in $\tilde{\mathbf{V}}$. Moreover there exist $P^n : \tilde{\mathbf{V}} \to H^N := \operatorname{span}\{\mathbf{w}_1, .., \mathbf{w}_N\}$, defined as

$$P^n\boldsymbol{\varphi} := \sum_{i=1}^n \left(\int_\Omega \boldsymbol{\varphi}\mathbf{w}_i\,\mathrm{d}x\right)\mathbf{w}_i, \tag{2.25}$$

for $\boldsymbol{\varphi} \in \tilde{\mathbf{V}}$, satisfying

$$\|P^n\boldsymbol{\varphi}\|_{L^2} \le \|\boldsymbol{\varphi}\|_{L^2}, \tag{2.26}$$

$$\|P^n\boldsymbol{\varphi}\|_{\tilde{\mathbf{V}}} \le \|\boldsymbol{\varphi}\|_{\tilde{\mathbf{V}}}. \tag{2.27}$$

We define the n-th Galerkin approximation of $\mathbf{v}^n$ as

$$\mathbf{v}^n(t,x) = \sum_{i=1}^n a_i^n(t)\mathbf{w}_i(x) + \mathbf{v}_{\text{in}}^*(t,x) \tag{2.28}$$

with

$$\mathbf{v}^n(0,x) = \sum_{i=1}^n a_i^n(0)\mathbf{w}_i(x) + \mathbf{v}_{\text{in}}^*(0,x) = \sum_{i=1}^n \left(\int_\Omega \mathbf{v}_0\mathbf{w}_i\,\mathrm{d}x\right)\mathbf{w}_i(x) + \mathbf{v}_{\text{in}}^*(0,x) \tag{2.29}$$

satisfying

$$\begin{aligned} &\rho_*\int_\Omega \frac{\partial\mathbf{v}^n}{\partial t}\mathbf{w}_j\,\mathrm{d}x + \rho_*\int_\Omega (\nabla\mathbf{v}^n)\mathbf{v}^n\cdot\mathbf{w}_j\,\mathrm{d}x + 2\mu_*\int_\Omega \mathbb{D}(\mathbf{v}^n) : \mathbb{D}(\mathbf{w}_j)\,\mathrm{d}x \\ &+ \frac{\theta}{\gamma_*(1-\theta)}\int_{\Gamma_{\text{wall}}} (\mathbf{v}^n)_\tau\cdot(\mathbf{w}_j)_\tau\,\mathrm{d}S = -P(t)\int_{\Gamma_{\text{out}}} \mathbf{w}_j\cdot\mathbf{n}\,\mathrm{d}S \\ &+ \frac{\rho_*}{2}\int_{\Gamma_{\text{out}}} (\mathbf{v}^n\cdot\mathbf{n})_-\mathbf{v}^n\cdot\mathbf{w}_j\,\mathrm{d}S \\ &\forall\, \mathrm{j} \in 1, .., n \text{ and a.a. } t \in (0,T). \end{aligned} \tag{2.30}$$

Here we can represent the duality by integral $\left(\left\langle \frac{\partial \mathbf{v}^n}{\partial t}, \mathbf{w}_j \right\rangle = \int_\Omega \frac{\partial \mathbf{v}^n}{\partial t} \mathbf{w}_j \,\mathrm{d}x\right)$ since $\mathbf{v}^n - \mathbf{v}^*_{\mathrm{in}}$ is a linear combination of functions from $\tilde{\mathbf{V}}$. By standard procedure, we substitute (2.28) to (2.30) and use the orthonormality of the basis in $\mathbf{L}^2(\Omega)$) and orthogonality in $\tilde{\mathbf{V}}$ to get the system of ordinary differential equations for unknowns $\mathbf{a}^n = (a_1^n, .., a_n^n)$ of type

$$\frac{\partial \mathbf{a}^n}{\partial t} = f(\mathbf{a}^n) \tag{2.31}$$

$$\mathbf{a}^n(0) = \left(\int_\Omega \mathbf{v}_0 \mathbf{w}_1 \,\mathrm{d}x, .., \int_\Omega \mathbf{v}_0 \mathbf{w}_n \,\mathrm{d}x\right). \tag{2.32}$$

Since $f(\mathbf{a}^n)$ is continuous, Carathéodory theory can be used and we get the local existence of $\mathbf{a}^n \in AC\,[0, T^*)$ solving the system for $\forall n \in \mathbb{N}$ and a.a. $t \in (0, T^*)$. Due to the following uniform estimates we will see that $T^* = T$, hence we get the global existence.

2.2.2 Uniform estimates

Uniform estimates for $\mathbf{v}^n - \mathbf{v}^*_{\mathrm{in}}$.

We multiply (2.30) by $a_j^n(t)$ and do the sum $\sum_{j=1}^n$ (it can be seen as testing by function $\mathbf{v}^n - \mathbf{v}^*_{\mathrm{in}}$). The procedure is then the same as in a priori estimates and we again refer to [9] (treatment of the most problematic convective term is for clarity explained in footnote in section 2.1). Eventually we get the energy equality for the Galerkin approximation as

$$\begin{aligned}
&\frac{\rho_*}{2}\|(\mathbf{v}^n - \mathbf{v}^*_{\mathrm{in}})(t,\cdot)\|^2_{L^2(\Omega)} + 2\mu_* \int_0^t \|\mathbb{D}(\mathbf{v}^n - \mathbf{v}^*_{\mathrm{in}})\|^2_{L^2(\Omega)} \,\mathrm{d}s \\
&+ \frac{\theta}{\gamma_*(1-\theta)} \int_0^t \int_{\Gamma_{\mathrm{wall}}} |\mathbf{v}^n_\tau|^2 \,\mathrm{d}S \,\mathrm{d}s + \int_0^t \int_{\Gamma_{\mathrm{out}}} \rho_* \frac{|\mathbf{v}^n|^2}{2} (\mathbf{v}^n \cdot \mathbf{n})_+ \,\mathrm{d}S \,\mathrm{d}s \\
&= \frac{\rho_*}{2}\|(\mathbf{v}^n - \mathbf{v}^*_{\mathrm{in}})(0,\cdot)\|^2_{L^2(\Omega)} + \frac{\theta}{\gamma_*(1-\theta)} \int_0^t \int_{\Gamma_{\mathrm{wall}}} \mathbf{v}^n_\tau \cdot (\mathbf{v}^*_{\mathrm{in}})_\tau \,\mathrm{d}S \,\mathrm{d}s \\
&- \int_0^t \int_\Omega \rho_* (\mathbf{v}^n - \mathbf{v}^*_{\mathrm{in}}) \otimes (\mathbf{v}^n - \mathbf{v}^*_{\mathrm{in}}) : \nabla \mathbf{v}^*_{\mathrm{in}} \,\mathrm{d}x \,\mathrm{d}s \\
&+ \int_0^t \int_\Omega \rho_* (\mathbf{v}^*_{\mathrm{in}} \otimes \mathbf{v}^*_{\mathrm{in}}) : \mathbb{D}(\mathbf{v}^n - \mathbf{v}^*_{\mathrm{in}}) \,\mathrm{d}x \,\mathrm{d}s - \int_0^t \int_\Omega \rho_* \frac{\partial \mathbf{v}^*_{\mathrm{in}}}{\partial t} \cdot (\mathbf{v}^n - \mathbf{v}^*_{\mathrm{in}}) \,\mathrm{d}x \,\mathrm{d}s \\
&- P(t) \int_0^t \int_{\Gamma_{\mathrm{in}}} \mathbf{v}^n \cdot \mathbf{n} \,\mathrm{d}S \,\mathrm{d}s - 2\mu_* \int_0^t \int_\Omega \mathbb{D}(\mathbf{v}^*_{\mathrm{in}}) : \mathbb{D}(\mathbf{v}^n - \mathbf{v}^*_{\mathrm{in}}) \,\mathrm{d}x. \,\mathrm{d}s
\end{aligned} \tag{2.33}$$

By standard procedure, using Cauchy-Schwartz, Young, Hölder inequalities and Gronwall lemma we get (also provided n [9])

$$\begin{aligned}
&\rho_* \sup_{t\in[0,T]} \|(\mathbf{v}^n - \mathbf{v}^*_{\mathrm{in}})(t,\cdot)\|_2^2 + \mu_* \int_0^T \|\mathbb{D}(\mathbf{v}^n - \mathbf{v}^*_{\mathrm{in}})\|_2^2 \,\mathrm{d}t \\
&+ \frac{\theta}{\gamma_*(1-\theta)} \int_0^T \int_{\Gamma_{\mathrm{wall}}} |\mathbf{v}^n_\tau|^2 \,\mathrm{d}S \,\mathrm{d}t + \int_0^T \int_{\Gamma_{\mathrm{out}}} \rho_* |\mathbf{v}^n|^2 (\mathbf{v}^n \cdot \mathbf{n})_+ \,\mathrm{d}S \,\mathrm{d}t \\
&\leq C\left(T, \|\mathbf{v}^n_0 - \mathbf{v}^*_{\mathrm{in}}(0,\cdot)\|_2^2, \tilde{C}(\mathbf{v}^*_{\mathrm{in}})\right) < \infty.
\end{aligned} \tag{2.34}$$

Boundedness of the first term gives

$$\sup_{t\in[0,T]} |\mathbf{a}^n(t)|^2 \leq C,$$

implying the global existence of $\mathbf{a}^n(t)$, hence also $\mathbf{v}^n$ on $(0,T)$. From (2.1) we can also get the n-independent estimates for sequence $\mathbf{v}^n$ (by triangle inequality from $\mathbf{v}^n = \mathbf{v}^n - \mathbf{v}^*_{\text{in}} + \mathbf{v}^*_{\text{in}}$) as

$$\|\mathbf{v}^n\|_{L^\infty(0,T;\mathbf{L}^2(\Omega))} \leq \|\mathbf{v}^n - \mathbf{v}^*_{\text{in}}\|_{L^\infty(0,T;\mathbf{L}^2(\Omega))} + \|\mathbf{v}^*_{\text{in}}\|_{L^\infty(0,T;\mathbf{L}^2(\Omega))} \leq C(T, \mathbf{v}^*_{\text{in}}, \mathbf{v}_0) \quad (2.35)$$

$$\|\mathbf{v}^n\|_{L^2(0,T;\tilde{\mathbf{V}}_\mathbf{n})} \leq \|\mathbf{v}^n - \mathbf{v}^*_{\text{in}}\|_{L^2(0,T;\tilde{\mathbf{V}})} + \|\mathbf{v}^*_{\text{in}}\|_{L^2(0,T;\tilde{\mathbf{V}}_\mathbf{n})} \leq C(T, \mathbf{v}^*_{\text{in}}, \mathbf{v}_0) \quad (2.36)$$

and

$$\|\mathbf{v}^n_\tau\|_{L^2(0,T;\mathbf{L}^2(\Gamma_{\text{wall}}))} \leq C(T, \mathbf{v}^*_{\text{in}}, \mathbf{v}_0). \quad (2.37)$$

In same way as in a priori estimates (2.11), (2.15), it can be also shown that

$$\|\mathbf{v}^n\|_{L^{s_1}(0,T;\mathbf{L}^{s_2}(\Omega)} \leq C \quad \text{for } s_2 = \frac{6s_1}{3s_1 - 4},\ s_2 \in [2,6], \quad (2.38)$$

$$\|\mathbf{v}^n\|_{L^{\frac{8}{3}}(0,T;\mathbf{L}^{\frac{8}{3}}(\Gamma_{\text{out}}))} \leq C, \quad (2.39)$$

for constant C independent of n.

Uniform estimate for $\frac{\partial \mathbf{v}^n}{\partial t}$.

We want to estimate

$$\|\partial_t \mathbf{v}^n\|_{L^{\frac{4}{3}}\left(0,T;(\tilde{\mathbf{V}})^\star\right)} := \sup_{\|\boldsymbol{\varphi}\|_{L^4(0,T;\tilde{\mathbf{V}})}=1} \int_0^T \int_\Omega \frac{\partial \mathbf{v}^n}{\partial t} \boldsymbol{\varphi} \,\mathrm{d}x \,\mathrm{d}t.$$

We separate the test function $\boldsymbol{\varphi}$ as $\boldsymbol{\varphi} = P^n\boldsymbol{\varphi} + \tilde{\boldsymbol{\varphi}}$. Here $P^n\boldsymbol{\varphi}$, defined in (2.25), is the orthogonal projection onto $\{\mathbf{w}_i\}_{i=1}^n$. Term $\tilde{\boldsymbol{\varphi}}$ denotes the rest, orthogonal to $\{\mathbf{w}_i\}_{i=1}^n$. Therefore

$$\|\partial_t \mathbf{v}^n\|_{L^{\frac{4}{3}}\left(0,T;(\tilde{\mathbf{V}})^\star\right)} = \sup_{\|\boldsymbol{\varphi}\|_{L^4(0,T;\tilde{\mathbf{V}})}=1} \int_0^T \int_\Omega \frac{\partial \mathbf{v}^n}{\partial t} P^n\boldsymbol{\varphi} \,\mathrm{d}x \,\mathrm{d}t$$

and we can substitute the weak formulation (2.30) and proceed as in a priori estimates in section 2.1.2, using the property (2.27). Finally we get the n-independent estimates for sequence $\partial_t \mathbf{v}^n$ as

$$\|\partial_t \mathbf{v}^n\|_{L^{\frac{4}{3}}\left(0,T;(\tilde{\mathbf{V}})^\star\right)} \leq C(T, \mathbf{v}^*_{\text{in}}, \mathbf{v}_0). \quad (2.40)$$

Limit passage

Consequently from the uniform estimates (2.36), (2.35), (2.37), (2.40), there exist a weakly converging subsequences (for simplicity of notation not relabelled), such that

$$\mathbf{v}^n \rightharpoonup \mathbf{v} \quad \text{in} \quad L^2(0,T;\tilde{\mathbf{V}}_\mathbf{n}), \quad (2.41)$$

$$\mathbf{v}^n \rightharpoonup^* \mathbf{v} \quad \text{in} \quad L^\infty(0,T;\mathbf{L}^2_{0,\text{div}}(\Omega)), \quad (2.42)$$

$$\mathbf{v}^n_\tau \rightharpoonup \mathbf{v}_\tau \quad \text{in} \quad L^2(0,T;\mathbf{L}^2(\Gamma_{\text{wall}})), \quad (2.43)$$

$$\partial_t \mathbf{v}^n \rightharpoonup \partial_t \mathbf{v} \quad \text{in} \quad L^{\frac{4}{3}}\left(0,T;(\tilde{\mathbf{V}})^\star\right). \quad (2.44)$$

To pass to the limit, we multiply the weak formulation for $\mathbf{v}^n$ (2.30) by $\psi \in \mathbf{C}^\infty(0,T)$ and integrate over the time interval $(0,T)$ and get

$$\begin{aligned}
&\rho_* \int_0^T \int_\Omega \frac{\partial \mathbf{v}^n}{\partial t} \cdot \psi \mathbf{w}_j \,\mathrm{d}x\,\mathrm{d}t - \rho_* \int_0^T \int_\Omega (\mathbf{v}^n \otimes \mathbf{v}^n) : \nabla \mathbf{w}_j \psi \,\mathrm{d}x\,\mathrm{d}t \\
&+ \int_0^T \int_{\Gamma_{\text{out}}} (\mathbf{v}^n \cdot \mathbf{n})\,(\mathbf{v}^n \cdot \mathbf{w}_j)\psi \,\mathrm{d}S\,\mathrm{d}t + 2\mu_* \int_0^T \int_\Omega \mathbb{D}(\mathbf{v}^n) : \mathbb{D}(\mathbf{w}_j)\psi \,\mathrm{d}x\,\mathrm{d}t \\
&+ \frac{\theta}{\gamma_*(1-\theta)} \int_0^T \int_{\Gamma_{\text{wall}}} (\mathbf{v}^n)_\tau \cdot (\mathbf{w}_j)_\tau \psi \,\mathrm{d}S\,\mathrm{d}t = -P(t) \int_0^T \int_{\Gamma_{\text{out}}} \psi \mathbf{w}_j \cdot \mathbf{n} \,\mathrm{d}S\,\mathrm{d}t \\
&+ \frac{\rho_*}{2} \int_0^T \int_{\Gamma_{\text{out}}} (\mathbf{v}^n \cdot \mathbf{n})_- (\mathbf{v}^n \cdot \mathbf{w}_j)\psi \,\mathrm{d}S\,\mathrm{d}t \\
&\forall\, \mathrm{j} \in 1, .., n,
\end{aligned} \tag{2.45}$$

where we additionally used formula (2.20). For all the linear terms in (2.45) is enough to use definition of weak convergence from obtained results (2.41), (2.43), (2.44) and pass the limit $n \to \infty$. However the non-linear convective term and non-linear term on Γ_{out} must be treated applying Aubin-Lions lemma, stated for example in [35].

Convective term on Ω. If holds (2.36), (2.40) and $\tilde{\mathbf{V}}_{\mathbf{n}} \hookrightarrow\hookrightarrow \mathbf{L}^2_{0,\text{div}}(\Omega) \hookrightarrow (\tilde{\mathbf{V}})^\star$ are Banach and reflexive spaces, then from Aubin-Lions lemma yields

$$\mathbf{v}^n \to \mathbf{v} \qquad \text{in} \quad L^2(0,T;\mathbf{L}^2(\Omega)). \tag{2.46}$$

Having (2.38) for $s_1 = s_2 = \frac{10}{3}$ and (2.46), the interpolation inequality for $r \in \left(2, \frac{10}{3}\right)$ gives

$$||\mathbf{v}^n - \mathbf{v}||_{L^r(Q)} \le ||\mathbf{v}^n - \mathbf{v}||^{\lambda}_{L^2(Q)} ||\mathbf{v}^n - \mathbf{v}||^{1-\lambda}_{L^{\frac{10}{3}}(Q)} \le C||\mathbf{v}^n - \mathbf{v}||^{\lambda}_{L^2(Q)} \xrightarrow{n\to\infty} 0,$$

where we use notation $Q = (0,T) \times \Omega^3$. Hence for $\lambda \in (0,1)$ we eventually obtain

$$\mathbf{v}^n \to \mathbf{v} \qquad \text{in} \quad L^r(0,T;\mathbf{L}^r(\Omega)), \quad r \in \left[1, \frac{10}{3}\right), \tag{2.47}$$

where the relation for $r \in [1,2]$ it is trivial due to (2.46). Now let us focus on the part of the convective term on Ω in (2.45). We have

$$\begin{aligned}
&\left| \int_0^T \int_\Omega [(\mathbf{v}^n \otimes \mathbf{v}^n) : \nabla \mathbf{w}_j \psi - (\mathbf{v} \otimes \mathbf{v}) : \nabla \mathbf{w}_j \psi] \,\mathrm{d}x\,\mathrm{d}t \right| \\
&\le \int_0^T \int_\Omega \left| \frac{\partial (w_j)_i}{\partial x_k} \right| |\psi| \,|(v_i^n - v_i)v_k^n - (v_k - v_k^n)v_i| \,\mathrm{d}x\,\mathrm{d}t \\
&\le \sup_{t\in[0,T]} |\psi| \Big(\int_0^T \int_\Omega \left| \frac{\partial (w_j)_i}{\partial x_k} \right| |(v_i^n - v_i)| \,|v_k^n| \,\mathrm{d}x\,\mathrm{d}t \\
&+ \int_0^T \int_\Omega \left| \frac{\partial (w_j)_i}{\partial x_k} \right| |(v_k - v_k^n)| \,|v_i| \,\mathrm{d}x\,\mathrm{d}t \Big) \\
&\le \sup_{t\in[0,T]} |\psi| \Big(\int_0^T ||\nabla \mathbf{w}_j||_{\mathbf{L}^2(\Omega)} ||\mathbf{v}^n - \mathbf{v}||_{\mathbf{L}^3(\Omega)} ||\mathbf{v}^n||_{\mathbf{L}^6(\Omega)} \,\mathrm{d}t \\
&+ \int_0^T ||\nabla \mathbf{w}_j||_{\mathbf{L}^2(\Omega)} ||\mathbf{v}^n - \mathbf{v}||_{\mathbf{L}^3(\Omega)} ||\mathbf{v}||_{\mathbf{L}^6(\Omega)} \,\mathrm{d}t \Big) \\
&\le \sup_{t\in[0,T]} |\psi| ||\nabla \mathbf{w}_j||_{\mathbf{L}^2(\Omega)} ||\mathbf{v}^n - \mathbf{v}||_{L^2(0,T;\mathbf{L}^3(\Omega))} \left(||\mathbf{v}^n||_{L^2(0,T;\mathbf{L}^6(\Omega))} + ||\mathbf{v}||_{L^2(0,T;\mathbf{L}^6(\Omega))} \right),
\end{aligned}$$

the Hölder inequality for exponents $p = 2$, $q = 3$ and $r = 6$ is used. Due to the strong convergence of $\mathbf{v}^n$ in $L^2(0,T;\mathbf{L}^3(\Omega))$ from (2.47) and boundedness of $\mathbf{v}$ and $\mathbf{v}^n$ in $L^2(0,T;\mathbf{L}^6(\Omega))$ coming from (2.9) and (2.36), the right hand side goes to zero as $n \to \infty$.

Non-linear terms on Γ_{out}. Now it remains the treat the non-linear terms on Γ_{out} in (2.45). We investigate the convergence of

$$\int_0^T \int_{\Gamma_{\text{out}}} (\mathbf{v}^n \cdot \mathbf{n})(\mathbf{v}^n \cdot \mathbf{w}_j)\psi \,\mathrm{d}S \,\mathrm{d}t,$$

as it is stronger requirement than with the negative part. Hence

$$\begin{aligned}
&\left| \int_0^T \int_{\Gamma_{\text{out}}} [(\mathbf{v}^n \cdot \mathbf{n})(\mathbf{v}^n \cdot \mathbf{w}_j)\psi - (\mathbf{v} \cdot \mathbf{n})(\mathbf{v} \cdot \mathbf{w}_j)\psi] \,\mathrm{d}S \,\mathrm{d}t \right| \\
&\leq \int_0^T \int_{\Gamma_{\text{out}}} |v_i^n n_i \, v_k^n (w_j)_k \psi - v_i n_i \, v_k (w_j)_k \psi| \,\mathrm{d}S \,\mathrm{d}t \\
&\leq \sup_{t\in[0,T]} |\psi| \int_0^T \int_{\Gamma_{\text{out}}} |(w_j)_k||(v_i^n - v_i)v_k^n - (v_k - v_k^n)v_i| \,\mathrm{d}S \,\mathrm{d}t \\
&\leq \sup_{t\in[0,T]} |\psi| \Big(\int_0^T \int_{\Gamma_{\text{out}}} |(w_j)_k||(v_i^n - v_i)||v_k^n| \,\mathrm{d}S \,\mathrm{d}t \\
&+ \int_0^T \int_{\Gamma_{\text{out}}} |(w_j)_k||(v_k - v_k^n)||v_i| \,\mathrm{d}S \,\mathrm{d}t \Big) \\
&\leq \sup_{t\in[0,T]} |\psi| \left(\int_0^T ||\mathbf{w}_j||_{\mathbf{L}^4(\Gamma_{\text{out}})} ||\mathbf{v}^n - \mathbf{v}||_{\mathbf{L}^2(\Gamma_{\text{out}})} ||\mathbf{v}^n||_{\mathbf{L}^4(\Gamma_{\text{out}})} \,\mathrm{d}t \right) \\
&+ \sup_{t\in[0,T]} |\psi| \left(\int_0^T ||\mathbf{w}_j||_{\mathbf{L}^4(\Gamma_{\text{out}})} ||\mathbf{v}^n - \mathbf{v}||_{\mathbf{L}^2(\Gamma_{\text{out}})} ||\mathbf{v}||_{\mathbf{L}^4(\Gamma_{\text{out}})} \,\mathrm{d}t \right) \\
&\leq \sup_{t\in[0,T]} |\psi| ||\mathbf{w}_j||_{\mathbf{L}^4(\Gamma_{\text{out}})} ||\mathbf{v}^n - \mathbf{v}||_{L^2(0,T,\mathbf{L}^2(\Gamma_{\text{out}}))} \\
&\cdot \left(||\mathbf{v}^n||_{L^2(0,T,\mathbf{L}^4(\Gamma_{\text{out}}))} + ||\mathbf{v}||_{L^2(0,T,\mathbf{L}^4(\Gamma_{\text{out}}))} \right) \\
&\leq C||\mathbf{v}^n - \mathbf{v}||_{L^2(0,T,\mathbf{L}^2(\Gamma_{\text{out}}))} \leq C||\mathbf{v}^n - \mathbf{v}||_{L^2(0,T,\mathbf{L}^{2+\epsilon}(\Gamma_{\text{out}}))},
\end{aligned}$$

for some small positive ϵ. In derivation we used Hölder inequality for $p = 2$, $q = 4$, $r = 4$ in the fourth inequality and (2.13), (2.16), setting $s = 4$ to get $\|\mathbf{v}\|_{L^2(0,T;\mathbf{L}^4(\Gamma_{\text{out}}))} \leq C\|\mathbf{v}\|_{L^2(0,T;\mathbf{W}^{\frac{1}{2},2}(\Gamma_{\text{out}}))} \leq C\|\mathbf{v}\|_{L^2\left(0,T;\mathbf{W}^{1,2}_{\text{div},\,\mathbf{n}}(\Omega)\right)} \leq C$ and the same for $\mathbf{v}^n$ with C independent of n.
Now by the embedding (2.16), we get

$$W^{\frac{s-2}{s},2}(\partial\Omega) \hookrightarrow L^s(\partial\Omega)$$

for $s = 2 + \epsilon$, hence $\frac{s-2}{s} = \tilde{\epsilon}$ also small positive. By the continuous trace operator (2.13) defined for $r \in \left(\frac{1}{2}, 1\right]$

$$\mathrm{tr} : W^{r,2}(\Omega) \to W^{r-\frac{1}{2},2}(\partial\Omega),$$

we set $r - \frac{1}{2} = \tilde{\epsilon}$, hence $r = \frac{1}{2} + \tilde{\epsilon}$. Therefore

$$\begin{aligned}
&||\mathbf{v}^n - \mathbf{v}||_{L^2(0,T,\mathbf{L}^2(\Gamma_{\text{out}}))} \leq C||\mathbf{v}^n - \mathbf{v}||_{L^2(0,T,\mathbf{L}^{2+\epsilon}(\Gamma_{\text{out}}))} \leq C||\mathbf{v}^n - \mathbf{v}||_{L^2(0,T,\mathbf{W}^{\tilde{\epsilon},2}(\Gamma_{\text{out}}))} \\
&C \leq ||\mathbf{v}^n - \mathbf{v}||_{L^2(0,T,\mathbf{W}^{\frac{1}{2}+\tilde{\epsilon},2}_{\text{div, bc}}(\Omega))} = C||(\mathbf{v}^n - \mathbf{v}^*_{\text{in}}) - (\mathbf{v} - \mathbf{v}^*_{\text{in}})||_{L^2(0,T,\mathbf{W}^{\frac{1}{2}+\tilde{\epsilon},2}_{\text{div, bc}}(\Omega))}. \quad (2.48)
\end{aligned}$$

The strong convergence of $\mathbf{v}^n - \mathbf{v}^*_{\text{in}}$ in space $L^2(0,T,\mathbf{W}^{\frac{1}{2}+\tilde{\epsilon},2}_{\text{div, bc}}(\Omega)^3)$ is provided by Aubin-Lions lemma. Let us have $\mathbf{W}^{1,2}_{\text{div, bc}}(\Omega)^3 \hookrightarrow\hookrightarrow \mathbf{W}^{1-\epsilon,2}_{\text{div, bc}}(\Omega)^3 \hookrightarrow (\mathbf{W}^{1,2}_{\text{div, bc}}(\Omega)^3)^\star$ Banach, reflexive spaces and results (2.36), (2.40). Then

$$\mathbf{v}^n - \mathbf{v}^*_{\text{in}} \to \mathbf{v} - \mathbf{v}^*_{\text{in}} \qquad \text{in} \quad L^2(0,T;\mathbf{W}^{1-\epsilon,2}_{\text{div, bc}}(\Omega)^3).$$

Therefore with continuous embedding $\mathbf{W}^{1-\epsilon,2}_{\text{div,bc}}(\Omega)^3 \hookrightarrow \mathbf{W}^{\frac{1}{2}+\tilde{\epsilon},2}_{\text{div,bc}}(\Omega)^3$ for small positive ϵ and $\tilde{\epsilon}$, s.t. $1-\epsilon > \tilde{\epsilon}$, we can also get

$$\mathbf{v}^n - \mathbf{v}^*_{\text{in}} \to \mathbf{v} - \mathbf{v}^*_{\text{in}} \qquad \text{in} \quad L^2(0,T;\mathbf{W}^{\frac{1}{2}+\tilde{\epsilon},2}_{\text{div,bc}}(\Omega)^3). \tag{2.49}$$

Hence from results (2.48) and (2.49) we can finally write

$$\mathbf{v}^n \to \mathbf{v} \qquad \text{in} \quad L^2(0,T;\mathbf{L}^2(\Gamma_{\text{out}})) \tag{2.50}$$

and

$$\left| \int_0^T \int_{\Gamma_{\text{out}}} [(\mathbf{v}^n \cdot \mathbf{n})(\mathbf{v}^n \cdot \mathbf{w}_j)\psi - (\mathbf{v} \cdot \mathbf{n})(\mathbf{v} \cdot \mathbf{w}_j)\psi] \,\mathrm{d}S \,\mathrm{d}t \right| \xrightarrow{n\to\infty} 0$$

and consequently

$$\begin{aligned}
&\rho_* \int_0^T \left\langle \frac{\partial \mathbf{v}}{\partial t}, \mathbf{w}_j \right\rangle \psi \,\mathrm{d}t + \rho_* \int_0^T \int_\Omega (\nabla \mathbf{v})\mathbf{v} \cdot \psi \mathbf{w}_j \,\mathrm{d}x \,\mathrm{d}t \\
&+ 2\mu_* \int_0^T \int_\Omega \mathbb{D}(\mathbf{v}) : \mathbb{D}(\mathbf{w}_j)\psi \,\mathrm{d}x \,\mathrm{d}t + \frac{\theta}{\gamma_*(1-\theta)} \int_0^T \int_{\Gamma_{\text{wall}}} (\mathbf{v})_\tau \cdot (\mathbf{w}_j)_\tau \psi \,\mathrm{d}S \,\mathrm{d}t \\
&= -P(t) \int_0^T \int_{\Gamma_{\text{out}}} \psi \mathbf{w}_j \cdot \mathbf{n} \,\mathrm{d}S \,\mathrm{d}t + \frac{\rho_*}{2} \int_0^T \int_{\Gamma_{\text{out}}} (\mathbf{v} \cdot \mathbf{n})_- \mathbf{v} \cdot \mathbf{w}_j \psi \,\mathrm{d}S \,\mathrm{d}t \\
&\forall\, \mathrm{j} \in \mathbb{N}.
\end{aligned}$$

This holds for all $\mathbf{w}_j$, $j = 1, .., \infty$, whose linear combination are dense in $\tilde{\mathbf{V}}$, therefore we can test by arbitrary $\boldsymbol{\varphi} \in \tilde{\mathbf{V}}$. Additionally the equation holds for all $\psi \in \mathbf{C}^\infty(0,T)$ and the whole integrand is in $L^1(0,T)$ a.e. All mentioned aspects imply existence of the velocity $\mathbf{v}$ belonging in spaces (1.16) and satisfying the weak formulation (1.13).

Energy inequality

We show that $\mathbf{v}$ satisfies the energy inequality. We start from Galerkin approximation for which we already have the energy equality in (2.33). We again integrate over $[0,T]$ and multiply by $\psi \in \mathbf{C}^\infty(0,T)$, such that $\psi \geq 0$ on $[0,T]$, to be able to pass to the limit.
Now we discuss the limiting procedure for all terms in (2.33).

$$\int_0^T \frac{\rho_*}{2} \|(\mathbf{v}^n - \mathbf{v}^*_{\text{in}})(t,\cdot)\|^2_{\mathbf{L}^2(\Omega)} \psi \,\mathrm{d}t \xrightarrow{n\to\infty} \int_0^T \frac{\rho_*}{2} \|(\mathbf{v} - \mathbf{v}^*_{\text{in}})(t,\cdot)\|^2_{\mathbf{L}^2(\Omega)} \psi \,\mathrm{d}t$$

as $\mathbf{v}^n \to \mathbf{v}$ in $L^2(0,T;\mathbf{L}^2_{0,\text{div}}(\Omega))$. Limit

$$\int_0^T \int_0^t \int_{\Gamma_{\text{wall}}} \mathbf{v}^n_\tau \cdot (\mathbf{v}^*_{\text{in}})_\tau \,\mathrm{d}S\psi \,\mathrm{d}s \,\mathrm{d}t \xrightarrow{n\to\infty} \int_0^T \int_0^t \int_{\Gamma_{\text{wall}}} \mathbf{v}_\tau \cdot (\mathbf{v}^*_{\text{in}})_\tau \,\mathrm{d}S\psi \,\mathrm{d}s \,\mathrm{d}t$$

as $\mathbf{v}^*_{\rm in} \in C((0,T)\times\overline{\Omega})$ and $\mathbf{v}^n_\tau \rightharpoonup \mathbf{v}_\tau$ in $L^2(0,T;\mathbf{L}^2(\Gamma_{\rm wall}))$. Limit

$$\int_0^T\int_0^t\int_{\Gamma_{\rm wall}} |\mathbf{v}^n_\tau|^2\,\mathrm{d}S\psi\,\mathrm{d}s\,\mathrm{d}t \xrightarrow{n\to\infty} \int_0^T\int_{\Gamma_{\rm wall}} |\mathbf{v}_\tau|^2\,\mathrm{d}S\psi\,\mathrm{d}t$$

as $\mathbf{v}^n_\tau \to \mathbf{v}_\tau$ in $L^2(0,T;L^2(\Gamma_{\rm wall})^2)$ (it is shown in (2.50) just for $\Gamma_{\rm out}$, but it holds for whole $\partial\Omega$, hence even for $\Gamma_{\rm wall}$). Limit

$$\int_0^T \frac{\rho_*}{2}\|(\mathbf{v}^n-\mathbf{v}^*_{\rm in})(0,\cdot)\|^2_{L^2(\Omega)}\psi\,\mathrm{d}t \xrightarrow{n\to\infty} \int_0^T \frac{\rho_*}{2}\|\mathbf{v}_0-\mathbf{v}^*_{\rm in}(0)\|^2_{L^2(\Omega)}\psi\,\mathrm{d}t$$

due to (2.29) and completeness of the orthogonal system $\{\mathbf{w}_i\}_{i=1}^\infty$ in $\mathbf{L}^2_{0,\rm div}(\Omega)$. Limit

$$\begin{aligned}&\int_0^T\int_0^t\int_\Omega \rho_*(\mathbf{v}^n-\mathbf{v}^*_{\rm in})\otimes(\mathbf{v}^n-\mathbf{v}^*_{\rm in}) : \nabla\mathbf{v}^*_{\rm in}\psi\,\mathrm{d}x\,\mathrm{d}s\,\mathrm{d}t\\ &\xrightarrow{n\to\infty} \int_0^T\int_0^t\int_\Omega \rho_*(\mathbf{v}-\mathbf{v}^*_{\rm in})\otimes(\mathbf{v}-\mathbf{v}^*_{\rm in}) : \nabla\mathbf{v}^*_{\rm in}\psi\,\mathrm{d}x\,\mathrm{d}s\,\mathrm{d}t\end{aligned}$$

follows from the limit procedure in section 2.2.2 and fact that $\nabla\mathbf{v}^*_{\rm in} \in L^\infty((0,T)\times\Omega)^{3\times3}$. Limits

$$\begin{aligned}&\int_0^T\int_0^t\int_\Omega \rho_*(\mathbf{v}^*_{\rm in}\otimes\mathbf{v}^*_{\rm in}) : \mathbb{D}(\mathbf{v}^n-\mathbf{v}^*_{\rm in})\psi\,\mathrm{d}x\,\mathrm{d}s\,\mathrm{d}t\\ &\xrightarrow{n\to\infty} \int_0^T\int_0^t\int_\Omega \rho_*(\mathbf{v}^*_{\rm in}\otimes\mathbf{v}^*_{\rm in}) : \mathbb{D}(\mathbf{v}-\mathbf{v}^*_{\rm in})\psi\,\mathrm{d}x\,\mathrm{d}s\,\mathrm{d}t,\\ &\int_0^T\int_0^t\int_\Omega 2\mu_*\mathbb{D}(\mathbf{v}^*_{\rm in}) : \mathbb{D}(\mathbf{v}^n-\mathbf{v}^*_{\rm in})\psi\,\mathrm{d}x\,\mathrm{d}s\,\mathrm{d}t\\ &\xrightarrow{n\to\infty} \int_0^T\int_0^t\int_\Omega 2\mu_*\mathbb{D}(\mathbf{v}^*_{\rm in}) : \mathbb{D}(\mathbf{v}-\mathbf{v}^*_{\rm in})\psi\,\mathrm{d}x\,\mathrm{d}s\,\mathrm{d}t,\\ &\int_0^T\int_0^t\int_\Omega \rho_*\frac{\partial\mathbf{v}^*_{\rm in}}{\partial t}\cdot(\mathbf{v}^n-\mathbf{v}^*_{\rm in})\psi\,\mathrm{d}x\,\mathrm{d}s\,\mathrm{d}t\\ &\xrightarrow{n\to\infty} \int_0^T\int_0^t\int_\Omega \rho_*\frac{\partial\mathbf{v}^*_{\rm in}}{\partial t}\cdot(\mathbf{v}-\mathbf{v}^*_{\rm in})\psi\,\mathrm{d}x\,\mathrm{d}s\,\mathrm{d}t,\end{aligned}$$

due to properties of $\mathbf{v}^*_{\rm in}$ stated in (1.15) and due to $\mathbf{v}^n-\mathbf{v}^*_{\rm in} \rightharpoonup \mathbf{v}-\mathbf{v}^*_{\rm in}$ in $L^2(0,T;\tilde{\mathbf{V}})$ from (2.36). Limit

$$P(t)\int_0^T\int_0^t\int_{\Gamma_{\rm out}} \mathbf{v}^n\cdot\mathbf{n}\psi\,\mathrm{d}S\,\mathrm{d}s\,\mathrm{d}t \xrightarrow{n\to\infty} P(t)\int_0^T\int_0^t\int_{\Gamma_{\rm out}} \mathbf{v}\cdot\mathbf{n}\psi\,\mathrm{d}S\,\mathrm{d}s\,\mathrm{d}t$$

due to (2.50). Applying twice the Fatou lemma for non-negative sequences, which converges pointwise and due to n-independent estimates coming from (2.34) we can write for selected subsequences simultaneously limits for two terms in (2.30) as

$$\begin{aligned}&\liminf_{n\to\infty}\int_0^T\left(\int_0^t 2\mu_*\|\mathbb{D}(\mathbf{v}^n-\mathbf{v}^*_{\rm in})\|^2_{L^2(\Omega)}\,\mathrm{d}s+\int_0^t\int_{\Gamma_{\rm out}}\frac{|\mathbf{v}^n|^2}{2}(\mathbf{v}^n\cdot\mathbf{n})_+\,\mathrm{d}S\,\mathrm{d}s\right)\psi\,\mathrm{d}t\\ &\geq\int_0^T\liminf_{n\to\infty}\left(\int_0^t 2\mu_*\|\mathbb{D}(\mathbf{v}^n-\mathbf{v}^*_{\rm in})\|^2_{L^2(\Omega)}\,\mathrm{d}s+\int_0^t\int_{\Gamma_{\rm out}}\frac{|\mathbf{v}^n|^2}{2}(\mathbf{v}^n\cdot\mathbf{n})_+\,\mathrm{d}S\,\mathrm{d}s\right)\psi\,\mathrm{d}t\\ &\geq\int_0^T\left(\int_0^t 2\mu_*\|\mathbb{D}(\mathbf{v}-\mathbf{v}^*_{\rm in})\|^2_{L^2(\Omega)}\,\mathrm{d}s+\int_0^t\int_{\Gamma_{\rm out}}\frac{|\mathbf{v}|^2}{2}(\mathbf{v}\cdot\mathbf{n})_+\,\mathrm{d}S\,\mathrm{d}s\right)\psi\,\mathrm{d}t,\end{aligned}$$

Due to limits of these terms we get energy inequality instead of equality as in (2.33). Altogether, choosing ψ as a mollifier ω_ϵ in time and passing $\epsilon \to 0$ we finally obtain

$$\begin{aligned}
&\frac{\rho_*}{2}\|(\mathbf{v}-\mathbf{v}^*_{\text{in}})(t,\cdot)\|^2_{\mathbf{L}^2(\Omega)} + 2\mu_* \int_0^t \|\mathbb{D}(\mathbf{v}-\mathbf{v}^*_{\text{in}})\|^2_{\mathbf{L}^2(\Omega)}\,\mathrm{d}s \\
&+ \frac{\theta}{\gamma_*(1-\theta)}\int_0^t\int_{\Gamma_{\text{wall}}} |\mathbf{v}_\tau|^2\,\mathrm{d}S\,\mathrm{d}s + \int_0^t\int_{\Gamma_{\text{out}}} \frac{|\mathbf{v}|^2}{2}(\mathbf{v}\cdot\mathbf{n})_+\,\mathrm{d}S\,\mathrm{d}s \\
&\le \frac{\rho_*}{2}\|\mathbf{v}_0-\mathbf{v}^*_{\text{in}}(0)\|^2_{\mathbf{L}^2(\Omega)} + \frac{\theta}{\gamma_*(1-\theta)}\int_0^t\int_{\Gamma_{\text{wall}}} \mathbf{v}_\tau\cdot(\mathbf{v}^*_{\text{in}})_\tau\,\mathrm{d}S\,\mathrm{d}s \\
&- \int_0^t\int_\Omega \rho_*(\mathbf{v}-\mathbf{v}^*_{\text{in}})\otimes(\mathbf{v}-\mathbf{v}^*_{\text{in}}) : \nabla\mathbf{v}^*_{\text{in}}\,\mathrm{d}x\,\mathrm{d}s \\
&+ \int_0^t\int_\Omega \rho_*(\mathbf{v}^*_{\text{in}}\otimes\mathbf{v}^*_{\text{in}}) : \mathbb{D}(\mathbf{v}-\mathbf{v}^*_{\text{in}})\,\mathrm{d}x\,\mathrm{d}s - \int_0^t\int_\Omega \rho_*\frac{\partial\mathbf{v}^*_{\text{in}}}{\partial t}\cdot(\mathbf{v}-\mathbf{v}^*_{\text{in}})\,\mathrm{d}x\,\mathrm{d}s \\
&- P(t)\int_0^t\int_{\Gamma_{\text{in}}} \mathbf{v}\cdot\mathbf{n}\,\mathrm{d}S\,\mathrm{d}s - 2\mu_*\int_0^t\int_\Omega \mathbb{D}(\mathbf{v}^*_{\text{in}}) : \mathbb{D}(\mathbf{v}-\mathbf{v}^*_{\text{in}})\,\mathrm{d}x\,\mathrm{d}s,
\end{aligned}$$

for a.a. $t \in (0,T)$, giving the energy inequality for weak solution $\mathbf{v}$.

Initial condition

We use following lemma, see lecture notes [31].

Lemma 2. *Let X, Y be Banach spaces, X reflexive space and $X \hookrightarrow Y$ densely. Let $\phi \in L^\infty(0,T;X) \cap C([0,T];Y_{weak})$. Then $\phi \in C([0,T];X_{weak})$.*

Where $\phi \in C([0,T];X_{weak})$ has the meaning

$$\langle F, \phi(t)\rangle_{X^*,X} \xrightarrow{t\to t_0} \langle F, \phi(t_0)\rangle_{X^*,X} \qquad \text{for all } F \in X^*. \tag{2.51}$$

For us let $X = \mathbf{L}^2_{0,\text{div}}(\Omega)$, $Y = \tilde{\mathbf{V}}^*$. We know that $\mathbf{v}-\mathbf{v}^*_{\text{in}} \in L^\infty\left(0,T;\mathbf{L}^2_{0,\text{div}}(\Omega)\right)$ and even $\mathbf{v}-\mathbf{v}^*_{\text{in}} \in C\left([0,T];\tilde{\mathbf{V}}^*\right)$, since $\mathbf{v}, \frac{\partial\mathbf{v}}{\partial t} \in L^2\left(0,T;\tilde{\mathbf{V}}^*\right)$. Therefore $\mathbf{v} \in C\left([0,T];(\mathbf{L}^2_{0,\text{div}}(\Omega))_{weak}\right)$ and also (see [31])

$$\mathbf{v} \in C\left([0,T];(\mathbf{L}^2(\Omega))_{weak}\right). \tag{2.52}$$

Now take weak formulation for Galerkin approximation (2.30), integrate over $[0,T]$ and multiply by $\psi \in \mathbf{C}^\infty(0,T)$, such that $\psi(T) = 0$. We integrate by parts the term with time derivative, i.e.

$$\int_0^T\int_\Omega \frac{\partial\mathbf{v}^n}{\partial t}\cdot\mathbf{w}_j\psi\,\mathrm{d}x\,\mathrm{d}t = -\int_0^T\int_\Omega \mathbf{v}^n\cdot\mathbf{w}_j\frac{\partial\psi}{\partial t}\,\mathrm{d}x\,\mathrm{d}t - \int_\Omega \mathbf{v}^n(0)\cdot\mathbf{w}_j\psi(0)\,\mathrm{d}x$$

Passing to the limit as we already showed in section 2.2.2, we get for $\boldsymbol{\varphi} \in \tilde{\mathbf{V}}$

$$\int_0^T\int_\Omega \frac{\partial\mathbf{v}^n}{\partial t}\cdot\mathbf{w}_j\psi\,\mathrm{d}x\,\mathrm{d}t \xrightarrow{n\to\infty} -\int_0^T\int_\Omega \mathbf{v}\cdot\boldsymbol{\varphi}\frac{\partial\psi}{\partial t}\,\mathrm{d}x\,\mathrm{d}t - \int_\Omega \mathbf{v}_0\cdot\boldsymbol{\varphi}\psi(0)\,\mathrm{d}x \tag{2.53}$$

due to (2.29). On the other hand, taking the weak formulation (1.13) for $\mathbf{v}$, again integrate over $[0,T]$ and multiply by $\psi \in \mathbf{C}^\infty(0,T)$, such that $\psi(T) = 0$, we get using integration by parts on the term with time derivative

$$\begin{aligned}
&\int_0^T \left\langle \frac{\partial\mathbf{v}}{\partial t}, \boldsymbol{\varphi}\right\rangle \psi\,\mathrm{d}t = \int_0^T \frac{d}{dt}\langle\mathbf{v},\boldsymbol{\varphi}\rangle\,\psi\,\mathrm{d}t = \int_0^T \frac{d}{dt}\left(\int_\Omega \mathbf{v}\cdot\boldsymbol{\varphi}\,\mathrm{d}x\right)\psi\,\mathrm{d}t = \\
&-\int_0^T \left(\int_\Omega \mathbf{v}\cdot\boldsymbol{\varphi}\,\mathrm{d}x\right)\frac{d\psi}{dt}\,\mathrm{d}t - \int_\Omega \mathbf{v}(0)\cdot\boldsymbol{\varphi}\psi(0)\,\mathrm{d}x,
\end{aligned}$$

due to weak continuity in time (2.52). Together comparing with (2.53) we get for arbitrary $\psi(0)$

$$\int_\Omega \mathbf{v}(0)\cdot\boldsymbol{\varphi}\,\mathrm{d}x = \int_\Omega \mathbf{v}_0\cdot\boldsymbol{\varphi}\,\mathrm{d}x. \tag{2.54}$$

Moreover,

$$\liminf_{t\to 0^+}\int_\Omega |\mathbf{v}(t)|^2\,\mathrm{d}x \geq \int_\Omega |\mathbf{v}_0|^2\,\mathrm{d}x \tag{2.55}$$

from weak convergence $\mathbf{v}(t)\rightharpoonup\mathbf{v}_0$ as $t\to 0^+$ in $\mathbf{L}^2(\Omega)$ obtained through (2.52) and (2.54). Also from energy inequality (1.17) follows

$$\limsup_{t\to 0^+}\int_\Omega |\mathbf{v}(t)|^2\,\mathrm{d}x \leq \int_\Omega |\mathbf{v}_0|^2\,\mathrm{d}x,$$

hence together we get convergence of norms: $\lim_{t\to 0^+}\|\mathbf{v}(t)\|_{L^2(\Omega)} = \|\mathbf{v}_0\|_{\mathbf{L}^2(\Omega)}$. Therefore finally

$$\lim_{t\to 0^+}\|\mathbf{v}(t)-\mathbf{v}_0\|^2_{L^2(\Omega)} = \lim_{t\to 0^+}\|\mathbf{v}(t)\|^2_{L^2(\Omega)} - \lim_{t\to 0^+} 2(\mathbf{v}(t),\mathbf{v}_0) + \lim_{t\to 0^+}\|\mathbf{v}_0\|^2_{L^2(\Omega)} = 0.$$

Which ends the proof of the theorem (1).

3. Numerical computations

So far we described physical problem of the flow in the aortic root by a mathematical model consisting of partial differential equations given in (1.1)-(1.3) with initial and boundary conditions (1.4)-(1.8). Generally we can not obtain the analytical solution to these equations. Therefore we must compute them numerically and obtain an approximate solution. This chapter presents how is the weak formulation (1.13) treated for numerical implementation and how it is discretised in time and space. We are using the finite element method for space discretisation. We also describe in detail chosen finite elements for our computations, which are the Taylor-Hood finite element and the divergence-free Raviart-Thomas and Brezzi-Douglas-Marini finite elements and we discuss their properties. Another section covers the analytical description of the domain of the aortic root to get the final computational mesh. Lastly, we deal with the construction of better than piecewise linear approximation of the boundary of the computational mesh.

3.0.1 Software tools

A significant part of this thesis involved the development of scripts for numerical computation of the flow in the aortic root, with all the modifications such as implementing the $\mathbf{H}(\mathrm{div}, \Omega)$-conforming finite element formulation (section 3.2.3), prescribing the geometry with three sinuses (section 3.3) and using higher polynomial approximation of the boundary (section 3.4). All numerical simulations and graphs presented in this thesis were generated using these scripts, which are available on Gitlab https://gitlab.karlin.mff.cuni.cz/kosarkova/diplomka. The scripts are written in Python programming language with use of the Firedrake library [21], an automated system for solving partial differential equations using the finite element method and the PETSc library [14], which handles the numerical algebra procedures behind and the parallel computation. Software Gmsh [19] was used for generating all meshes. The codes were running on the computational cluster Sněhurka.

3.1 Nitsche's method

For the numerical implementation, it is necessary to incorporate the weak formulation of the incompressibility condition (1.14) to the weak formulation (1.13). Simultaneously, the function space $\mathbf{W}^{1,2}_{\mathrm{div,\,bc}}$ should be replaced by $\mathbf{W}^{1,2}_{\mathrm{bc}}$.
When imposing the Navier's slip boundary condition (1.8), while specifying the tangential velocity component at the wall, it is also necessary to impose the impermeability condition (1.7), which constrains the normal velocity component at the wall as Dirichlet type boundary condition. However in some cases for arbitrary curved domain Ω, the numerical implementation of such boundary condition in a strong sense is complicated (i.e. such that it is contained in the space $\mathbf{W}^{1,2}_{\mathrm{bc}}$). Instead, it is more convenient to be enforced weakly by incorporating into the weak formulation. The suitable method for imposition of this type of boundary conditions in weak sense was first introduced by [30] [1].

[1] Note that for example the $\mathbf{H}(\mathrm{div}, \Omega)$-nonconforming finite element spaces allow the strong imposition of Dirichlet boundary conditions on the normal component, however there are other

Derivation of the Nitsche's method. There are several options how to derive the weak formulation using Nitche's method. We will show one of the approach, presented in [3], suitable for simple Newtonian model (1.3) of a fluid.
Denote space

$$\hat{\mathbf{V}} := \{\boldsymbol{\phi} \in \mathbf{V};\ \boldsymbol{\phi} = \mathbf{0} \text{ on } \Gamma_{\mathrm{D}}\}, \tag{3.1}$$

where $\mathbf{V}$ is defined as (1.10), Γ_{D} denotes parts of the boundary where Dirichlet boundary conditions are imposed strongly, thus here $\Gamma_{\mathrm{D}} = \Gamma_{\mathrm{in}}$.
Now we show how to modify the weak formulation to weakly impose the Dirichlet boundary condition on normal components on Γ_{wall}. We proceed in similar manner as in derivation of the weak formulation in 1.2, but now with test functions $\boldsymbol{\phi} \in \hat{\mathbf{V}}$, we get

$$\begin{aligned}\rho_* \left\langle \frac{\partial \mathbf{v}}{\partial t}, \boldsymbol{\phi} \right\rangle + \rho_* \int_\Omega (\nabla \mathbf{v})\,\mathbf{v} \cdot \boldsymbol{\phi}\,\mathrm{d}x - \int_\Omega p\mathbb{I} : \nabla \boldsymbol{\phi}\,\mathrm{d}x \\ + 2\mu_* \int_\Omega \mathbb{D}(\mathbf{v}) : \nabla \boldsymbol{\phi}\,\mathrm{d}x - \int_\Omega q \operatorname{div} \mathbf{v}\,\mathrm{d}x \\ = \int_{\Gamma_{\mathrm{out}}} \mathbb{T}\mathbf{n} \cdot \boldsymbol{\phi}\,\mathrm{d}S + \int_{\Gamma_{\mathrm{wall}}} (\mathbb{T}\mathbf{n})_\tau \cdot \boldsymbol{\phi}_\tau\,\mathrm{d}S + \int_{\Gamma_{\mathrm{wall}}} (\mathbb{T}\mathbf{n})_n \cdot \boldsymbol{\phi}_n\,\mathrm{d}S.\end{aligned}$$

Now lets us focus on the fourth and the fifth term. Due to the symmetry of $\mathbb{D}$ and observation $\mathbb{I} : \nabla \mathbf{v} = \operatorname{tr}(\mathbf{v}) = \operatorname{div} \mathbf{v}$, they can be written as

$$\begin{aligned}\int_\Omega 2\mu_* \mathbb{D}(\mathbf{v}) : \nabla \boldsymbol{\phi}\,\mathrm{d}x - \int_\Omega q \operatorname{div} \mathbf{v}\,\mathrm{d}x &= \int_\Omega 2\mu_* \mathbb{D}(\mathbf{v}) : \mathbb{D}(\boldsymbol{\phi})\,\mathrm{d}x - \int_\Omega q\mathbb{I} : \nabla \mathbf{v}\,\mathrm{d}x \\ &= \int_\Omega 2\mu_* \nabla \mathbf{v} : \mathbb{D}(\boldsymbol{\phi})\,\mathrm{d}x - \int_\Omega q\mathbb{I} : \nabla \mathbf{v}\,\mathrm{d}x \\ &= \int_\Omega [-q\mathbb{I} + 2\mu_* \mathbb{D}(\boldsymbol{\phi})] : \nabla \mathbf{v}\,\mathrm{d}x \\ &= \int_\Omega \mathbb{T}(q, \boldsymbol{\phi}) : \nabla \mathbf{v}\,\mathrm{d}x \end{aligned} \tag{3.2}$$

Where we denoted

$$\mathbb{T}(q, \boldsymbol{\phi}) := -q\mathbb{I} + 2\mu_* \mathbb{D}(\boldsymbol{\phi}),$$

which is the Cauchy stress tensor for the test functions $q, \boldsymbol{\phi}$.

$$\begin{aligned}\int_\Omega \mathbb{T}(q, \boldsymbol{\phi}) : \nabla \mathbf{v}\,\mathrm{d}x = -\int_\Omega \operatorname{div} \mathbb{T}(q, \boldsymbol{\phi}) \cdot \mathbf{v}\,\mathrm{d}x + \int_{\Gamma_{\mathrm{in}}} \mathbb{T}(q, \boldsymbol{\phi})\mathbf{n} \cdot \mathbf{v}\,\mathrm{d}S \\ + \int_{\Gamma_{\mathrm{out}}} \mathbb{T}(q, \boldsymbol{\phi})\mathbf{n} \cdot \mathbf{v}\,\mathrm{d}S + \int_{\Gamma_{\mathrm{wall}}} (\mathbb{T}(q, \boldsymbol{\phi})\mathbf{n})_\tau \cdot \mathbf{v}_\tau\,\mathrm{d}S \\ + \int_{\Gamma_{\mathrm{wall}}} (\mathbb{T}(q, \boldsymbol{\phi})\mathbf{n})_n \cdot \mathbf{v}_n\,\mathrm{d}S.\end{aligned}$$

Here we can set the Dirichlet boundary condition (for now in general case) as $\mathbf{v}_n\big|_{\Gamma_{\mathrm{wall}}} = (\mathbf{v}_n)_D$ and velocity on Γ_{in}, Γ_{out}, and tangential velocity component on Γ_{wall} leave unspecified. Now apply integration per pares once again on the term $-\int_\Omega \operatorname{div} \mathbb{T}(q, \boldsymbol{\phi}) \cdot \mathbf{v}\,\mathrm{d}x$, where terms on Γ_{in}, Γ_{out} and tangential term on Γ_{wall} cancels out and there remains

$$\int_\Omega \mathbb{T}(q, \boldsymbol{\phi}) : \nabla \boldsymbol{\phi}\,\mathrm{d}x = \int_\Omega \mathbb{T}(q, \boldsymbol{\phi}) : \nabla \boldsymbol{\phi}\,\mathrm{d}x - \int_{\Gamma_{\mathrm{wall}}} (\mathbb{T}(q, \boldsymbol{\phi})\mathbf{n})_n \cdot (\mathbf{v}_n - (\mathbf{v}_n)_D)\,\mathrm{d}S.$$

obstacles with these spaces, which will be more discussed in chapter 3.2.3

Using again identity (3.2), putting everything together we get

$$\begin{aligned}\rho_* \left\langle \frac{\partial \mathbf{v}}{\partial t}, \boldsymbol{\phi} \right\rangle + \rho_* \int_\Omega (\nabla\, \mathbf{v})\, \mathbf{v} \cdot \boldsymbol{\phi}\, \mathrm{d}x - \int_\Omega \mathbb{T}(p, \mathbf{v}) : \nabla\, \boldsymbol{\phi}\, \mathrm{d}x - \int_\Omega q \operatorname{div} \mathbf{v}\, \mathrm{d}x \\ - \int_{\Gamma_{\text{wall}}} (\mathbb{T}(p, \mathbf{v})\mathbf{n})_n \cdot \boldsymbol{\phi}_n\, \mathrm{d}S - \int_{\Gamma_{\text{wall}}} (\mathbb{T}(q, \boldsymbol{\phi})\mathbf{n})_n \cdot (\mathbf{v}_n - (\mathbf{v}_n)_D)\, \mathrm{d}S \\ = \int_{\Gamma_{\text{out}}} \mathbb{T}(p, \mathbf{v})\mathbf{n} \cdot \boldsymbol{\phi}\, \mathrm{d}S + \int_{\Gamma_{\text{wall}}} (\mathbb{T}(p, \mathbf{v})\mathbf{n})_\tau \cdot \boldsymbol{\phi}_\tau\, \mathrm{d}S.\end{aligned}$$

Penalisation term. Such weak formulation is consistent with (1.13), however [30] showed it is not stable. For stabilising, one must add consistent penalisation term

$$\frac{\mu_* \beta}{h} \int_{\Gamma_{\text{wall}}} (\mathbf{v}_n - (\mathbf{v}_n)_D) \cdot \boldsymbol{\phi}_n\, \mathrm{d}S, \tag{3.3}$$

where h denotes the local size of mesh edge and $\beta > 0$ is the stabilisation parameter. The parameter must be determined experimentally based on the specific problem. It should not be very small to ensure stability, yet it should not be too large so it doesn't make all other terms less relevant.

Weak formulation using symmetric Nitche's method. All together substituting for (1.8), (1.6), that is also use the impermeability condition $\mathbf{v}_n\big|_{\Gamma_{\text{wall}}} = (\mathbf{v}_n)_D = 0$ and adding the penalisation term (3.3), we obtain the weak formulation in the form:

Definition 2 (Weak solution)**.** *Find* $(\mathbf{v} - \mathbf{v}^*_{\text{in}}, p) \in L^\infty(0, T; \mathbf{L}^2(\Omega)) \cap L^2(0, T; \hat{\mathbf{V}}) \times L^{5/4}(0, T; L^2(\Omega))$ *such that*

$$\begin{aligned}&\rho_* \left\langle \frac{\partial \mathbf{v}}{\partial t}, \boldsymbol{\phi} \right\rangle + \rho_* \int_\Omega (\nabla \mathbf{v})\mathbf{v} \cdot \boldsymbol{\phi}\, \mathrm{d}x - \int_\Omega p \operatorname{div} \boldsymbol{\phi}\, \mathrm{d}x + 2\mu_* \int_\Omega \mathbb{D}(\mathbf{v}) : \mathbb{D}(\boldsymbol{\phi})\, \mathrm{d}x \\ &- \int_\Omega q \operatorname{div} \mathbf{v}\, \mathrm{d}x - \int_{\Gamma_{\text{wall}}} (\mathbb{T}(p, \mathbf{v})\mathbf{n})_n \cdot \boldsymbol{\phi}_n\, \mathrm{d}S - \int_{\Gamma_{\text{wall}}} (\mathbb{T}(q, \boldsymbol{\phi})\mathbf{n})_n \cdot \mathbf{v}_n\, \mathrm{d}S \\ &+ \frac{\mu_* \beta}{h} \int_{\Gamma_{\text{wall}}} \mathbf{v}_n \cdot \boldsymbol{\phi}_n\, \mathrm{d}S + \frac{\theta}{\gamma_*(1-\theta)} \int_{\Gamma_{\text{wall}}} \mathbf{v}_\tau \cdot \boldsymbol{\phi}_\tau\, \mathrm{d}S \\ &+ P(t) \int_{\Gamma_{\text{out}}} \boldsymbol{\phi} \cdot \mathbf{n}\, \mathrm{d}S - \frac{\rho_*}{2} \int_{\Gamma_{\text{out}}} (\mathbf{v} \cdot \mathbf{n})_- \mathbf{v} \cdot \boldsymbol{\phi}\, \mathrm{d}S = 0,\end{aligned} \tag{3.4}$$

valid for all $(\mathbf{w}_h, q) \in \hat{\mathbf{V}} \times L^2(\Omega)$ *and a.a.* $t \in (0, T)$ [2]

Since terms $-\int_{\Gamma_{\text{wall}}} (\mathbb{T}(p, \mathbf{v})\mathbf{n})_n \cdot \boldsymbol{\phi}_n\, \mathrm{d}S$ and $-\int_{\Gamma_{\text{wall}}} (\mathbb{T}(q, \boldsymbol{\phi})\mathbf{n})_n \cdot \mathbf{v}_n\, \mathrm{d}S$ have same sign, method is denoted as *symmetric Nitsche's method*. However, [8] showed, there also exist *nonsymmetric Nitsche method* having $+\int_{\Gamma_{\text{wall}}} (\mathbb{T}(q, \boldsymbol{\phi})\mathbf{n})_n \cdot \mathbf{v}_n\, \mathrm{d}S$ in weak formulation (2). Such variant is stable even without penalisation term (3.3). Based on our experiments, symmetric Nitsche's method with appropriate penalty β gave very similar or even more accurate results in comparison to nonsymmetric Nitsche's method. Therefore our further tests will be provided only with the symmetric one.

[2] Note that here we consider also pressure as opposed to the definition (1), where it was not part of the analysis. According to [9], space $L^{5/4}(0, T; L^2(\Omega))$ for pressure should be reasonable.

3.2 Discretisation

To numerically compute the solution $\mathbf{v}$, p, the weak formulation in (2) must be discretised.

Discretisation in time Consider partition of time $0 = t_0 < t_1 .. < t_N$ of the time interval $[0, T]$ and set fixed time step $\Delta t = t_k - t_{k-1}$ for $k = 1, .., N$.
Consider differential equation of form

$$\frac{\partial \mathbf{u}}{\partial t} = G(\mathbf{u}), \quad \mathbf{u}(0) = \mathbf{0}.$$

Backward Euler method. The time derivative can be discretised by Backward Differentiation Formula of the first order (BDF1) denoted as *Backward Euler method*. It is a stable implicit method and the time derivate is approximated as

$$\frac{\partial \mathbf{u}}{\partial t} \approx \frac{1}{\Delta t}\left(\mathbf{u}^k - \mathbf{u}^{k-1}\right) = G(\mathbf{u}^k), \tag{3.5}$$

where we denote $\mathbf{u}^i := \mathbf{u}(t_i)$ and we set $\mathbf{u}^0 = \mathbf{0}$.

Backward Differentiation Formula of the second order. To get higher order accuracy in time, we consider also *Backward Differentiation Formula of the second order* (BDF2) an implicit stable method, which approximates the derivative as

$$\frac{\partial \mathbf{u}}{\partial t} \approx \frac{1}{\Delta t}\left(\frac{3}{2}\mathbf{u}^k - 2\mathbf{u}^{k-1} + \frac{1}{2}\mathbf{u}^{k-2}\right) = G(\mathbf{u}^k). \tag{3.6}$$

For initialisation we star from zero solution, i.e. $\mathbf{u}^{-1} = \mathbf{u}^0 = 0$.
For numerical simulations in this thesis we use BDF2 scheme, to eventually get same order of accuracy in time as in space.

Discretisation in space Finite element method is used for discretisation in space. Let us consider Ω_h an approximation of the domain Ω (more specified in section 3.2.1). Over Ω_h we construct finite-dimensional spaces $Q_h \subset L^2(\Omega)$, $\mathbf{X}_h \approx \mathbf{V}$, $\hat{\mathbf{X}}_h \approx \hat{\mathbf{V}}$, where $\mathbf{V}$, $\hat{\mathbf{V}}$ are defined in (1.10), (3.1), such that $\mathbf{X}_h, \hat{\mathbf{X}}_h \subset \mathbf{L}^2(\Omega)$ for general non-conforming finite element spaces. Let $\hat{\mathbf{X}}_h$ be of dimension N_v with basis $\{\boldsymbol{\varphi}_i\}_{i=1}^{N_v}$ and Q_h of dimension N_p, with basis $\{q_i\}_{i=1}^{N_p}$. Spaces $\hat{\mathbf{X}}_h$ and Q_h should satisfy the discrete inf-sup condition called the *Babuška Brezzi condition* ([5]) to obtain a uniquely solvable discrete problem. Special choice of these spaces will be discussed in next section 3.2.1.
On each time-step t_k, for $k = 1, .., N$, we look for $\mathbf{v}_h^k \in \mathbf{X}_h$ and $p^k \in Q_h$ in a form

$$\mathbf{v}_h^k = (\mathbf{v}_{\text{in}}^*)_h^k + \sum_{i=1}^{Nv} V_i^k \, \boldsymbol{\varphi}_i, \tag{3.7}$$

$$p^k = \sum_{i=1}^{Np} P_i^k \, q_i, \tag{3.8}$$

where $(\mathbf{v}_{\text{in}}^*)_h^k = (\mathbf{v}_{\text{in}}^*)_h(t_k) \in \mathbf{X}_h$ in each time-step is an approximation of $\mathbf{v}_{\text{in}}^*$ defined in (1.15) where $\mathbf{v}_{in}$ is known from (1.5). Further, for simplification of notation, let us denote

$$\mathbf{v}_h - (\mathbf{v}_{\text{in}}^*)_h^k := \hat{\mathbf{v}}_h \tag{3.9}$$

and from (3.7) we look in each time-step t_k, $k = 1, .., N$, for the coefficients V_i^k of the velocity $\hat{\mathbf{v}}_h^k \in \hat{\mathbf{X}}_h$.

Finite-dimensional variational problem. We apply the spatial discretization to the weak formulation in (2), using test functions as basis functions of $\hat{\mathbf{X}}_h$, Q_h, while also incorporating the BDF2 scheme specified in (3.6). Then we look for the approximate velocity $\hat{\mathbf{v}}_h^k \in \hat{\mathbf{X}}_h$ and approximate pressure $p_h^k \in Q_h$, such that in each time-step t_k for $k = 1, .., N$ they satisfy the discrete weak formulation, which can be after standard manipulations generally written as system of non-linear algebraic equations of the form

$$\mathbf{F}(\mathbf{V}_h^k, \mathbf{P}_h^k) = \mathbf{0}, \quad \text{for } k = 1, .., N, \tag{3.10}$$

where $\mathbf{V}_h^k = (V_1^k, .., V_{N_v}^k)$ and $\mathbf{P}_h^k = (P_1^k, .., P_{N_p}^k)$ are vectors of coefficients from (3.7), (3.8).

Newton method. Defining $\mathbf{x}^k = (\mathbf{V}_h^k, \mathbf{P}_h^k)$, solving such system by *Newton method* for each $k = 1, .., N$ leads to

$$\mathbf{x}_{n+1}^k = \mathbf{x}_n^k - \left(J_n^k\right)^{-1} \mathbf{F}(\mathbf{x}_n^k), \quad \text{for } n = 1, 2, ..,$$

where J_n^k denotes the Jacobian, $J_n^k = \frac{\partial \mathbf{F}}{\partial \mathbf{x}}(\mathbf{x}_n^k)$, in k-th time-step in point $\mathbf{x}_n^k$. Practically we compute in each time-step t_k, $k = 1, .., N$, linear algebraic system

$$J_n^k \Delta \mathbf{x}_n^k = -\mathbf{F}(\mathbf{x}_n^k), \quad \text{for } n = 1, 2, .., \tag{3.11}$$

for $\Delta \mathbf{x}_n = \mathbf{x}_{n+1}^k - \mathbf{x}_n^k$. For each $n = 1, 2, ..$ the linear system (3.11) is solved directly by MUMPS solver [2]. The newton iterations are then stopped when the residuum $r_n^k = \|\mathbf{F}(\mathbf{x}_n^k)\|$ satisfies the absolute tolerance $r_n^k \leq 10^{-10}$ or the relative tolerance $\frac{r_n^k}{\|\mathbf{x}_n^k\|} \leq 10^{-10}$ for each $k = 1, .., N$.
This classical Newton method is used for numerical computations of Couette flow in section 4.1.1 and Poiseuille flow in section 4.1.2. However in three dimensional non-stationary numerical simulations of flow in the aortic root, direct computation of the linear system (3.11) for each $k = 1, .., N$ and $n = 1, 2, ..$ are the most time consuming operations in whole computation. Therefore in this case the so called *lagged Jacobian method* is used. That is the Jacobian is not evaluated in every step n as in Newton method, instead it is kept from the previous step. If more than 10 iterations are needed to solve the non-linear problem, the Jacobian is recomputed. However it can also happen that it is kept to next time-step.
In simulations of flow in the aortic root we compute to the fixed time $T = 5$ s or we can also stop the computation if the steady solution is reached, that means we stop at time t_k, if the time derivative is under some tolerance, in our case $\rho_* \frac{\|\mathbf{v}_h^k - \mathbf{v}_h^{k-1}\|_{L^2}}{\Delta t} \leq 10^{-3}$.

3.2.1 Finite element method

The problem is numerically solved by the finite element method (FEM) in space, a very frequent method for solving partial differential equations. Previous section

provided general process how to get from variational formulation in (2) to finite-dimensional system represented as (3.11) through finite-dimensional spaces $\mathbf{X}_h$ and Q_h. This section will introduce the basic definitions and theorems behind the theory and also selection of the spaces $\mathbf{X}_h$ and Q_h. All the definitions, details and proofs are provided in [12]. A brief overview about finite element method can be found, for example, in [38].
Firstly, domain $\overline{\Omega}$ is approximated by polyhedral domain $\overline{\Omega}_h$, which is split into subdomains T which build the *triangulation* $\mathcal{T}_h$ of the domain Ω_h with boundary $\partial\Omega_h$ consisting of Γ^h_{in}, Γ^h_{wall}, Γ^h_{out}. We assume

- ($\mathcal{T}_h$1) Each set T from $\mathcal{T}_h$ is closed with non-empty and connected interior.
- ($\mathcal{T}_h$2) The boundary ∂T of each $T \in \mathcal{T}_h$ is Lipschitz continuous.
- ($\mathcal{T}_h$3) $\overline{\Omega_h} = \bigcup_{T\in\mathcal{T}_h} T$
- ($\mathcal{T}_h$4) The intersection of interiors of two different sets from $\mathcal{T}_h$ is empty.

Definition 3 (General definition of the finite element)**.** *The finite element in $\mathbb{R}^n$ is a triple (T, P, Σ), where*

- *T is an bounded closed subset of $\mathbb{R}^n$ with non-empty connected interior and Lipschitz continuous boundary.*
- *P is a finite-dimensional function space on element T.*
- *$\Sigma = \{l_i, i = 1, .., N\}$, is the set of linear functionals over the space P, such that Σ is P-unisolvent.*

Then $p_1, .., p_N$ are basis function of the finite element and $l_1, .., l_N$ are degrees of freedoms of the finite element, such that $l_i(p_j) = \delta_{ij}$ for $i, j = 1, .., N$. It holds that

$$p = \sum_{i=1}^{N} l_i(p)p_i \quad \forall p \in P.$$

If the functionals from Σ are defined on space $Q(T) \supset P$, the *local interpolation operator* $\Pi : Q(T) \to P$ can be defined as

$$\Pi v = \sum_{i=1}^{N} l_i(v)p_i, \quad \text{for } v \in Q(T). \tag{3.12}$$

It holds that $\Pi p = p$ for $\forall p \in P$, hence Π is a projection. Function Πv is called the *P-interpolation* of function v.
If Σ has the meaning of evaluation of function at a point a_i, i.e. $\phi_i(v) = v(a_i)$, $i = 1, .., N$, then we talk about *Lagrange interpolation* and hence it must hold that the definition domain of the interpolation operator $\mathcal{D}(\Pi) = C(T)$.
Given a regular mapping $\mathbf{F}_T$, one can generate system made of finite elements (T, P_T, Σ_T) from reference finite element $\left(\hat{T}, \hat{P}, \hat{\Sigma}\right)$. The mapping $\mathbf{F}_T$ is usually used as *affine regular*, that means $\mathbf{F}_T : \mathbb{R}^n \to \mathbb{R}^n$ satisfying

$$\mathbf{F}_T(\hat{\mathbf{x}}) = \mathbb{B}\hat{\mathbf{x}} + \mathbf{b}, \tag{3.13}$$

for regular matrix $\mathbb{B}^{n\times n}$, vector $\mathbf{b} \in \mathbb{R}^n$ and $\hat{\mathbf{x}}$ denoting point in reference element $\hat{T}$.

Definition 4 (Affine equivalent finite elements)**.** *Two finite elements* $\left(\hat{T}, \hat{P}, \hat{\Sigma}\right)$, (T, P_T, Σ_T) *are affine equivalent if there exists an affine regular mapping* $\mathbf{F}_T$ *such that*

$$\begin{cases} T = \mathbf{F}_T(\hat{T}) \\ P_T = \left\{p : T \to \mathbb{R},\ p = \hat{p} \circ \mathbf{F}_T^{-1},\ \hat{p} \in \hat{P}\right\} \\ \Sigma_T = \left\{l, l(p) = \hat{l}(p \circ \mathbf{F}_T), \hat{l} \in \hat{\Sigma}\right\}. \end{cases} \tag{3.14}$$

Theorem 1. *Let* $\hat{p}_1, .., \hat{p}_N$ *be a basis function of the finite element* $\left(\hat{T}, \hat{P}, \hat{\Sigma}\right)$*, then functions* $p_i = \hat{p}_i \circ \mathbf{F}_T^{-1},\ i = 1.., N$ *are the basis functions of the finite element* (T, P_T, Σ_T)*. It addition it holds that* $\hat{P}$*-interpolation operator* $\hat{\Pi}$*, defined in* (3.12) *and the* P_T*-interpolation operator* Π_T *satisfy*

$$\hat{\Pi_T} v = \hat{\Pi}\hat{v}, \quad \forall \hat{v} \in \mathcal{D}(\hat{\Pi}) \text{ and } \forall\, v = \hat{v} \circ \mathbf{F}_T^{-1} \in \mathcal{D}(\Pi_T). \tag{3.15}$$

Definition 5 (General definition of finite element spaces)**.** *Let* Ω_h *be a bounded domain with Lipschitz continuous boundary and* $\mathcal{T}_h$ *triangulation satisfying all assumptions* $(\mathcal{T}_h 1) - (\mathcal{T}_h 4)$*. We define a general finite element space as*

$$X_h := \Big\{v_h \in L^2(\Omega), v_h\Big|_T \in P_T \ \ \forall T \in \mathcal{T}_h, l_{T,i}(v_h|_T) = l_{\hat{T},i}(v_h|_{\hat{T}}) \\ \forall T, \hat{T} \in \mathcal{T}_{h,i}, i = 1, .., N_h\Big\}, \tag{3.16}$$

where indices $i = 1, .., N_h$ *denotes global nodes and* $\mathcal{T}_{h,i}$ *set of elements containing node* i*.*

By summing the basis functions over the elements we can eventually get $\{p_i\}_{i=1}^{N_h}$ the basis of finite element space X_h with $\Sigma_h = \{l_i\}_{i=1}^{N_h}$ a set of global degrees of freedom, where $i = 1, .., N_h$ are indices of the nodes. It holds that $l_i(p_j) = \delta_{ij}$ for $i, j = 1, .., N_h$
Considering the Dirichlet boundary conditions on Γ_{D}^h, we define

$$\Sigma_h^{\Gamma_{\mathrm{D}}} = \left\{l \in \Sigma_h;\ l(v|_{\Omega_h}) = 0\ \forall \varphi \in C^\infty(\mathbb{R}^n); \varphi = 0 \text{ on } \Gamma_{\mathrm{D}}^h\right\} \tag{3.17}$$

and finite-dimensional function space

$$\hat{X}_h = \left\{v_h \in X_h;\ l(v_h) = 0\ \forall l \in \Sigma_h^{\Gamma_{\mathrm{D}}}\right\}. \tag{3.18}$$

Assuming functionals from Σ_h are defined on space $\mathrm{Q}(\Omega_h)$, we can also define a global X_h *interpolation operator* $\Pi_h : Q(\Omega_h) \to X_h$, such that

$$\Pi_h v = \sum_{i=1}^{N_h} l_i(v) p_i \quad \text{ for } v \in Q(\Omega_h). \tag{3.19}$$

Moreover it holds for every $T \in \mathcal{T}_h$ that $(\Pi_h v)\,|_T = \Pi|_T(v|_T)$, where Π_T is defined through (3.15).

Consider a mixed function space $\hat{\mathbf{X}}_h \times Q_h$ of finite-dimensional function spaces $\hat{\mathbf{X}}_h$, Q_h from 3.2 with general definitions (3.16), (3.18). The specific choices of these spaces that we use in our computations are Taylor-Hood finite element and $\mathbf{H}(\mathrm{div}, \Omega)$-conforming finite element, which are in detail described in sections 3.2.2

and 3.2.3 respectively. Our aim is to develop a script for reliable and efficient computation of flow in the aortic root. As the problem is in three-dimensions, the computational time is high mainly due to the direct computations of the linear system (3.11) in Newton iterations. A potential future modification is the implementation of a multigrid scheme for solving this linear system. In [17] they discuss using the multigrid scheme for stationary Naiver-Stokes equations on Scott-Vogelius element. However, there are challenges associated with using Taylor-Hood finite elements together with multigrid methods. In contrast, $\mathbf{H}(\mathrm{div}, \Omega)$-conforming finite elements are more suitable for this method, which is our main motivation to use and investigate the influence of these spaces on numerical computations.

3.2.2 Classical methods - Taylor-Hood discretisation

Consider a mixed function space $\hat{\mathbf{X}}_h \times Q_h$ of finite-dimensional function spaces $\hat{\mathbf{X}}_h$, Q_h from 3.2 with general definitions (3.16), (3.18). Classical methods are those, where we look for continuos approximative velocity $\hat{\mathbf{v}}_h \in \hat{\mathbf{X}}_h$ and pressure $p_h \in Q_h$ which are conforming in (i.e. they are contained in space) $\hat{\mathbf{V}}$ and $L^2(\Omega)$ respectively. It seems as a natural choice for discretisation of the weak formulation in (2), where we look for weak solution $((\mathbf{v} - \mathbf{v}^*_{\mathrm{in}})(t), p(t)) \in \hat{\mathbf{V}} \times L^2(\Omega)$. Frequently used classical mixed discretisation generating these spaces and ensuring the inf-sup Babuška condition [5] is the *Taylor-Hood finite element* $\mathbf{P}_k/\mathrm{P}_{k-1}$ for $k \geq 2$, further denoted as TH_k. Therefore finite-dimensional spaces for the approximative velocity $\hat{\mathbf{v}}_h$ and for approximative pressure p_h satisfy $\hat{\mathbf{X}}_h \subset \hat{\mathbf{V}}$, $Q_h \subset L^2(\Omega)$ respectively and are defined as

$$\mathbf{X}_h = \left\{ \mathbf{v}_h \in \mathbf{C}(\overline{\Omega}_h), \mathbf{v}_h|_T \in \mathbf{P}_k \ \ \forall T \in \mathcal{T}_h \right\}, \tag{3.20}$$

$$\hat{\mathbf{X}}_h := \left\{ \hat{\mathbf{v}}_h \in \mathbf{X}_h; \ l(\hat{\mathbf{v}}_h) = 0 \ \forall l \in \Sigma_h^{\Gamma_{\mathrm{D}}} \right\}, \tag{3.21}$$

$$Q_h := \left\{ p_h \in C(\overline{\Omega}_h), p_h|_T \in P_{k-1} \ \ \forall T \in \mathcal{T}_h \right\}, \tag{3.22}$$

where P_k is polynomial of order k. Thus spaces contain functions, that are continuous and piecewise polynomials of order k. For approximative velocity $\mathbf{v}_h$ it means that every component is in P_k. Set of degrees os freedoms Σ_h are values at points. Set $\Sigma_h^{\Gamma_{\mathrm{D}}}$ is defined as (3.17), where $\Gamma_{\mathrm{D}}^h = \Gamma_{\mathrm{in}}^h$ for problem of flow in the aortic root, when using Nitche's method for imposing impermeability condition (1.7).

Non-divergence-free property.

To the weak formulation in (2) we added the weak form of the incompressibility condition (1.1) for $\mathbf{v} \in \mathbf{V}$, which reads

$$-\int_\Omega q \, \mathrm{div}\, \mathbf{v} \, \mathrm{d}x = 0 \quad \forall q \in L^2(\Omega), \tag{3.23}$$

For the discretised problem we try to satisfy for $\mathbf{v}_h \in \mathbf{X}_h$:

$$-\int_{\Omega_h} q_h \, \mathrm{div}\, \mathbf{v}_h \, \mathrm{d}x = 0 \quad \forall q_h \in Q_h. \tag{3.24}$$

Simultaneously, it is clear that $\mathrm{div}\, \mathbf{X}_h \not\subset Q_h$, since $\mathrm{div}\, \mathbf{X}_h$ contains also discontinuous functions. Therefore we can not generally get from (3.24) $\| \mathrm{div}\, \mathbf{v}_h \|_{L^2} = 0$ or $\mathrm{div}\, \mathbf{v}_h =$

0 pointwise in Ω_h. Moreover, experiments in sections 4.1 show, that the quantity $\|\operatorname{div} \mathbf{v}_h\|_{L^2}$ can be quite large, hence we say that Taylor-Hood finite element is *non-divergence-free method*. This problematic is in detailed discussed for Stokes problem in [24].

Error estimates for Stokes problem.

In [24] the error estimates using classical methods are in detail analysed for the Stokes problem.
Let us have solution $(\mathbf{v},\ p)$ to the *Stokes problem*, that reads

$$\begin{aligned} -\nu\Delta\mathbf{v} + \nabla p &= \mathbf{f} \quad \text{in } \Omega \\ \operatorname{div}\mathbf{v} &= 0 \quad \text{in } \Omega \\ \mathbf{v} &= \mathbf{0} \quad \text{on } \partial\Omega, \end{aligned} \tag{3.25}$$

for $\mathbf{f} \in \mathbf{L}^2(\Omega)$. The approximative solution $(\mathbf{v}_h, p_h) \in \hat{\mathbf{X}}_h \times Q_h \subset \hat{\mathbf{V}} \times L^2_0(\Omega)$ is obtained using Taylor-Hood finite element. Here $\hat{\mathbf{X}}_h$, $\hat{\mathbf{V}}$ are defined in (3.21), (3.1) respectively, for $\Gamma_{\mathrm{D}} = \partial\Omega$ and we denote $L^2_0(\Omega) = \{q \in L^2(\Omega), \int_\Omega q\,\mathrm{d}x = 0\}$ The error estimates for velocity $\mathbf{v}_h$ and pressure p_h can be obtained by the analogue of Céa's lemma, which can be further estimated by error of interpolation operator (3.19), for general theorem of error estimates for interpolation operator, see [12]. Firstly, define

$$\mathbf{X}_{h,div} := \left\{ \mathbf{v}_h \in \hat{\mathbf{X}}_h, \int_{\Omega_h} q_h \operatorname{div}\mathbf{v}_h \,\mathrm{d}x = 0 \ \forall q_h \in Q_h \right\}, \tag{3.26}$$

the space of discretely divergence-free functions.

Theorem 2 (Error estimates for Stokes problem discretised by Taylor-Hood element (Theorem 4.21, 4.25, Corollary 4.30 in [23]))**.** *Let Ω_h be a bounded domain with polyhedral Lipschitz continuous boundary. Consider family of triangulations $\{\mathcal{T}_h\}$ satisfying assumptions $(\mathcal{T}_h 1) - (\mathcal{T}_h 4)$ $\forall T \in \bigcup_h \mathcal{T}_h$ and such that system $\{\mathcal{T}_h\}$ is regular, i.e. there exists constant κ such that $\frac{h_T}{\rho_T} \leq \kappa$ $\forall T \in \bigcup_h \mathcal{T}_h$ and the quantity $h = \max_{T\in\mathcal{T}_h} h_T$ approaches zero. Also all finite elements (T, P_T, Σ_T), $T \in \mathcal{T}_h$ are affine equivalent to a single reference finite element $\left(\hat{T}, \hat{P}, \hat{\Sigma}\right)$. Let $(\mathbf{v},\ p)$ be solution of the Stokes problem (3.25), with $\mathbf{v} \in \mathbf{W}^{k+1,2}(\Omega) \cap \hat{\mathbf{V}}$ and $p \in W^{k,2}(\Omega) \cap L^2_0(\Omega)$. Then for the discretisation of this problem with inf-sup stable conforming Taylor-Hood finite element $\boldsymbol{P}_k/P_{k-1}$ $k \geq 2$ with spaces $\hat{\mathbf{X}}_h \times Q_h$, denoting the velocity solution by $\mathbf{v}_h \in \mathbf{X}_{h,div}$, holds*

$$\begin{aligned} \|\nabla(\mathbf{v} - \mathbf{v}_h)\|_{L^2(\Omega_h)} &\leq 2 \inf_{\tilde{\mathbf{v}}_h \in \mathbf{X}_{h,div}} ||\nabla(\mathbf{v} - \tilde{\mathbf{v}}_h)||_{L^2(\Omega_h)} + \nu^{-1} \inf_{q_h \in Q_h} ||p - q_h||_{L^2(\Omega_h)} \\ &\leq Ch^k \left(\|\mathbf{v}\|_{W^{k+1,2}(\Omega_h)} + \nu^{-1}\|p\|_{W^{k,2}(\Omega_h)} \right) \end{aligned} \tag{3.27}$$

$$\begin{aligned} \|p - p_h\|_{L^2(\Omega_h)} &\leq C_1\nu \inf_{\tilde{\mathbf{v}}_h \in \mathbf{X}_{h,div}} ||\nabla(\mathbf{v} - \tilde{\mathbf{v}}_h)||_{L^2(\Omega_h)} + C_2 \inf_{q_h \in Q_h} ||p - q_h||_{L^2(\Omega_h)} \\ &\leq Ch^k \left(\nu\|\mathbf{v}\|_{W^{k+1,2}(\Omega_h)} + \|p\|_{W^{k,2}(\Omega_h)} \right), \end{aligned} \tag{3.28}$$

with constants C_1, C_2, C independent of h.

Hence the $\mathbf{H}_1$ norm of the velocity depends on the approximation properties of space $\mathbf{X}_{h,div}$ but also due to $\operatorname{div} \mathbf{X}_h \not\subset Q_h$ it eventually depends on the approximation of the pressure or on the smallness of the viscosity. Thus it can happen that the term $\nu^{-1}\|p\|_{W^{k,2}(\Omega_h)}$ dominates in the velocity error bound.
It is important to note that these estimates are established on the domain $\Omega_h \approx \Omega$ with a polyhedral boundary and also under the assumption that all integrals in the weak formulation of the given problem are computed exactly. However, in practice, the integrals are evaluated using numerical integration, and the real domain Ω is often not polyhedral, meaning that its boundary is not composed of a union of simplices (triangles in two dimensions, tetrahedra in three dimensions). These factors are known as *variational crimes*, and they can result in less accurate estimates than those presented. In section 3.4 we consider better approximation Ω_h of Ω, using higher-order piecewise polynomial boundary. With this procedure we aim to reduce the inaccuracies related to the second variational crime.

Grad-div stabilisation

The higher error in $\|\operatorname{div} \mathbf{v}_h\|_{L^2} = 0$ for the classical methods, such as the Taylor-Hood element, can be reduced by adding the *grad-div stabilisation*, which penalises the violation of mass conservation. It was first presented in [18].
The idea is to add term $-\alpha \nabla(\operatorname{div} \mathbf{v}) = \mathbf{0}$ to the linear momentum equation, where $\mathbf{v}$ is the strong solution. Then multiply by $\boldsymbol{\phi} \in \hat{\mathbf{V}}$, defined in (3.1)) and integrate over Ω (as in derivation of the weak formulation). Since $\operatorname{div} \mathbf{v} = 0$ on the boundary, using integration per partes we eventually get the additional term

$$\alpha \int_{\Omega_h} \operatorname{div} \mathbf{v}_h \operatorname{div} \boldsymbol{\phi}_h \,\mathrm{d}x \quad \forall \boldsymbol{\phi} \in \hat{\mathbf{X}}_h \tag{3.29}$$

in the discretised weak formulation. [24] and [23] proves on Stokes problem that for smaller stabilisation parameter α, the divergence error became smaller and vanishes for $\alpha \to \infty$. However in practice, we do not take α too high, to not make other terms less relevant (in finite precision arithmetic).

3.2.3 $\mathbf{H}(\operatorname{div}, \Omega)$-conforming discretisations

Again we assume a mixed function space $\hat{\mathbf{X}}_h \times Q_h$ of finite-dimensional function spaces $\hat{\mathbf{X}}_h$, Q_h, from discretisation 3.2, with general definitions (3.16), (3.18). Now we consider non-conforming discretisation ($\hat{\mathbf{X}}_h \not\subset \hat{\mathbf{V}}$) of space for velocities, but satisfying the divergence-free property $\operatorname{div} \mathbf{X}_h \in Q_h$. The review of diverge-free methods are provided for example in [29]. One of them are the $\mathbf{H}(\operatorname{div}, \Omega)$-conforming methods, which are suitable divergence-free methods for our problem, where we discuss also better approximation of the boundary. We provide a brief introduction how are this spaces defined, more details can be found in [23].
Let us have triangulation $\mathcal{T}_h$ satisfying assumptions $(\mathcal{T}_h 1) - (\mathcal{T}_h 4)$. Let $\mathcal{E}_h$ be set of facets (edges in two dimensions, faces in three dimensions). Denote $\mathcal{E}_h^B \subset \mathcal{E}_h$ the set of boundary facets and $\mathcal{E}_h^I := \mathcal{E}_h \setminus \mathcal{E}_h^B$ set of interior facets. We no longer require $\mathbf{X}_h \subset \mathbf{V}$ as we did in Taylor-Hood conforming finite element method, instead we have $\mathbf{X}_h \subset \mathbf{H}(\operatorname{div}, \Omega)$, which is defined as

$$\mathbf{H}(\operatorname{div}, \Omega) := \left\{ \mathbf{v} \in \mathbf{L}^2(\Omega) : \operatorname{div} \mathbf{v} \in \mathbf{L}^2(\Omega) \right\}, \tag{3.30}$$

also we denote space

$$\mathbf{H}_0(\mathrm{div},\Omega) := \{\mathbf{v} \in \mathbf{H}(\mathrm{div},\Omega); \mathbf{v}\cdot\mathbf{n} = \mathbf{0} \text{ on } \Gamma_D\}, \tag{3.31}$$

here for problem of flow in the aortic root (1.1)-(1.8) we have $\Gamma_D = \Gamma_{\text{in}} \cap \Gamma_{\text{wall}}$.

Lemma 3. *Let $\mathbf{X}_h$ denote a space of piecewise polynomials with respect to partition $\mathcal{T}_h$. Then $\mathbf{X}_h \subset \mathbf{H}(\mathrm{div},\Omega)$, provided the normal components (not necessarily the tangential components) of functions in this space are continuous across all inter-element boundaries $e \in \mathcal{E}_h^I$.*

Article [33] address all the issues for assembly of the $\mathbf{H}(\mathrm{div},\Omega)$-conforming finite elements for numerical implementation. We present two spaces satisfying the lemma (3).

Raviart-Thomas finite element space.

Raviart-Thomas (RT) finite element spaces are class of vector-valued finite element spaces defined as

$$\mathrm{RT}_k := \{\hat{\mathbf{v}}_h \in \mathbf{H}_0(\mathrm{div},\Omega) : \hat{\mathbf{v}}_h|_T \in \mathbf{P}_k(T) + \mathbf{x}P_k(T)\ \forall T \in \mathcal{T}_h\} \quad k \geq 0, \tag{3.32}$$

where $\mathbf{H}_0(\mathrm{div},\Omega)$ is defined in (3.31). Defining space DP_k, such that

$$\mathrm{DP}_k := \left\{p_h \in L^2(\Omega), p_h|_T \in P_k \quad \forall T \in \mathcal{T}_h\right\}, \tag{3.33}$$

yields to inf-sup stable mixed finite element pair $\hat{\mathbf{X}}_h \times Q_h = \mathrm{RT}_k \times \mathrm{DP}_k$ for approximative velocity and pressure which we will denote *Raviart-Thomas finite element*. Note that the mathematical definition (3.32) for lowest order $k = 0$ leads to space $\mathrm{RT}_0 := \{\hat{\mathbf{v}}_h \in \mathbf{H}_0(\mathrm{div},\Omega) : \hat{\mathbf{v}}_h|_T \in \mathbf{P}_0(T) + \mathbf{x}P_0(T)\ \forall T \in \mathcal{T}_h\}$, i.e. it is a linear function on each element. However in Firedrake library, which we use for implementation of finite element method, such space is denoted as RT_1, since it contains piecewise linear functions. Similarly for each k in definition (3.32), the space is numerically implemented as RT_{k+1} with DP_k.

Brezzi-Douglas-Marini finite element space.

Brezzi-Douglas-Marini (BDM) finite element spaces are also class of vector-valued finite element spaces defined as

$$\mathrm{BDM}_k := \{\hat{\mathbf{v}}_h \in \mathbf{H}_0(\mathrm{div}) : \hat{\mathbf{v}}_h|_T \in \mathbf{P}_k(T)\, \forall T \in \mathcal{T}_h\} \quad k \geq 1. \tag{3.34}$$

Choosing space DP_{k-1}, defined in (3.33), for approximative pressure, yields to an inf-sup stable mixed finite element pair $\hat{\mathbf{X}}_h \times Q_h = \mathrm{BDM}_k \times \mathrm{DP}_{k-1}$ for approximative velocity and pressure which we will denote *Brezzi-Douglas-Marini finite element*.

Degrees of freedoms

For presented $\mathbf{H}(\mathrm{div},\Omega)$ methods, the degrees of freedom (DOFs) on facets contain normal integral moments with Lagrange space of order k (assuming here k from the mathematical definition (3.32)). On the interior of the reference element are integral

moments with vector Lagrange space of order $k-1$. [3] Therefore when imposing Dirichlet boundary conditions, $\mathbf{H}(\mathrm{div}, \Omega)$ elements take into account only the normal component on the boundary, the tangential part must be imposed weakly to the weak formulation. For illustration we show some formulas of degrees of freedom for RT and BDM on triangle, analogous formulas can be obtained for tetrahedron.

Example: DOFs for RT_0 on triangle Degrees of freedom for RT_0 on the reference triangle are defined as

$$l : \mathbf{v} \to \int_{e_i} \mathbf{v} \cdot \mathbf{n}_i, \; i = 0, 1, 2,$$

where e_i are edges of the triangle and $\mathbf{n}_i$ their normals. The corresponding basis functions are shown on Figure 3.1

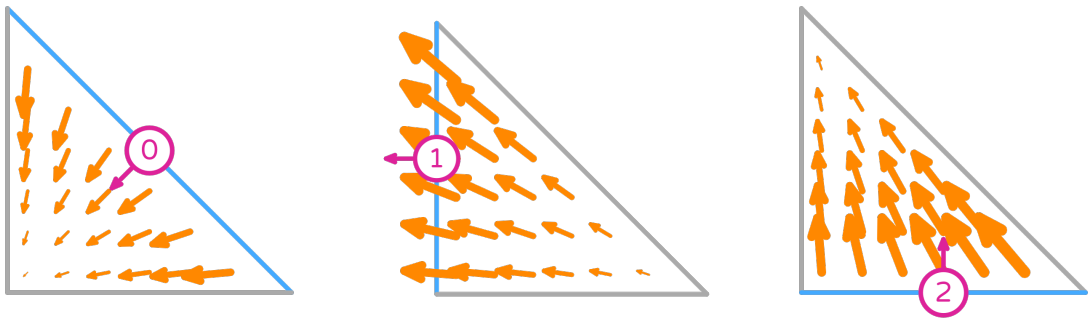

Figure 3.1: Basis functions for RT_0 on triangle (source: DefElement)

Example: DOFs for RT_1 on triangle Degrees of freedom for RT_1 on the reference triangle are defined as

$$\begin{aligned}
l : \mathbf{v} &\to \int_{e_i} \mathbf{v} \cdot (1 - s_0)\mathbf{n}_i, \; i = 0, 1, 2 \\
l : \mathbf{v} &\to \int_{e_i} \mathbf{v} \cdot (s_0)\mathbf{n}_i, \; i = 0, 1, 2 \\
l : \mathbf{v} &\to \int_R \mathbf{v} \cdot \begin{pmatrix} 1 \\ 0 \end{pmatrix} \\
l : \mathbf{v} &\to \int_R \mathbf{v} \cdot \begin{pmatrix} 0 \\ 1 \end{pmatrix}
\end{aligned}$$

where e_i are edges of the triangle, $\mathbf{n}_i$ their normals and s_0 their parametrisation (which represents the Lagrange space of order k on the edges). On Figure 3.2 are shown the basis functions for interior degrees of freedoms (with numbering 6,7), basis functions for degrees of freedom on edges are show just for one edge e_0 (with numbering 0,1), others would look analogously.

[3] Lagrange space denotes space consisting of piecewise polynomial functions that are continuous across the elements of the mesh. For example in Taylor-Hood finite element the velocity is in vector Lagrange space of order k and pressure in Lagrange space of order $k-1$.

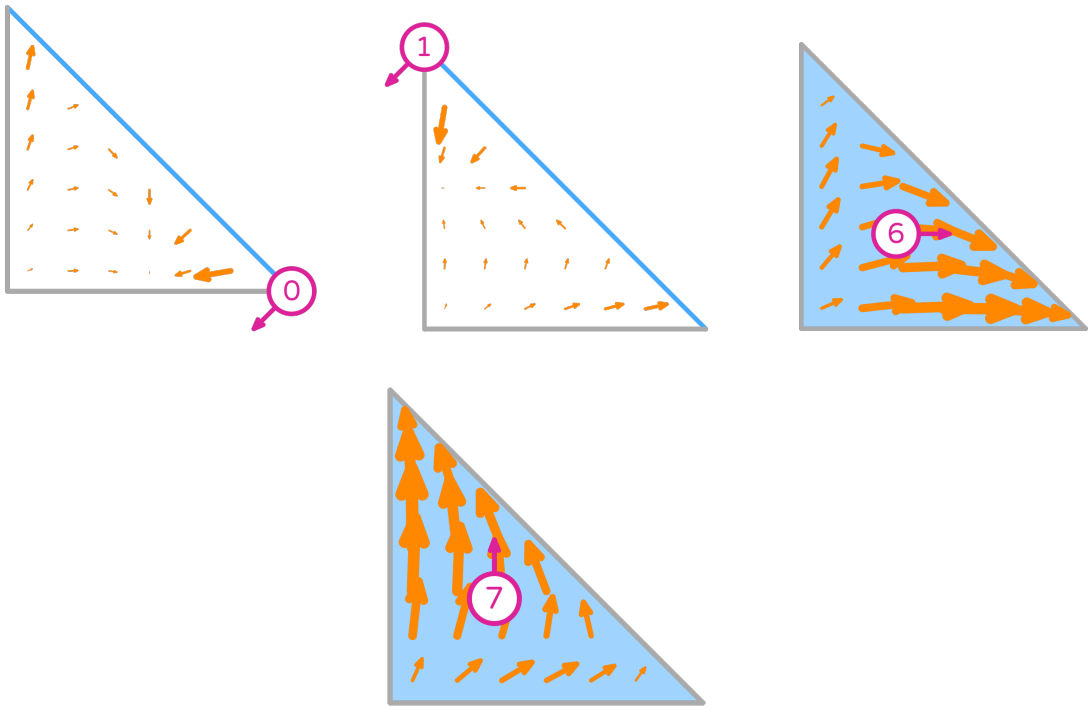

Figure 3.2: Basis functions for RT_1 on triangle (source: DefElement)

Example: DOFs for BDM_1 on triangle Degrees of freedom for BDM_1 on the reference triangle are defined as

$$l : \mathbf{v} \to \int_{e_i} \mathbf{v} \cdot (1 - s_0)\mathbf{n}_i,\ i = 0, 1, 2$$
$$l : \mathbf{v} \to \int_{e_i} \mathbf{v} \cdot (s_0)\mathbf{n}_i,\ i = 0, 1, 2$$

where e_i are edges of the triangle, $\mathbf{n}_i$ their normals and s_0 their parametrisation. Note that this six degrees of freedom are the same as those six on edges for RT_1.

Divergence-free property.

From the construction, both these finite elements satisfy $\operatorname{div} \mathbf{X}_h \subseteq Q_h$, therefore for $\mathbf{v}_h \in \mathbf{X}_h$

$$-(\operatorname{div} \mathbf{v}_h, q_h) = 0 \quad \forall q_h \in Q_h \tag{3.35}$$

implies $\operatorname{div} \mathbf{v}_h = 0$ pointwise in Ω.

Modification of the weak formulation.

In section 1.2 we showed how to get to the weak formulation for test functions $\boldsymbol{\varphi} \in \hat{\mathbf{V}}$, defined in (3.1), for $\Gamma_\mathrm{D} = \Gamma_\mathrm{in} \cap \Gamma_\mathrm{wall}$. For numerical computation we assumed the space without constraining zero divergence in it. Now we aim to get to the weak formulation for $\mathbf{v}$ and p but assuming the test functions from space $\hat{\mathbf{X}}_h \subset \mathbf{H}_0(\operatorname{div}, \Omega)$ (but $\hat{\mathbf{X}}_h \not\subset \hat{\mathbf{V}}$) being the Raviart-Thomas or Brezzi-Douglas-Marini space. The procedure to get to the weak formulation is similar as for derivation the Discontinuous Galerkin method, where we assume discontinuity for both normal and

tangential components across facets. Here we derive similar formulas, but knowing that normal components are automatically continuous by definition of the space $\mathbf{H}(\mathrm{div}, \Omega)$, hence we can force the continuity only to tangential components. Little bit different procedure is provided in [24] for Stokes problem in two dimensions.
Also due to the degrees of freedom for RT and BDM finite elements, which are applied only to the normal component on facets, we do not have to use the Nitsche's method as in section 3.1, to impose the impermeability condition $\mathbf{v} \cdot \mathbf{n}|_{\Gamma_{\mathrm{wall}}} = 0$ weakly. However, since $\hat{\mathbf{X}}_h \not\subset \hat{\mathbf{V}}$ the gradients of functions $\mathbf{w}_h \in \hat{\mathbf{X}}_h$ do not exist globally. Thus multiplying the right hand side of (1.2) by $\mathbf{w}_h \in \hat{\mathbf{X}}_h \subset \mathbf{H}_0(\mathrm{div}, \Omega)$, integrating over Ω_h and then using integration by parts element-wise, we get

$$\int_{\Omega_h} \mathrm{div}\, \mathbb{T}\, \mathrm{d}x = -\sum_{T \in \mathcal{T}_h} \int_T \mathbb{T} : \nabla\, \mathbf{w}_h\, \mathrm{d}x + \sum_{T \in \mathcal{T}_h} \int_{\partial T} \mathbb{T}\mathbf{n} \cdot \mathbf{w}_h\, \mathrm{d}x.$$

The first term can be written as $\int_\Omega \mathbb{T} : \nabla_h\, \mathbf{w}_h\, \mathrm{d}x$ denoting ∇_h as piecewise gradient operator. The additional second term can be separated as

$$\begin{aligned} &\sum_{T \in \mathcal{T}_h} \int_{\partial T} \mathbb{T}\mathbf{n} \cdot \mathbf{w}_h\, \mathrm{d}s = \sum_{e \in \mathcal{E}_h^I} \int_e [\mathbb{T}_+\mathbf{n}_+ \cdot (\mathbf{w}_h)_+ + \mathbb{T}_-\mathbf{n}_- \cdot (\mathbf{w}_h)_-]\ \mathrm{d}s \\ &+ \sum_{e \in \mathcal{E}_h^B} \int_e \mathbb{T}\mathbf{n} \cdot (\mathbf{w}_h)\, \mathrm{d}s = \mathcal{I}_I + \mathcal{I}_B \end{aligned} \tag{3.36}$$

where $\boldsymbol{\phi}_+ := \boldsymbol{\phi}|_{T+}$, $\boldsymbol{\phi}_- := \boldsymbol{\phi}|_{T-}$. Let us now focus on the first term, which we denote as $\mathcal{I}_I$. Since $\mathbb{T} = -p\mathbb{I} + 2\mu_*\mathbb{D}(\mathbf{v})$ and the normal components of $\mathbf{w}_h$ are continuous across all inner facets, we can write

$$\mathcal{I}_I = \sum_{e \in \mathcal{E}_h^I} \int_e [2\mu_*\mathbb{D}_+\mathbf{n}_+ \cdot (\mathbf{w}_h)_+ + 2\mu_*\mathbb{D}_-\mathbf{n}_- \cdot (\mathbf{w}_h)_-]\ \mathrm{d}s.$$

We use the notation $\mathbb{A}\mathbf{b} \cdot \mathbf{c} = \mathbb{A} : (\mathbf{c} \otimes \mathbf{b})$ for matrix $\mathbb{A}$ and vectors $\mathbf{b}$, $\mathbf{c}$. Further we use that for normals to facets on each T holds $\mathbf{n}_- = -\mathbf{n}_+$. Hence we get

$$\mathcal{I}_I = \mu_* \sum_{e \in \mathcal{E}_h^I} \int_e [2\mathbb{D}_+ : ((\mathbf{w}_h)_+ \otimes \mathbf{n}_+) - 2\mathbb{D}_- : ((\mathbf{w}_h)_- \otimes \mathbf{n}_+)]\ \mathrm{d}s.$$

Now we use the identity $\mathbb{A} : \mathbb{B} - \mathbb{C} : \mathbb{D} = \frac{1}{2}(\mathbb{A} - \mathbb{C}) : (\mathbb{B} + \mathbb{D}) + \frac{1}{2}(\mathbb{A} + \mathbb{C}) : (\mathbb{B} - \mathbb{D})$ and a little manipulation to get

$$\begin{aligned} \mathcal{I}_I = \mu_* \sum_{e \in \mathcal{E}_h^I} \int_e \Big[&\frac{1}{2}(2\mathbb{D}_+ - 2\mathbb{D}_-) : \{((\mathbf{w}_h)_+ \otimes \mathbf{n}_+) + ((\mathbf{w}_h)_- \otimes \mathbf{n}_+)\} \\ &\frac{1}{2}(2\mathbb{D}_+ + 2\mathbb{D}_-) : \{((\mathbf{w}_h)_+ \otimes \mathbf{n}_+) + ((\mathbf{w}_h)_- \otimes \mathbf{n}_-)\} \Big]\ \mathrm{d}s. \end{aligned}$$

The first term can be again rewritten as $(2\mathbb{D}_+ - 2\mathbb{D}_-)\mathbf{n}_+ \cdot ((\mathbf{w}_h)_+ + (\mathbf{w}_h)_-)$, where $(\mathbb{D}_+ - \mathbb{D}_-)\mathbf{n}_+$ denotes jump of $\mathbb{D}$ across the inner facets, which vanishes assuming $\mathbf{v}$ sufficiently smooth. Denoting the average as

$$\mathrm{avg} = \frac{1}{2}(\mathbb{A}_+ + \mathbb{A}_-), \tag{3.37}$$

we can finally write

$$\mathcal{I}_I = \mu_* \sum_{e \in \mathcal{E}_h^I} \int_e \operatorname{avg}(2\mathbb{D}) : 2 \operatorname{avg}(\mathbf{w}_h \otimes \mathbf{n}) \, \mathrm{d}s.$$

To keep the symmetry, but also still the stability, we add the so called *symmetry term* and *penalisation term*, respectively:

$$\begin{aligned} \mathcal{I}_I = \mu_* \sum_{e \in \mathcal{E}_h^I} \Big[& \int_e \operatorname{avg}(2\mathbb{D}(\mathbf{v})) : 2 \operatorname{avg}(\mathbf{w}_h \otimes \mathbf{n}) \, \mathrm{d}s \\ & + \int_e \operatorname{avg}(2\mathbb{D}(\mathbf{w}_h)) : 2 \operatorname{avg}(\mathbf{v} \otimes \mathbf{n}) \, \mathrm{d}s - \frac{\sigma}{h_e} \int_e 2 \operatorname{avg}(\mathbf{v} \otimes \mathbf{n}) : 2 \operatorname{avg}(\mathbf{w}_h \otimes \mathbf{n}) \, \mathrm{d}s \Big] \end{aligned} \tag{3.38}$$

where $h_e = \operatorname{diam}(e)$, $\sigma >$ is the penalisation parameter, which is problem dependent and must be chosen experimentally.
Let us now continue with term denoted as $\mathcal{I}_B$ in (3.36). Since $\mathbf{w}_h \in \mathbf{H}_0(\operatorname{div}, \Omega)$, on Γ^h_{wall} remains just tangential components [4]. Therefore we get

$$\mathcal{I}_B = \int_{\Gamma^h_{\text{in}}} \mathbb{T}\mathbf{n} \cdot \mathbf{w}_h \, \mathrm{d}S + \int_{\Gamma^h_{\text{wall}}} (\mathbb{T}\mathbf{n})_\tau \cdot (\mathbf{w}_h)_\tau \, \mathrm{d}S + \int_{\Gamma^h_{\text{out}}} \mathbb{T}\mathbf{n} \cdot \mathbf{w}_h \, \mathrm{d}S \tag{3.39}$$

On Γ^h_{out} and Γ^h_{wall} we simply use the conditions (1.6), (1.8) respectively. In the first term of (3.39) we can omit the pressure part of Cauchy stress tensor (1.3) since $\mathbf{w}_h \in \mathbf{H}_0(\operatorname{div}, \Omega)$. The remaining part can be written, using the notation $\mathbb{A}\mathbf{b} \cdot \mathbf{c} = \mathbb{A} : (\mathbf{c} \otimes \mathbf{b})$ as

$$\int_{\Gamma^h_{\text{in}}} \mathbb{T}\mathbf{n} \cdot \mathbf{w}_h \, \mathrm{d}S = \int_{\Gamma^h_{\text{in}}} 2\mu_* \mathbb{D}(\mathbf{v}) : (\mathbf{w}_h \otimes \mathbf{n}) \, \mathrm{d}S. \tag{3.40}$$

Adding to(3.40) also the symmetric and penalisation term similarly as in (3.38) also with imposing the condition on Γ_{in} leads to

$$\begin{aligned} \int_{\Gamma^h_{\text{in}}} \mathbb{T}\mathbf{n} \cdot \mathbf{w}_h \, \mathrm{d}S = & \int_{\Gamma^h_{\text{in}}} 2\mu_* \mathbb{D}(\mathbf{v}) : (\mathbf{w}_h \otimes \mathbf{n}) \, \mathrm{d}S \\ & + \int_{\Gamma^h_{\text{in}}} 2\mu_* \mathbb{D}(\mathbf{w}_h) : ((\mathbf{v} - \mathbf{v}^*_{\text{in}}) \otimes \mathbf{n}) \, \mathrm{d}S - \frac{\mu_* \sigma}{h_e} \int_{\Gamma^h_{\text{in}}} (\mathbf{v} - \mathbf{v}^*_{\text{in}}) \cdot \mathbf{w}_h \, \mathrm{d}S. \end{aligned} \tag{3.41}$$

Weak formulation. Giving all the terms together, with the use of (3.38), (3.41) we get the weak formulation for test functions $\mathbf{w}_h \in \mathbf{H}_0(\operatorname{div}, \Omega)$ and we can define the weak solution.

Definition 6 (Weak solution)**.** *Find* $(\mathbf{v} - \mathbf{v}^*_{\text{in}}, p) \in L^\infty(0, T; \mathbf{L}^2(\Omega)) \cap L^2(0, T; \hat{\mathbf{V}}) \times$

[4] In fact also on Γ^h_{in} should remain just the tangential part $\int_{\Gamma^h_{\text{in}}} (\mathbb{T}\mathbf{n})_\tau \cdot (\mathbf{w}_h)_\tau \, \mathrm{d}S$, however our experiments show that leaving here also the normal part, which is from the Dirichlet condition set as zero, we get same or better results.

$L^{5/4}(0,T;L^2(\Omega))$ *such that*

$$\begin{aligned}
&\rho_*\left\langle\frac{\partial\mathbf{v}}{\partial t},\mathbf{w}_h\right\rangle+\rho_*\int_\Omega(\nabla\mathbf{v})\mathbf{v}\cdot\mathbf{w}_h\,\mathrm{d}x-\int_\Omega p\,\mathrm{div}\,\mathbf{w}_h\,\mathrm{d}x+2\mu_*\int_\Omega\mathbb{D}(\mathbf{v}):\mathbb{D}(\mathbf{w}_h)\,\mathrm{d}x\\
&-\int_\Omega q\,\mathrm{div}\,\mathbf{v}\,\mathrm{d}x-\mu_*\sum_{e\in\mathcal{E}_h^I}\Big[\int_e\mathrm{avg}(2\mathbb{D}(\mathbf{v})):2\,\mathrm{avg}(\mathbf{w}_h\otimes\mathbf{n})\,\mathrm{d}s\\
&-\int_e\mathrm{avg}(2\mathbb{D}(\mathbf{w}_h)):2\,\mathrm{avg}(\mathbf{v}\otimes\mathbf{n})\,\mathrm{d}s-\frac{\sigma}{h_e}\int_e 2\,\mathrm{avg}(\mathbf{v}\otimes\mathbf{n}):2\,\mathrm{avg}(\mathbf{w}_h\otimes\mathbf{n})\,\mathrm{d}s\Big]\\
&-\int_{\Gamma_{\mathrm{in}}}2\mu_*\mathbb{D}(\mathbf{v}):(\mathbf{w}_h\otimes\mathbf{n})\,\mathrm{d}S+\int_{\Gamma_{\mathrm{in}}}2\mu_*\mathbb{D}(\mathbf{w}_h):((\mathbf{v}-\mathbf{v}_{\mathrm{in}}^*)\otimes\mathbf{n})\,\mathrm{d}S\\
&-\frac{\mu_*\sigma}{h_e}\int_{\Gamma_{\mathrm{in}}}(\mathbf{v}-\mathbf{v}_{\mathrm{in}}^*)\cdot\mathbf{w}_h\,\mathrm{d}S+\frac{\theta}{\gamma_*(1-\theta)}\int_{\Gamma_{\mathrm{wall}}}\mathbf{v}_\tau\cdot(\mathbf{w}_h)_\tau\,\mathrm{d}S\\
&=-P(t)\int_{\Gamma_{\mathrm{out}}}\mathbf{w}_h\cdot\mathbf{n}\,\mathrm{d}S+\frac{\rho_*}{2}\int_{\Gamma_{\mathrm{out}}}(\mathbf{v}\cdot\mathbf{n})_-\mathbf{v}\cdot\mathbf{w}_h\,\mathrm{d}S,
\end{aligned}$$

valid for all $(\mathbf{w}_h,q)\in\mathbf{H}_0(\mathrm{div},\Omega)\times L^2(\Omega)$ *and a.a.* $t\in(0,T)$.

For such weak formulation it makes sense to apply the $\mathbf{H}(\mathrm{div},\Omega)$-conforming discretisation (after discretizing the domain to Ω_h).
Note that adding the symmetry and penalisation terms in (3.38), (3.41) can be taken as applying the Nitsche's method, introduced in 3.1, to impose weakly the continuity in tangential direction between inner facets in case of (3.38), or imposing weakly the Dirichlet condition on Γ_{in} in case of (3.41) (here we could impose it only in the tangential direction since for the normal component the Dirichlet condition is imposed strongly).

Stabilisations. For $\mathbf{H}(\mathrm{div},\Omega)$-conforming elements we will use the *upwind stabilisation*. It is common procedure for the discontinuous Galerkin discretisation and comes from applying the integration per partes on the convective term $\rho_*\int_\Omega(\nabla\mathbf{v})\mathbf{v}\cdot\mathbf{w}_h\,\mathrm{d}x$. Moreover even for $\mathbf{H}(\mathrm{div},\Omega)$-conforming elements we also add the grad-div stabilisation. The additional term (3.29) is zero from the divergence-free property (3.35), however it should improve the numerical properties.

Error estimates for Stokes problem.

Consider the Stokes problem defined in (3.25) with the modified weak formulation, which can be obtain in a same manner as above for the problem of flow in aortic root. Firstly, define discrete $\mathbf{H}^1$-norm as

$$\|\mathbf{w}\|_{1,h}^2:=\sum_{T\in\mathcal{T}_h}\|\nabla\mathbf{w}\|_{L^2(T)}^2+\sum_{e\in\mathcal{E}_h}h_e\|\,\mathrm{avg}(2\mathbb{D}(\mathbf{w}))\|_{L^2(e)}^2+\sum_{e\in\mathcal{E}_h}h_e^{-1}\|\,\mathrm{avg}(\mathbf{w}\otimes\mathbf{n})\|_{L^2(e)}^2. \tag{3.42}$$

The error estimates for the Stokes problem is analysed for example in [24], leading to following results,

$$\|\mathbf{v}-\mathbf{v}_h\|_{1,h}\le C\inf_{\tilde{\mathbf{v}}_h\in\hat{\mathbf{X}}_h}\|\mathbf{v}-\tilde{\mathbf{v}}_h\|_{1,h}\le Ch^{l-1}\|\mathbf{v}\|_{W^{l,2}(\Omega_h)}, \tag{3.43}$$

$$\begin{aligned}
\|p-p_h\|_{L^2(\Omega_h)}&\le C\left(\nu\|\mathbf{v}-\tilde{\mathbf{v}}_h\|_{1,h}+\inf_{q_h\in Q_h}\|p-q_h\|_{L^2(\Omega_h)}\right)\\
&\le C\left(\nu h^{l-1}\|\mathbf{v}\|_{W^{l,2}(\Omega_h)}+h^m\|p\|_{W^{m,2}(\Omega_h)}\right).
\end{aligned} \tag{3.44}$$

Assume for the solution of the Stokes problem (3.25) $(\mathbf{v},\ p) \in (\mathbf{W}^{s,2}(\Omega),\ W^{r,2}(\Omega))$. Then, $l = \min\{s, k+1\}$. If $\hat{\mathbf{X}}_h \times Q_h$ is Raviart-Thomas finite element pair $\mathrm{RT}_k \times \mathrm{DP}_k$, then $m = \min\{r, k+1\}$. If $\hat{\mathbf{X}}_h \times Q_h$ is Brezzi-Douglas-Marini finite element pair $\mathrm{BDM}_k \times \mathrm{DP}_{k-1}$, then $m = \min\{r, k\}$. That is, in language of numerical implementation, velocity in RT_{k+1} (RT_k by mathematical definition (3.32)) and BDM_k has the same error convergence rate. Therefore the same also holds for the pressure error.

3.3 Shape of the computational domain

Aortic root, the subject of our interest, is a region located behind the aortic valve. It is characterised by its structure containing three sinuses, see Figure 3.3. It starts from the aortic valve and ends behind the three sinuses. It is known, that such

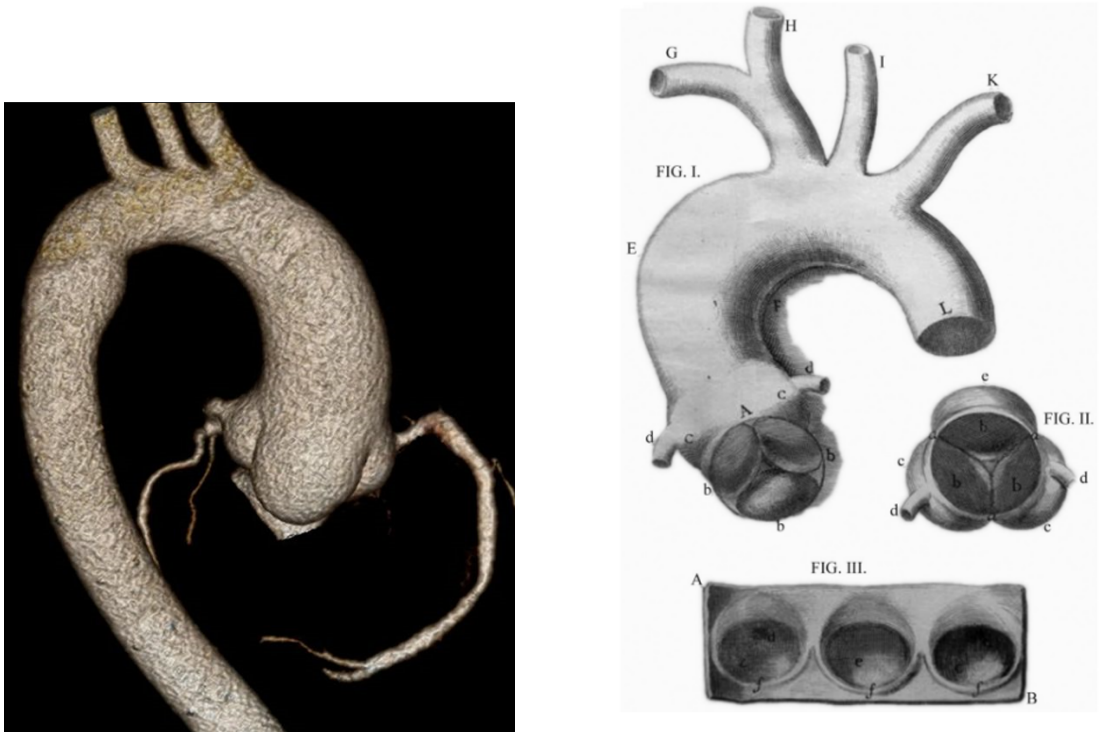

Figure 3.3: On left: CT image of aorta (source). On right: illustration of the aortic root with three sinuses (source: Biography of Antonio Maria Valsalva, Morgagni G. 1740).

shape induce vortices in this region, which affect the underlying valve. The flow dynamics in the aortic root is highly complex, involving many factors to be considered. Therefore it is reasonable to start with the most simplified model and subsequently introduce modifications to analyse their impact on the character of the flow.
Regarding the geometry, the most simplified model can be considered as a straight, rigid tube without the valve. For such model, the characteristics of the flow, including dissipation, vorticity, pressure drop under varying Navier's slip parameters θ from (1.8) are analysed in [9]. By modifying the geometry to a tube with an axially symmetric sinus extension, [10] found out, depending on the radius of the extension and the Navier slip parameter θ, there are conditions under which vortices begin to

form and conditions where the flow becomes chaotic.
We will proceed using different (analytical) description of the geometry, which can be either with axially symmetric extension or extension with three sinuses, representing the ones in the real aortic root in Figure 3.3. Still, we do not consider aortic valve and the coronary arteries, coming from the aortic root to our model as we want to fully understand the behaviour and role of the sinuses on its own. However there are studies as [20], [37], where the effect of fully tree dimensional model of the aortic root with mechanical aortic valve is investigated. Study [16] demonstrated that the fluid structure interaction contained in a model does not have a significant effect on character of the flow. Therefore, we also assume the walls to be rigid for now.

Description of the geometry

It is also possible to create a mesh of the aortic root from MRI images, however for our purposes of analysing the flow in domain with axial or non-axial sinus extension, we want to have the analytical description. It is also essential in our process of generating piecewise polynomial boundaries, presented in section 3.4.
For description of the geometry in cross-section, we follow the article [32]. The shape of the aortic root can be here approximated by epitrochoid. It is curve described by a point which lies inside an exterior circle of radius r rolling on a fixed interior circle of radius R and the point is at a distance d from the centre of the exterior circle, see Figure 3.4. In Cartesian parametrisation:

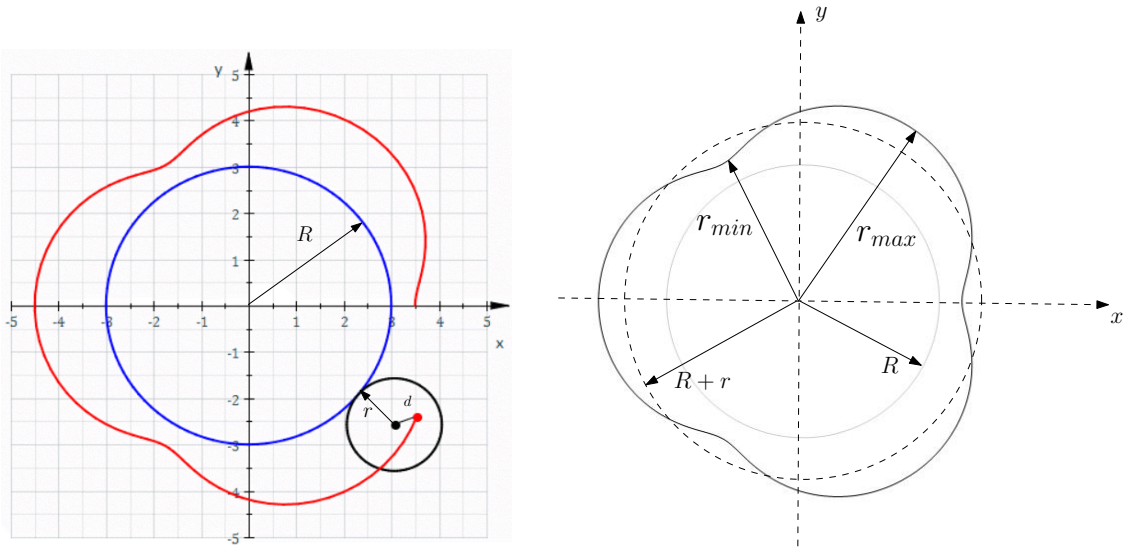

Figure 3.4: Epitrochoid for $R = 3r$, $d = 0.5$ (source: Wikipedia)

$$x = (R+r)\cos(s) - \lambda r \cos\left(\frac{R+r}{r}s\right) \tag{3.45}$$

$$y = (R+r)\sin(s) - \lambda r \sin\left(\frac{R+r}{r}s\right), \tag{3.46}$$

where $\lambda = d/r$. The angle s is geometrically the polar angle of the centre of the exterior circle, however it is not a polar angle of the point $(x(s), y(s))$ on the epitrochoid. The outer circle rotates three times around the inner one, representing three

sinus of the same size, hence $R = 3r$. According to [32], $\lambda = 0.5$ corresponds to normal aortic root. Values r_{min} and r_{max}, see Figure 3.4, can be then computed, denoting $R + r = r_{char}$, as

$$r_{min} = R + r - \lambda r = r_{char} - \lambda r,$$
$$r_{max} = R + r + \lambda r = r_{char} + \lambda r.$$

Study [39] refers that the upper limit of radius in normal aortic root is $r_{max} = 20$ mm for men and $r_{max} = 18$ mm for woman. In term of characteristic radius r_{char}, we further in numerical computations set $r_{char} = 16$ mm (for $\lambda = 0.5$ corresponds to $r_{max} = 18$ mm)
In z direction, we will consider, inspired by [32] and
[10], that region consist of three parts. The first, almost straight one, starting from radius 12 mm, is approximately 10 mm long, representing the left ventricular outflow. Then it extends to the second part, representing sinuses, approximately 24 mm long, with characteristic radius $r_{char} = 16$ mm. Further it narrows to the approximately 10 mm long part, ending with radius 13 mm.
The analytical description which would extend the results (3.45), (3.46) to z direction (main direction of the blood flow) is not reasonably described in literature. Therefore, we suggest to suitably multiply formulas (3.45), (3.46) by exponential functions, to get the following parametrisation.

Parametrisation of the domain. Description of three dimensional shape of the aortic root, parametrized by (s, t) reads

$$\begin{aligned} x &= \frac{D}{2}\cos(s) + \left(r_{char} - \frac{D}{2}\right) e^{-\varphi t^2 - \psi t^4}\cos(s) - \lambda r e^{-\xi t^2}\cos\left(\frac{r_{char}}{r}s\right) \\ y &= \frac{D}{2}\sin(s) + \left(r_{char} - \frac{D}{2}\right) e^{-\varphi t^2 - \psi t^4}\sin(s) - \lambda r e^{-\xi t^2}\sin\left(\frac{r_{char}}{r}s\right) \\ z &= t, \end{aligned} \tag{3.47}$$

for $s \in (0, 2\pi]$, $t \in (-44 \text{ mm }, 44 \text{ mm })$, $r_{char} = R + r$ and

$$\frac{D}{2} = \begin{cases} R_{out} = 13 \text{ mm} & \text{if } t \geq 0 \\ R_{in} = 12 \text{ mm} & \text{if } t < 0 \end{cases}$$

$$\varphi = \begin{cases} \varphi_{out} & \text{if } t \geq 0 \\ \varphi_{in} & \text{if } t < 0 \end{cases}$$

$$\psi = \begin{cases} \psi_{out} & \text{if } t \geq 0 \\ \psi_{in} & \text{if } t < 0 \end{cases}$$

Values for ξ, φ and ψ are chosen using non-linear least squares to fit the shape with the geometry used in [10]. Also, note that the shape, analytically described by (3.47), is infinitely continuous.
Figure 3.5 shows the final shape with dimensions. For comparison of the effect on the dynamic of the flow, governed by equations (1.1)-(1.8), on the shape of the domain, we use two geometries, axially symmetric one and one with three sinuses.

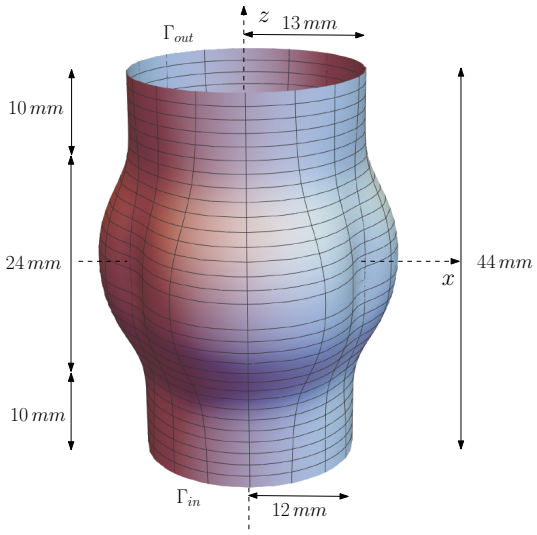

Figure 3.5: Dimensions of the computational domain.

Shape with three sinuses. As we already mentioned the shape with three sinuses can be obtained by choice $\lambda = 0.5$ in the parametrisation (3.47). Hence for the characterisation radius $r_{char} = 16$ mm, the maximal radius is $r_{max} = 18$ mm and minimal radius $r_{min} = 14$ mm. The shape with respect to r_{char} in a cross-section can be seen on right in Figure 3.4.

Axially symmetric shape. Setting $\lambda = 0$ in (3.47), we can get axially symmetric shape with maximal radius $r_{max} = r_{char} = 16$ mm.
Figure 3.6 show the final reference meshes, which are used for all computations. They are generated by software Gmsh [19] and are made of simplices.

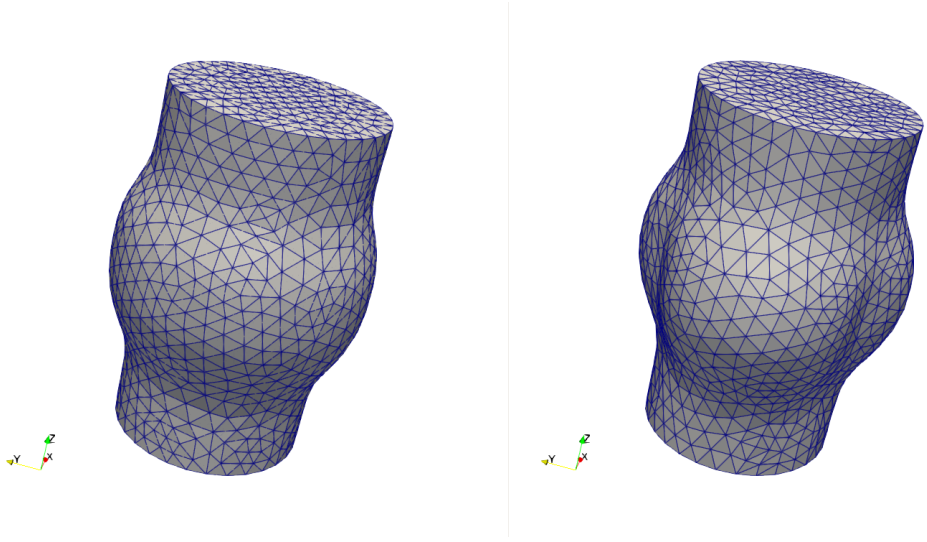

Figure 3.6: Computational meshes with $r_{char} = 16$ mm: axially symmetric one on left, with three sinuses on right.

3.4 Approximation of the boundary

To numerically compute the solution using finite element method, the computational domain Ω must be discretized first. This discretization usually leads to a mesh composed of elements (in our case triangles in 2D or tetrahedra in 3D), each with piecewise linear facets. Together, however, the elements only provide an approximation Ω_h of the real domain Ω, whose boundary may not be very accurate for some general domains with curved boundaries. This problem is one of the so-called variational crimes that occur along with numerical integration in obtaining an approximate solution by the finite element method. As the result the Dirichlet boundary condition is imposed on a slightly shifted boundary and Navier's slip boundary condition (1.8) allows the slip of the fluid on piecewise linear non-smooth boundary. To reduce the resulting inaccuracies, we construct a mesh with a boundary of piecewise higher order polynomials. Section 4.1 of the next chapter demonstrate the difference in convergence of the errors on two simple examples: Couette flow and Poiseuille flow.

Generation of a mesh with boundary of piecewise higher order polynomials. We consider shift $\mathbf{u}$ on the computational discretised domain Ω_h such that

$$\Delta \mathbf{u} = \mathbf{0} \qquad \text{in } \Omega_h \tag{3.48}$$

$$\mathbf{u} = \mathbf{0} \qquad \text{on } \Gamma^h_{\text{out}},\ \Gamma^h_{\text{in}} \tag{3.49}$$

$$\mathbf{u} = \mathbf{x}_{analytical} - \mathbf{x}_{mesh} \qquad \text{on } \Gamma^h_{\text{wall}}, \tag{3.50}$$

where Γ^h_{in}, Γ^h_{out}, Γ^h_{wall} are parts of the boundary of Ω_h. The coordinates $\mathbf{x}_{analytical} \in \mathbb{R}^n$ are prescribed analytically by the given parametric description of the domain ((3.47) in case of our simplified aortic root) and $\mathbf{x}_{mesh} \in \mathbb{R}^n$ are the real coordinates of the given computational mesh. That means we prescribe known shift on the boundary Γ^h_{wall} and smoothly extend it to the whole domain Ω_h. Problem (3.48)-(3.49) is also solved by finite element method using Lagrange space of order l, implying resulted shift $\mathbf{u}$ continuous and piecewise polynomial of the order l. The coordinates of new mesh with boundary of piecewise polynomials of order l, denoted $mesh_l$, is then generated as

$$\mathbf{x}_{mesh_l} = \mathbf{x}_{mesh_1} + \mathbf{u}, \tag{3.51}$$

where $mesh_1$ is the same or very similar mesh as the original reference one. [5] Generated mesh with boundary of piecewise higher polynomials $mesh_l$ is than classically used for further numerical computation of the flow. Note that for general curved domain Ω we can never obtain mesh with precise boundary, only with boundary of piecewise polynomials.

In case of computational domain represented by cylinder (used in Poiseuille flow in section 4.1.2), the corrections on the wall from reference piecewise linear mesh with coordinates x_{mesh_1} to piecewise higher order polynomial mesh, made by parametrisation of the cylinder, leaves the vertices of all elements at the same place and moves points in interior of facets. These corrections are small, therefore the shift can be also generated only requiring (3.50) on Γ^h_{wall} and extending by zero inside of

[5] In case of parametrisation (3.47), linear shift $\mathbf{u}$ on Γ_{wall} only slightly moves the vertices on the surface along the surface.

Ω_h. However the reference mesh x_{mesh_1} for the aortic root is parametrised by (3.47), whose angle s is geometrically the polar angle of the centre of the exterior circle, but is not a polar angle of the point $(x(s), y(s))$ on the epitrochoid, describing the cross section of the domain. Therefore the correction to piecewise higher order polynomial mesh, using again parametrisation (3.47), also slightly shifts the vertices. Hence the shift must be computed as (3.48)-(3.49) to get computational mesh with reasonable shape of elements.
Note that some software, such as Gmsh or Netgen, allows to create a mesh with a boundary of piecewise higher order polynomial, however the current software tools based on Firedrake can not use such meshes directly. Nevertheless, all of these options should give the same output, only the method we have presented using shift $\mathbf{u}$ is slightly more complicated for the user.
Also note that the problem has same degrees of freedom using $mesh_1$ as $mesh_2$, but the computational time is slightly higher for computations on $mesh_2$ due to the more difficult enumeration of the integrals.

Isoparametric finite element method

The idea to use same finite elements for mapping the boundary as for approximating the velocity leads to so called *isoparametric finite element method*. A introduction on this topic can be found in [38].
Denote, similarly as in section 3.2.1 the reference finite element $(\hat{T},\hat{P},\hat{\Sigma})$. Now

- $\hat{T}$ is an bounded closed subset of $\mathbb{R}^n$ with non-empty connected interior and Lipschitz continuous boundary
- $\hat{P}$ is a finite dimensional function space on element $\hat{T}$
- $\hat{\Sigma} = \{\hat{p}(a_i), i = 1, .., N\}$, for N number of nodes, is the set of functionals on $\hat{P}$ giving the evaluation of $\hat{p} \in \hat{P}$ in point a_i (finite element with such degrees of freedom are called *Lagrange finite elements*)

Further, instead of affine regular mapping $\mathbf{F}_T$ defined as (3.13), there is a mapping $\mathbf{G} : \hat{\mathbf{x}} \in \hat{T} \to \mathbf{x} \in T,$ s.t. $\mathbf{x} = (G_j(\hat{\mathbf{x}}))_{j=1,..,n} \in \mathbb{R}^n$ where

$$G_j \in \hat{P} \quad \forall j = 1, .., n, \tag{3.52}$$

with n denoting dimension of the problem. In other words, arbitrary point $\hat{\mathbf{x}}$ in reference element $\hat{T}$ is mapped to the point $\mathbf{x}$ in element T, whose components are each obtained by a polynomial function which is a linear combination of the basis functions on the reference element $\hat{T}$, see Figure 3.7.
An *isoparametric finite element* (T, P, Σ) is then defined by

$$\begin{cases} T = \mathbf{G}(\hat{T}) \\ P = \left\{ p : T \to \mathbb{R},\ p = \hat{p} \circ \mathbf{G}^{-1},\ \hat{p} \in \hat{P} \right\} \\ \Sigma = \{ p(\mathbf{G}(\hat{a}_i)),\ i = 1, .., N \}. \end{cases} \tag{3.53}$$

Note that from this definition, the mapping (3.52) is from the same finite element space on the element. We use isoparametric triangles or tetrahedra elements, see Figure 3.7, but in literature isoparametric quadrilaterals are also often. The same

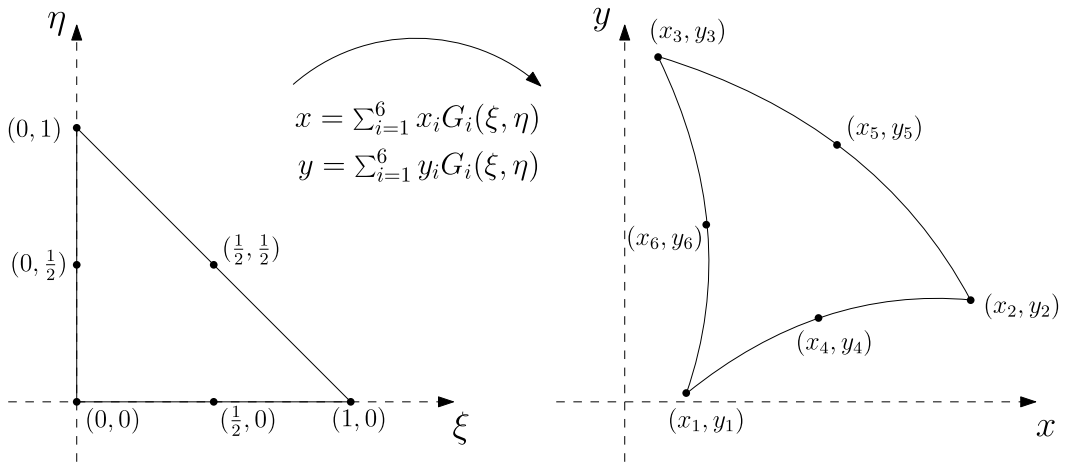

Figure 3.7: Example of quadratic mapping on a reference triangle element. The reference element is described by the coordinates (ξ, η) and $G_i(\xi, \eta)$ are the (quadratic) basis functions here.

convergence result for interpolation operator as for classical finite elements can be also obtained, see [11]. The main obstacle stands in Jacobian of the mapping $\mathbf{G}$ which is no longer constant. Eventually, we can get the estimates for the Stokes problem for classical methods as in theorem (2).
Hence in our case numerically solving problem by finite element method using Lagrange type function spaces (for example space for velocities in Taylor- Hood element) with $P \in P_k$ on a mesh, created by shift (3.48)-(3.50) i.e. with boundary of piecewise polynomials of degree k can be called by isoparametric finite element method. Using $\mathbf{H}(\mathrm{div}, \Omega)$-conforming finite elements with mapping of the boundary from Lagrange space is not isoparemetric finite element method since the assumptions on degrees of freedom from (3.53) is not satisfied and the theory behind is more difficult.

4. Results

The final chapter presents the results from numerical simulations, which are generated using all mentioned methods and aspects presented in Chapter 2.
The main goal of this thesis is to analyse the effect on character of the flow in the aortic root when using following modifications. First, as discussed in section 3.3, we employ the computational mesh with three sinus together with the less realistic axially symmetric mesh. Second, we construct better approximation of the boundary than just piecewise linear, which is addressed in 3.4. Additionally we examine the impact on the solution of the flow using these discretisations in space: Taylor-Hood element and $\mathbf{H}(\mathrm{div}, \Omega)$-conforming elements, see 3.2.2, 3.2.3 respectively. The character of the flow is described by the following characteristic flow quantities.

Flow quantities. Flow quantities we are interested in are bulk dissipation Ξ_Ω, boundary dissipation Ξ_Γ, kinetic energy E_k, average wall shear stress $\frac{1}{|\Gamma_{wall}|}\|(\mathbb{T}\mathbf{n})_\tau\|_{1,\Gamma}$, pressure drop p_{drop}, vorticity $\frac{1}{|O|}\|\operatorname{rot}\mathbf{v}\|_{1,O}$, wall flux, respectively:

$$\Xi_\Omega := 2\mu \int_\Omega |\mathbb{D}(\mathbf{v})|^2 \,\mathrm{d}x \tag{4.1}$$

$$\Xi_\Gamma := \begin{cases} \frac{\theta}{1-\theta} \int_{\Gamma_{\mathrm{wall}}} |\mathbf{v}_\tau|^2 \,\mathrm{d}S & \text{if } \theta < 1 \\ 0 & \text{if } \theta = 1 \end{cases} \tag{4.2}$$

$$E_k := \int_\Omega \rho \frac{|\mathbf{v}|^2}{2} \,\mathrm{d}x \tag{4.3}$$

$$\frac{1}{|\Gamma_{wall}|}\|(\mathbb{T}\mathbf{n})_\tau\|_{1,\Gamma} := \frac{1}{|\Gamma_{wall}|} \int_{\Gamma_{\mathrm{wall}}} |(\mathbb{T}\mathbf{n})_\tau| \,\mathrm{d}S \tag{4.4}$$

$$p_{drop} := \frac{1}{|\Gamma_{in}|} \int_{\Gamma_{\mathrm{in}}} p \,\mathrm{d}S - \frac{1}{|\Gamma_{out}|} \int_{\Gamma_{\mathrm{out}}} p \,\mathrm{d}S \tag{4.5}$$

$$\frac{1}{|\Omega|}\|\operatorname{rot}\mathbf{v}\|_{1,\Omega} := \frac{1}{|\Omega|} \int_\Omega |\operatorname{curl}(\mathbf{v})| \,\mathrm{d}x \tag{4.6}$$

$$\mathrm{flux}_{wall} := \int_{\Gamma_{\mathrm{wall}}} \mathbf{v} \cdot \mathbf{n} \,\mathrm{d}S. \tag{4.7}$$

4.1 Piecewise linear versus piecewise higher order polynomial boundary

Since we do not have the exact analytical solution for (1.1)-(1.8), we can not say, if the solution using mentioned modifications are more accurate. Therefore, we set two benchmark problems: Couette flow in two dimensions and Poiseuille flow in three dimensions, where we know the analytical solution. On these examples we demonstrate the accuracy of the solution and of the characteristic quantities when computing on a mesh with piecewise higher order polynomial boundary rather then piecewise linear. Simultaneously, it will be computed by Taylor-Hood element and $\mathbf{H}(\mathrm{div}, \Omega)$-nonconforming Raviart-Thomas and Brezzi-Douglas-Marini elements. [10] demonstrated the importance of the allowed slip on the boundary, therefore we investigate the solutions also under different slip parameters θ coming from Navier's slip boundary condition.

We are interested in relative velocity L^2 error, relative velocity H^1 error, relative pressure L^2 error of each solution, respectively:

$$e_{v,L^2} = \frac{\|\mathbf{v} - \mathbf{v}_{ex}\|_2}{\|\mathbf{v}_{ex}\|_2} \tag{4.8}$$

$$e_{v,H^1} = \frac{\|\nabla(\mathbf{v} - \mathbf{v}_{ex})\|_2}{\|\nabla\mathbf{v}_{ex}\|_2} \tag{4.9}$$

$$e_{p,L^2} = \frac{\|p - p_{ex}\|_2}{\|p_{ex}\|_2}, \tag{4.10}$$

where $\mathbf{v}_{ex}$ and p_{ex} are known exact analytical solutions of the problem and $\mathbf{v}$, p here denotes the approximative solutions from the numerical computations. To see the convergence depending on the degrees of freedoms (DOFs), we compute the errors of solution for set of refined meshes. An estimated order of convergence (EOC) is taken as

$$\text{EOC} = \frac{\log(\frac{e(h_{N-1})}{e(h_N)})}{\log(\frac{h_{N-1}}{h_N})} \tag{4.11}$$

for each error $e = e_{v,L^2}$, e_{v,H^1}, e_{p,L^2}. Here h_N is the minimal cell diameter in the most refined mesh, h_{N-1} the minimal cell diameter in the second most refined mesh. Values of EOC can be than compared to the theoretical results for Stokes problem (2) when using Taylor-Hood element or (3.43) and (3.44) when using $\mathbf{H}(\text{div}, \Omega)$-conforming elements.
Also the L^2 norm of the divergence $\|\operatorname{div}\mathbf{v}\|_2$ is plotted in graphs for illustration of fulfilling the incompressibility condition by divergence-free $\mathbf{H}(\text{div}, \Omega)$-conforming methods as opposed to non-divergence-free classical methods such as Taylor-Hood. For Poiseuille flow the flow quantities (4) are numerically computed and the error with respect to degrees of freedom is investigated.
Convergence of the errors is plotted with respect to $\text{DOFs}^{\frac{1}{d}}$, where d denotes dimension of the problem and DOFs denotes degrees of freedom of the whole mixed space. For a fair comparison of used finite elements, this is a better option than plotting with respect to the minimum element size.

4.1.1 Couette flow in two dimensions between two concentric circles

Couette flow in two dimensions between two concentric circles is simple example with known analytical solution and curved boundary. Since it is in two dimensions, the computational costs are low and we can afford to compute solutions on more refinements of the computational mesh.

Definition of the problem

We assume incompressible Navier-Stokes fluid. The inner circle is at rest and outer circle rotates with angular velocity Ω_{out} and same Navier's slip boundary conditions are imposed on both walls Γ_{in} and Γ_{out}. Assume the problem is stationary and $\mathbf{v} = (0, v_\varphi(r))$, $p = p(r)$ (see geometry of the problem in Figure 4.1). Governing

equations and boundary conditions can be therefore written as

$$\rho(\mathbf{v}\cdot\nabla\mathbf{v}) = \operatorname{div}\mathbb{T} \quad \text{in } \Omega, \tag{4.12}$$
$$\nabla\cdot\mathbf{v} = 0 \quad \text{in } \Omega, \tag{4.13}$$
$$\mathbb{T} = -p\mathbb{I} + \mu\left(\nabla\mathbf{v} + \nabla\mathbf{v}^T\right) \quad \text{in } \Omega, \tag{4.14}$$

$$\mathbf{v}\cdot\mathbf{n} = 0 \quad \text{on } \Gamma_{\text{in}}, \tag{4.15}$$
$$\theta\mathbf{v}_\tau + \gamma(1-\theta)(\mathbb{T}\mathbf{n})_\tau = 0 \quad \text{on } \Gamma_{\text{in}}, \tag{4.16}$$
$$\mathbf{v}\cdot\mathbf{n} = 0 \quad \text{on } \Gamma_{\text{out}}, \tag{4.17}$$
$$\theta(\mathbf{v}_\tau - V) + \gamma(1-\theta)(\mathbb{T}\mathbf{n})_\tau = 0 \quad \text{on } \Gamma_{\text{out}}, \tag{4.18}$$
$$\tag{4.19}$$

where velocity on the outer circle is $V = \Omega_{out}R_{out}$.

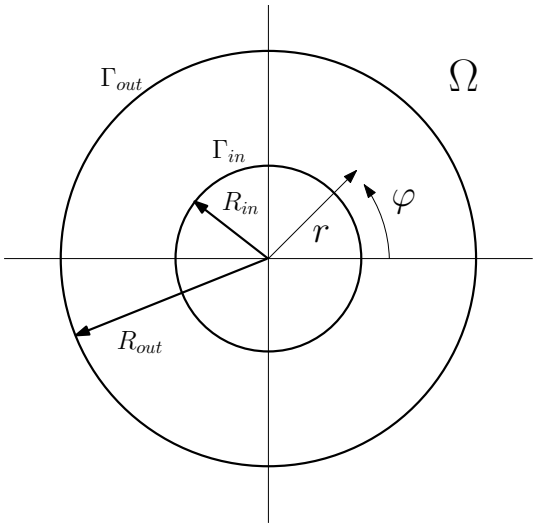

Figure 4.1: Geometry for Couette flow in concetric circles in two dimensions.

Exact solution

Analytical form of velocity and pressure are computed for example in [22] (there for flow between concentric cylinders in three dimensions) and are as follows

$$(v_\varphi)_{ex} = Ar + \frac{B}{r}$$
$$p_{ex} = \rho\left(\frac{A^2}{2}r^2 - \frac{B^2}{2r^2} + AB\ln r + K\right),$$

where K is such that $p(R_{in}) = 0$. Velocity in Cartesian coordinates (x, y) can be then written as

$$\mathbf{v}_{ex} = \left(-\frac{y}{\sqrt{x^2+y^2}}(v_\varphi)_{ex}, \frac{x}{\sqrt{x^2+y^2}}(v_\varphi)_{ex}\right).$$

Constants A and B are

$$A = \frac{R_{in}R_{out}\Omega_{out}R_{out}^2 + 2\mu\kappa R_{out}^3\Omega_{out}}{R_{in}R_{out}(R_{out}^2 - R_{in}^2) + 2\mu\kappa(R_{out}^3 + R_{in}^3)}$$
$$B = -\frac{R_{in}^3 R_{out}^3\Omega_{out}}{R_{in}R_{out}(R_{out}^2 - R_{in}^2) + 2\mu\kappa(R_{out}^3 + R_{in}^3)},$$

with $\kappa = \gamma\frac{1-\theta}{\theta}$.

Experiments

Numerical tests are computed for values of constant parameters given in Table 4.1. The solution is quite sensitive to the stabilisation parameter β coming from

Table 4.1: Chosen values of parameters for Couette flow between concentric circles.

Symbol	Name	Value	Unit
ρ	density	1	$\mathrm{kg.m^{-3}}$
μ	dynamic viscosity	0.001	$\mathrm{kg.m^{-1}.s^{-1}}$
Ω_{out}	angular velocity on R_{out}	1	$\mathrm{rad.s^{-1}}$
R_{in}	inner radius	1	m
R_{out}	outer radius	2	m
γ	slip parameter	3.08	$\mathrm{m^2.s.kg^{-2}}$

Nitsche's method (3.3) and stabilisation parameter σ from weak formulation (6) for $\mathbf{H}(\mathrm{div}, \Omega)$-conforming methods. The optimal value is experimentally set as $\beta = 10$ and $\sigma = 100$. The grad-div stabilisation (3.29) with parameter α around 1 for all used finite elements is used. $\mathbf{H}(\mathrm{div}, \Omega)$-conforming elements are computed with upwind stabilisation.

Results for $\theta = 1$. Figure 4.2 shows the solution errors for Couette flow with no-slip ($\theta = 1$) on the wall [1]. It is computed with piecewise linear ($l = 1$) and quadratic ($l = 2$) boundary, using finite elements with $k = 2$, that means TH_2 ($\mathbf{P}_2$ for velocity, P_1 for pressure), RT_3 (RT_3 for velocity, DP_2 for pressure), BDM_2 (BDM_2 for velocity, DP_1 for pressure). It demonstrates the improvement of accuracy and higher EOC (mainly in velocity errors) when using piecewise quadratic boundary for all finite elements. Also, for $l = 1$ RT and BDM, elements needs more DOFs to get to the same error as TH element. For $l = 2$ the results are very similar, even better for RT and BDM elements.

Results for $\theta = 0.5$. Figure 4.3 captures the same setting, only with imposed partial slip $\theta = 0.5$ on Γ_{wall}. For TH element the convergence of velocity in H^1 is significantly worse for $l = 1$, however it seems that the pressure error surprisingly

[1] In the weak formulations (2) or (6), the term on Γ_{wall} imposing the Navier's slip boundary condition is not defined for $\theta = 1$. Therefore, we compute this case with imposing the Dirichlet boundary condition $\mathbf{v}|_{\Gamma_{\mathrm{wall}}} = 0$ strongly for the Taylor-Hood element. On contrary, for $\mathbf{H}(\mathrm{div}, \Omega)$-conforming elements we additionally need to impose $\mathbf{v}\cdot\boldsymbol{\tau}|_{\Gamma_{\mathrm{wall}}} = 0$ weakly into the weak formulation. The results are also very similar as to compute Navier's slip with $\theta = 0.999$.

doesn't very depend on smoothness of the boundary. For RT and BDM elements the difference in velocity and pressure errors between solutions obtained with $l = 1$ and $l = 2$ are significant. Also while for $l = 2$ it is comparable with TH element, using $l = 1$ is much worse than TH. Comparing results for no-slip (Figure 4.2) and for partial slip (Figure 4.3) we can see (except convergence of the pressure for TH) that imposing Navier's slip on non-smooth piecewise linear boundary rather then on smoother piecewise quadratic boundary yields to worse errors convergence then in imposing Dirichlet no-slip boundary condition on the wall.
Using the same finite elements for obtaining the approximative velocity as for mapping the domain leads to *isoparametric finite elements*, described in section 3.4. Therefore in Figure 4.4 we demonstrated for slip parameter $\theta = 0.5$ the difference in using order $k = l = 2$ and $k = l = 3$. There is an improvement for solutions using cubic isoparametric finite elements [2], however, the difference is not so significant as opposed to piecewise linear boundary versus piecewise quadratic boundary with $k = 2$. Also the degrees of freedom are increasing with k, which increases the computational time and memory mainly for problems in three dimensions. Therefore for our purposes we further use $k = 2$ and both $l = 1$ and $l = 2$ to see the difference in smoothness of the boundary.
All the figures 4.2-4.4 demonstrates on last graph, that $\mathbf{H}(\mathrm{div}, \Omega)$-conforming RT and BMD elements satisfy the incompressibility condition $\mathrm{div}\, \mathbf{v} = 0$ (here $\mathbf{v}$ denotes the approximative solution) as opposed to TH finite element.

[2]Strictly from the definition (3.53), we can speak about isoparametric finite elements only when using TH element.

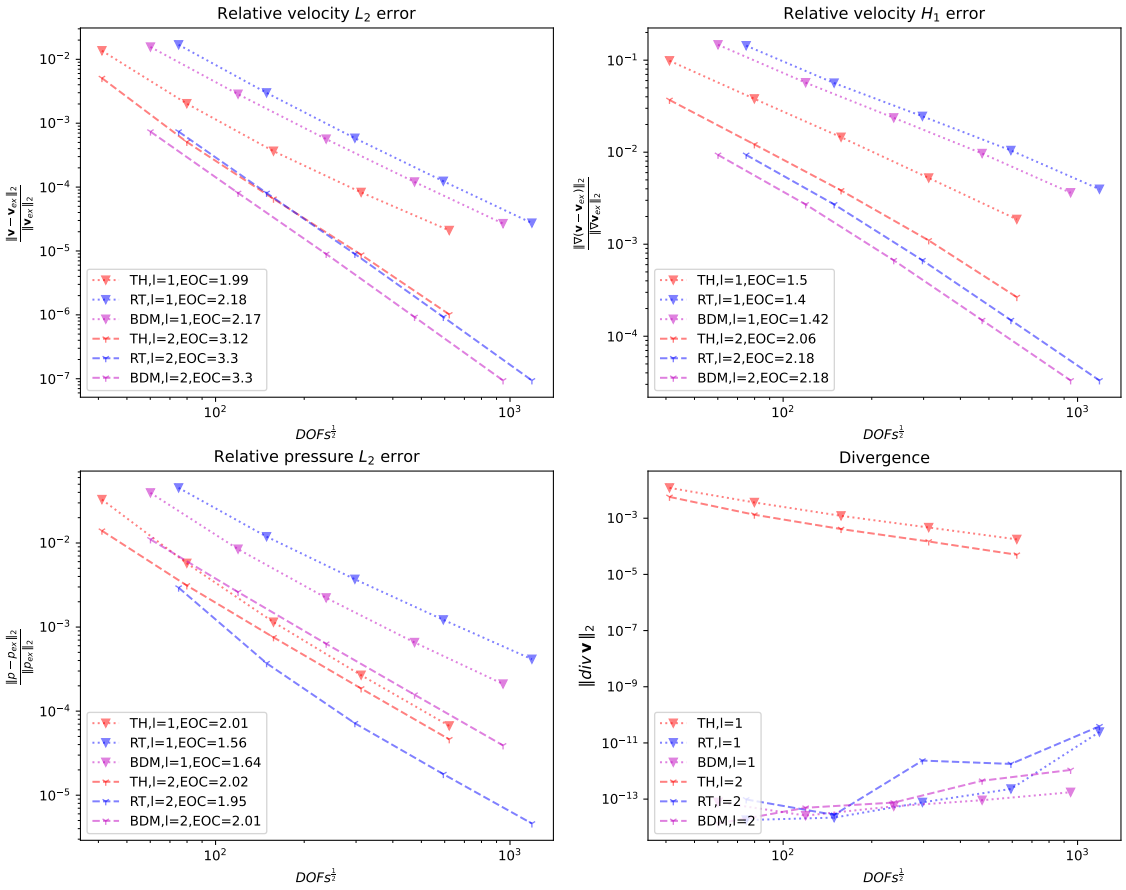

Figure 4.2: Convergence of relative errors, EOC and norm of the velocity divergence for Couette flow with no-slip ($\theta = 1$) on the boundaries, for piecewise linear $l = 1$ (lines with triangles) and piecewise quadratic $l = 2$ (lines with stars) boundary and for TH_2, RT_3, BDM_2 finite elements.

4.1.2 Poiseuille flow in 3D

Poiseuille flow in straight tube in three dimensions is another simple example with know analytical solution and curved boundary. It can be represented as a model of flow in arteries or even very simplified model of flow in the aortic root. With such motivation in mind, the article [9] investigated this problem, analysed the influence of slip parameter θ on Γ_{wall} on flow characteristics defined in (4).

Definition of the problem

We assume again steady flow of incompressible Navier-Stokes fluid in cylinder with Navier's slip boundary condition on Γ_{wall}. Assume the problem is stationary and $\mathbf{v} = (0, 0, v_z(r))$, $p = p(r)$ [3](see geometry of the problem in Figure 4.5). Governing

[3]In numerical computations we keep the convective term, even though in analytical solution it should vanish due to the symmetry.

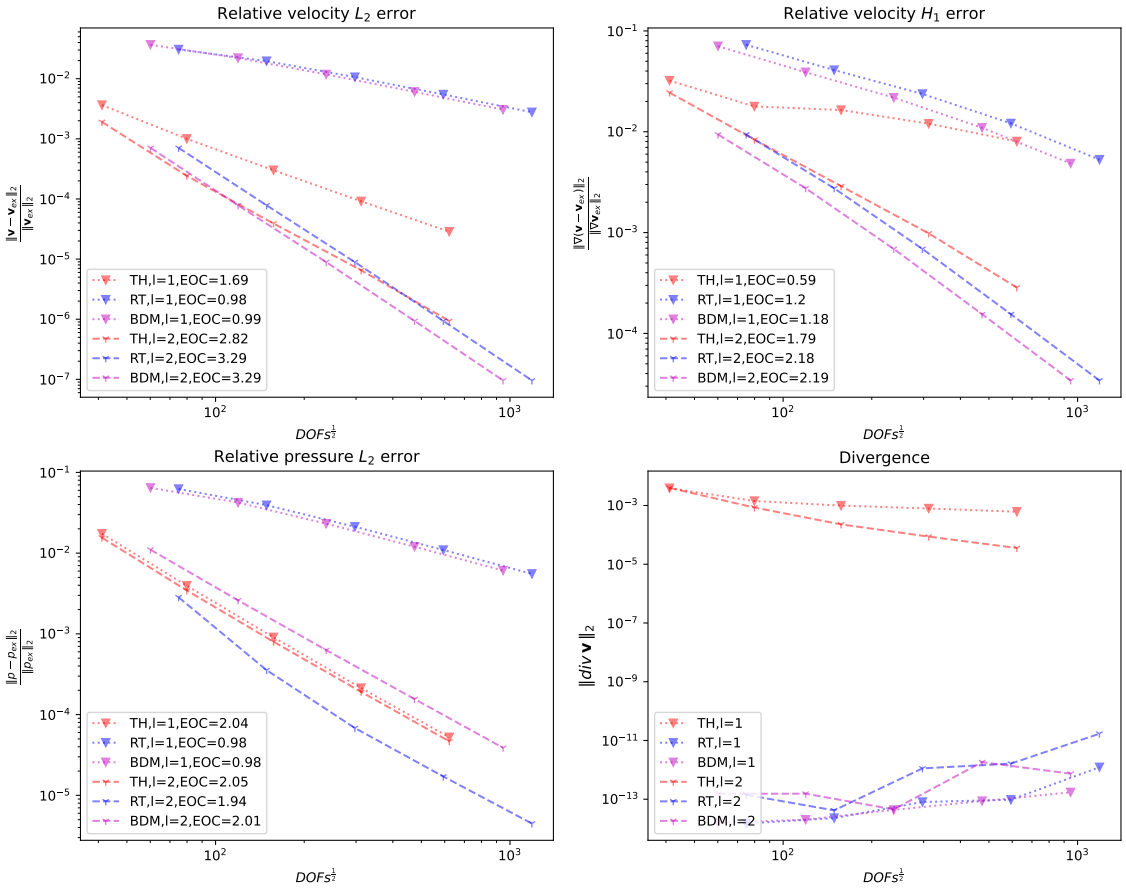

Figure 4.3: Convergence of relative errors, EOC and norm of the velocity divergence for Couette flow with partial slip ($\theta = 0.5$) on the boundaries, for piecewise linear $l = 1$ (lines with triangles) and piecewise quadratic $l = 2$ (lines with stars) boundary and for TH_2, RT_3, BDM_2 finite elements.

equations and boundary conditions read

$$\rho(\mathbf{v} \cdot \nabla \mathbf{v}) = \operatorname{div} \mathbb{T} \qquad \text{in } \Omega, \tag{4.20}$$

$$\nabla \cdot \mathbf{v} = 0 \qquad \text{in } \Omega, \tag{4.21}$$

$$\mathbb{T} = -p\mathbb{I} + \mu \left(\nabla \mathbf{v} + \nabla \mathbf{v}^T \right) \qquad \text{in } \Omega, \tag{4.22}$$

$$\mathbf{v} \cdot \mathbf{n} = 0 \qquad \text{on } \Gamma_{\text{wall}}, \tag{4.23}$$

$$\theta \mathbf{v}_\tau + \gamma(1-\theta)(\mathbb{T}\mathbf{n})_\tau = 0 \qquad \text{on } \Gamma_{\text{wall}}, \tag{4.24}$$

$$\mathbf{v} = \mathbf{v}_{in} \qquad \text{on } \Gamma_{\text{in}}, \tag{4.25}$$

$$\mathbb{T}\mathbf{n} = 0 \qquad \text{on } \Gamma_{\text{out}}, \tag{4.26}$$

$$v_y = v_z = 0 \qquad \text{on } \Gamma_{\text{out}}, \tag{4.27}$$

where the inflow $\mathbf{v}_{in}$ is set as the velocity profile obtained by the exact analytical solution (4.29) defined below. Condition (4.26) states that there is no force at the outlet boundary, which than fixes the pressure as $p\big|_{x=\frac{L}{2}} = 0$. Conditions (4.27) ensures that the flow at the outlet remains parallel.

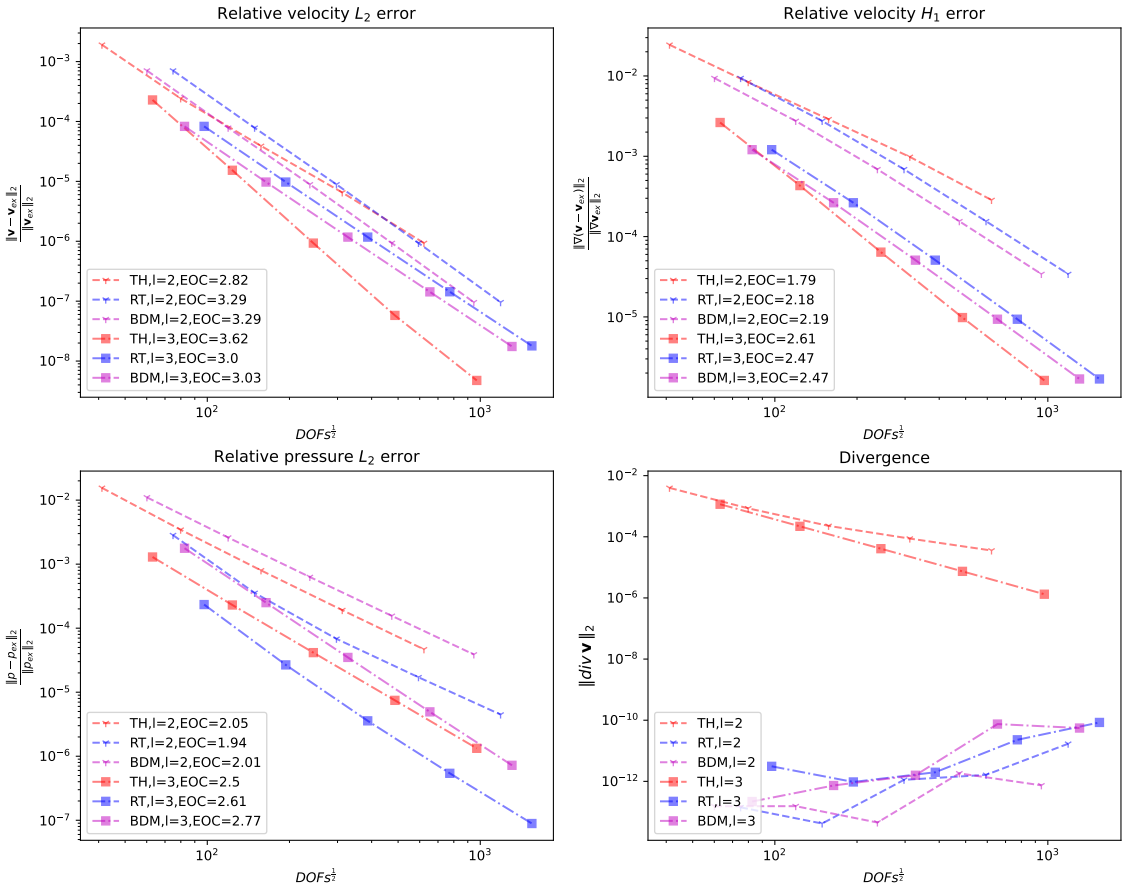

Figure 4.4: Convergence of relative errors, EOC and norm of the velocity divergence for Couette flow with partial slip ($\theta = 0.5$) on the boundaries, for piecewise quadratic $l = 2$ (lines with triangles) and piecewise cubic $l = 3$ (lines with cubes) boundary and for TH_2, RT_3, BDM_2 finite elements.

Exact solution

Derivation of the analytical solution for Poiseuille flow is provided for example in [9] and is as follows

$$(v_z(r))_{ex} = V\frac{4\mu\gamma R(1-\theta) + 2\theta(R^2 - r^2)}{R\left[4\gamma\mu(1-\theta) + \theta R\right]} \tag{4.28}$$

$$\mathbf{v}_{ex} = (0, 0, (v_z(r))_{ex}) \tag{4.29}$$

$$(p(z))_e x = \frac{8\mu V\theta}{R\left[4\gamma\mu(1-\theta) + \theta R\right]}\left(\frac{L}{2} - z\right) \tag{4.30}$$

where V is mean inflow velocity and p is fixed as $p|_{\Gamma_{\text{out}}} = 0$ assuming finite tube.

Experiments

Numerical test are for values of constant parameters given in Table 4.2.

The solution is again sensitive to the stabilisation parameter β coming from Nitsche's method (3.3) and stabilisation parameter σ from weak formulation (6) for $\mathbf{H}(\text{div}, \Omega)$-conforming methods. The optimal value is experimentally set as $\beta = 10$ and $\sigma = 10$. The grad-div stabilisation (3.29) with parameter α around 0.1 is used

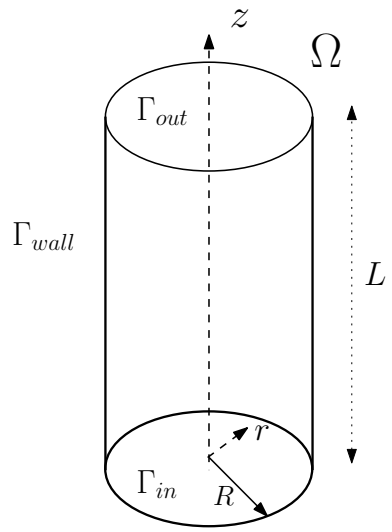

Figure 4.5: Geometry for Poiseuille flow in tube in three dimensions.

Table 4.2: Chosen values of parameters for Poiseuille flow in straight tube.

Symbol	Name	Value	Unit
ρ	density	1050	$\mathrm{kg.m^{-3}}$
μ	dynamic viscosity	3.896×10^{-3}	$\mathrm{kg.m^{-1}.s^{-1}}$
R	radius of the cylinder	12×10^{-3}	m
L	length of the cylinder	44×10^{-3}	m
γ	slip parameter	3.08	$\mathrm{m^2.s.kg^{-2}}$
V	mean inflow velocity	0.5	$\mathrm{m.s^{-1}}$

for all finite elements. $\mathbf{H}(\mathrm{div}, \Omega)$-conforming elements are computed with upwind stabilisation.
The theoretical error estimates for Stokes problem reads (2) for TH_k element and (3.43), (3.44) for RT_{k+1} (mathematically RT_k) and BDM_k element. Since the exact solution is regular enough, setting $k = 2$ for all further computations, we should theoretically get for all elements EOC = 2 for both velocity H^1 error and pressure L^2 error. Note that in (4.20) we still take into the account the convective term, hence it can also have a slight impact to the theoretical estimates.

Results for $\theta = 1$. Figure 4.6 shows convergence of relative errors for velocity and pressure and also L^2 norm of divergence for Poiseuille flow with no-slip ($\theta = 1$) on Γ_{wall}. For all used finite elements there is an improvement in using piecewise quadratic rather than piecewise linear boundary. The EOC results for H^1 velocity error is about a half order lower for $l = 1$ then the theoretical estimates, however for $l = 2$ EOC is even greater than theoretical estimate. The pressure error give for both $l = 1$ and $l = 2$ higher estimates then theoretical one, however computations with $l = 2$ are about 2 orders higher than for $l = 1$. Using TH finite elements over RT and BDM elements gives more accurate results, expect of the velocity H^1 error with $l = 1$. Otherwise RT and BDM elements always needs more degrees of freedoms to get to the same error.

Results for $\theta = 0.8$. Figure 4.7 shows the results imposing Navier's slip boundary condition on Γ_{wall} with $\theta = 0.8$. For all finite elements the resulting EOC is lower then in no-slip case, mainly for $l = 1$. Such observation can represent the worse enforcement of some slip on non-smooth boundary, rather than enforcement of the zero velocity on the wall. The effect of worse convergence of errors using $l = 1$ with $\theta = 0.8$ than $\theta = 1$ is more significant for RT and BDM elements. All the figures 4.6-4.7 demonstrates on last graph, that $\mathbf{H}(\text{div}, \Omega)$-conforming RT and BMD elements satisfy the incompressibility condition $\text{div}\,\mathbf{v} = 0$ as opposed to TH finite element.
Figure 4.8 captures convergence of the absolute errors of characteristic quantities defined in 4. The improvement of results using $l = 2$ is also visible. The best approximations seems to be using TH finite elements. Figure 4.9-4.10 shows the effect of varying slip parameter θ on flow quantities, computed on coarse mesh ($h_{min} = 3.05 \times 10^{-3}$) and fine mesh ($h_{min} = 7.62 \times 10^{-4}$) respectively.

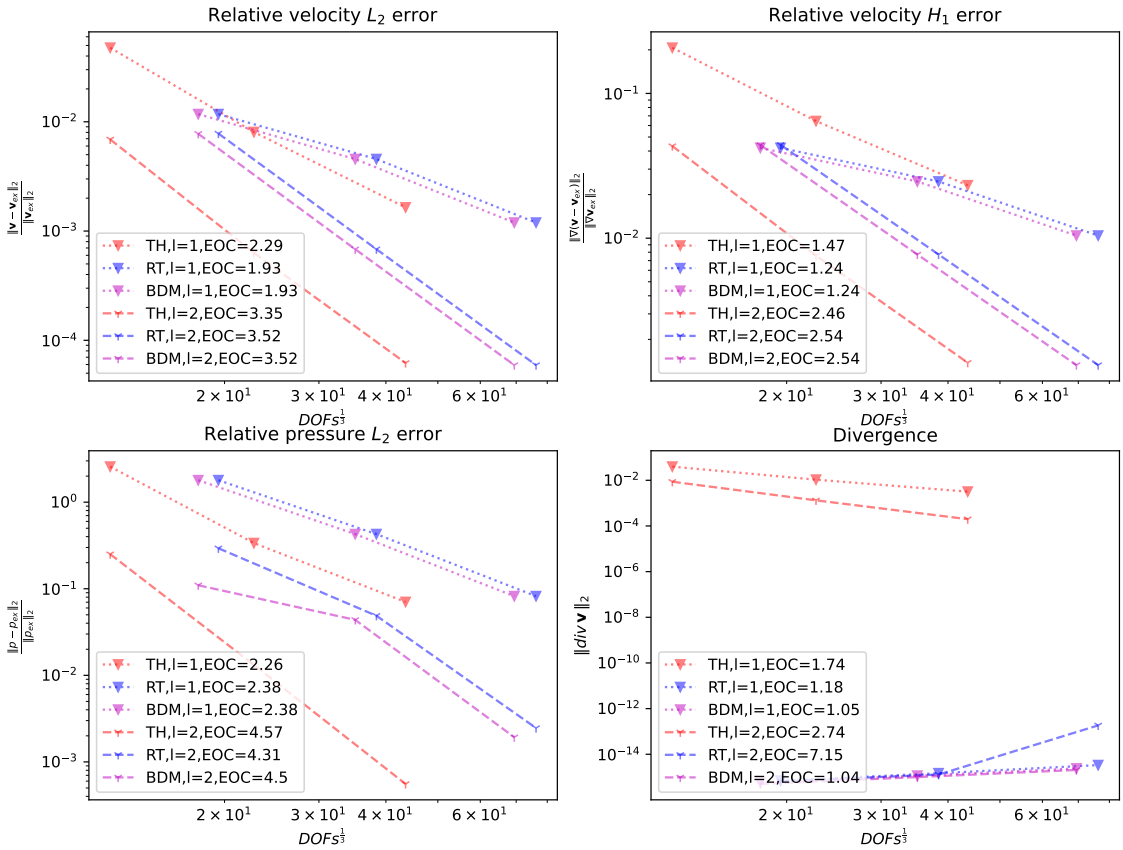

Figure 4.6: Convergence of errors, EOC and norm of the velocity divergence for Poiseuille flow with no-slip ($\theta = 1$) on the boundary using piecewise linear $l = 1$ (lines with triangles) and piecewise quadratic $l = 2$ (lines with stars) boundary and for TH_2, RT_3, BDM_2 finite elements.

Assume two same problems with same data on the same mesh, where one is discretised with usual piecewise linear boundary and the other allowing more smoother piecewise quadratic boundary. Previous examples show that we can get two different solutions even for fine meshes, where the second one with smoother boundary is more accurate one.

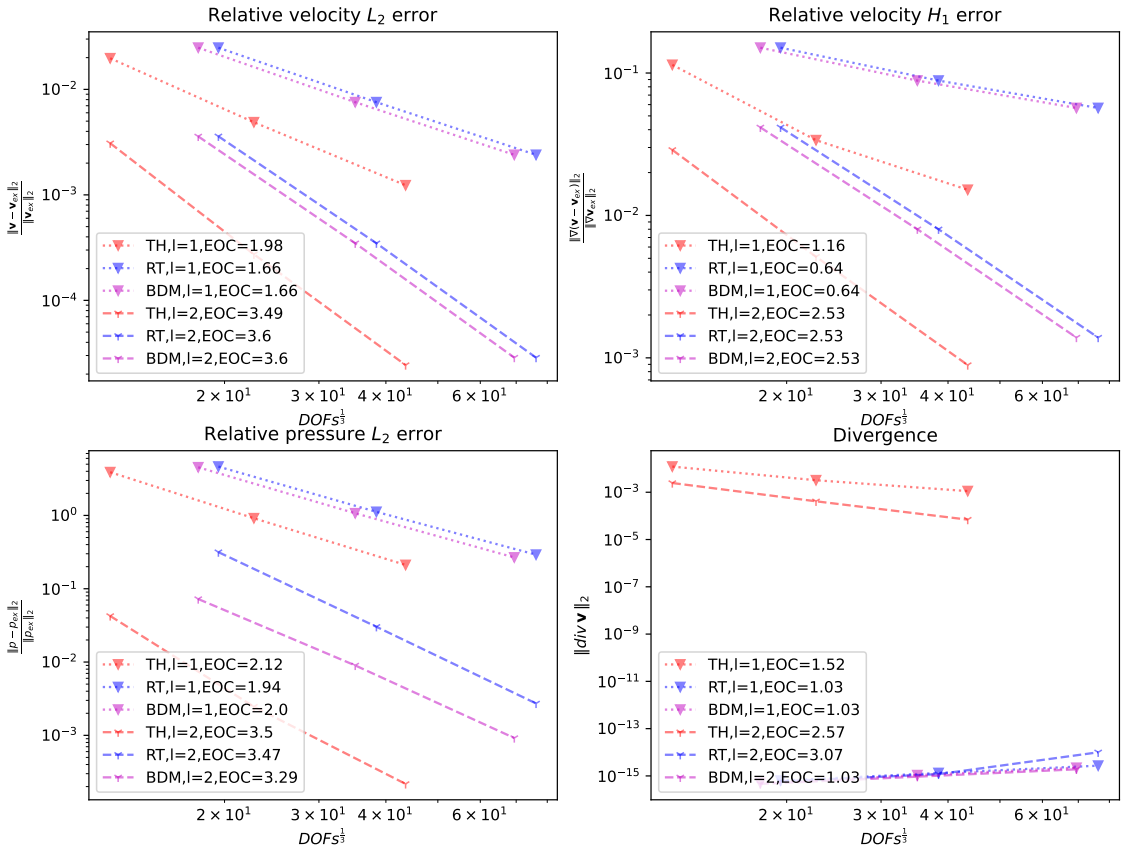

Figure 4.7: Convergence of errors, EOC and norm of the velocity divergence for Poiseuille flow with partial slip ($\theta = 0.5$) on the boundary using piecewise linear $l = 1$ (lines with triangles) and piecewise quadratic $l = 2$ (lines with stars) boundary and for TH_2, RT_3, BDM_2 finite elements.

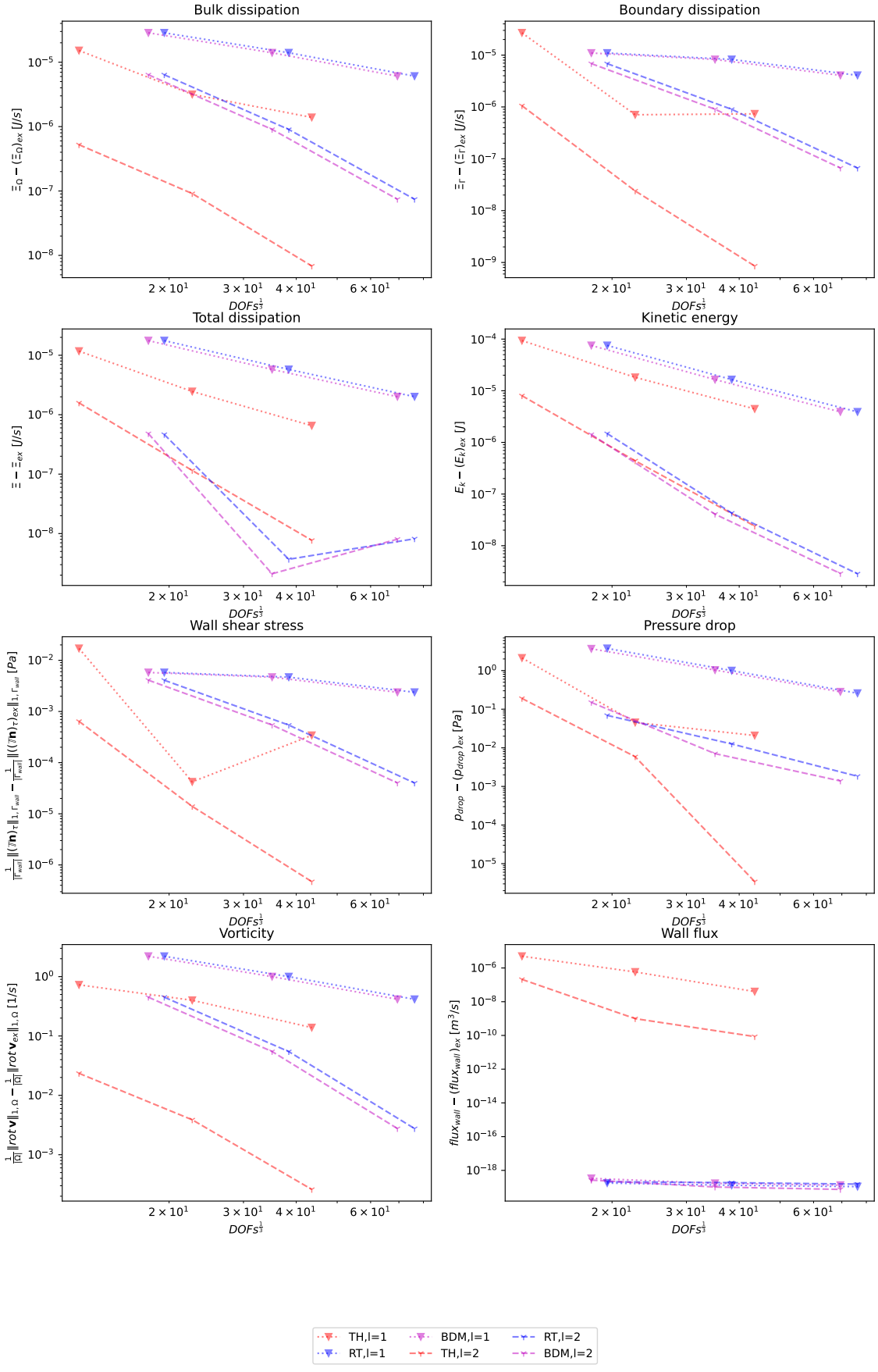

Figure 4.8: Error convergence of flow characteristics for Poiseuille flow with partial slip ($\theta = 0.8$) on the boundary, for piecewise linear $l = 1$ (lines with triangles) and piecewise quadratic $l = 2$ (lines with stars) boundary and for TH_2, RT_3, BDM_2 finite elements.

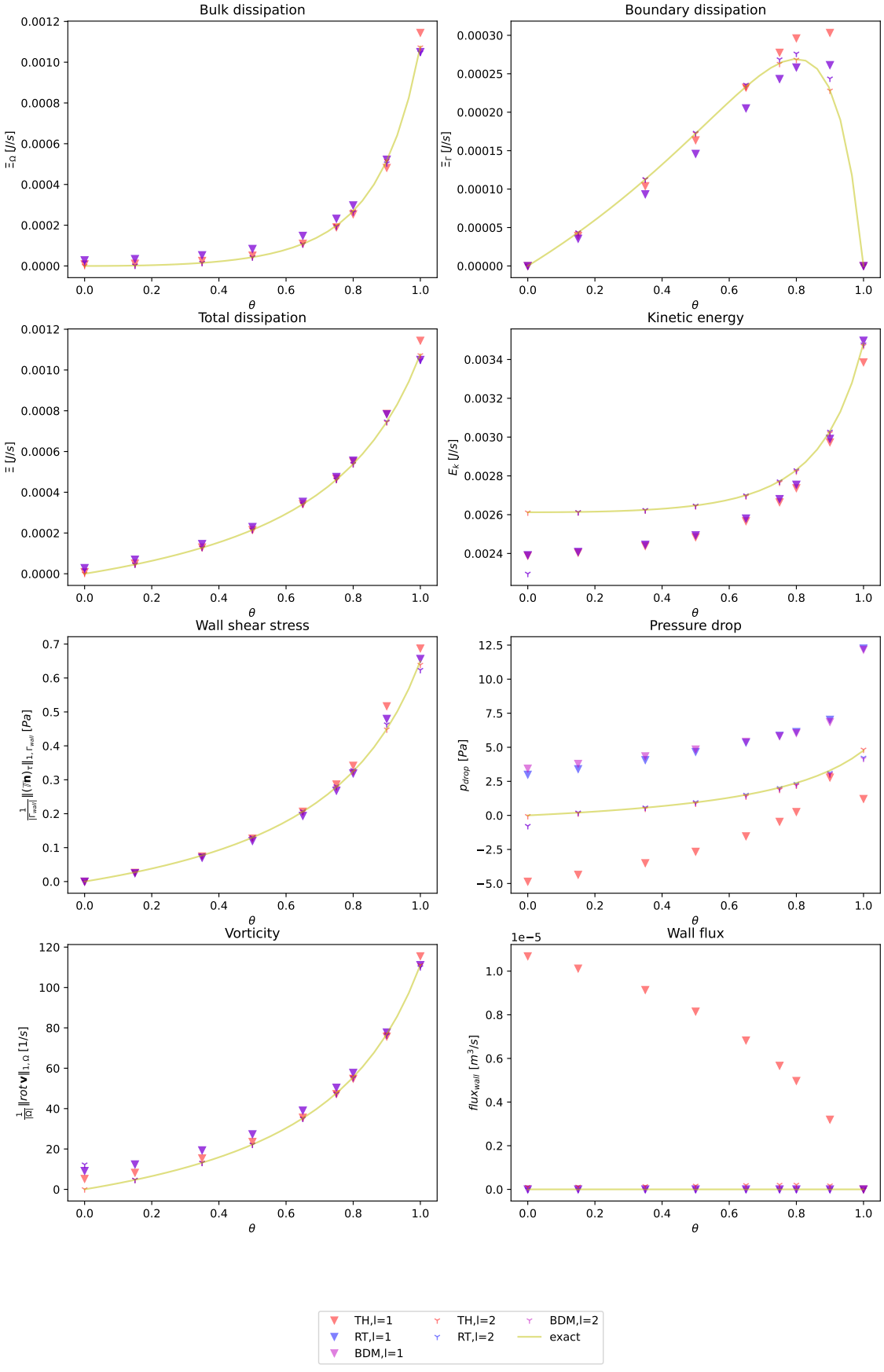

Figure 4.9: Flow quantities for values $\theta \in \{0, 0.15, 0.35, 0.5, 0.65, 0.75, 0.8, 0.9, 1\}$ on coarse mesh ($h_{min} = 3.05 \times 10^{-3}$) using piecewise linear $l = 1$ (triangles) and piecewise quadratic $l = 2$ (stars) boundary and for for TH_2, RT_3, BDM_2 finite elements.

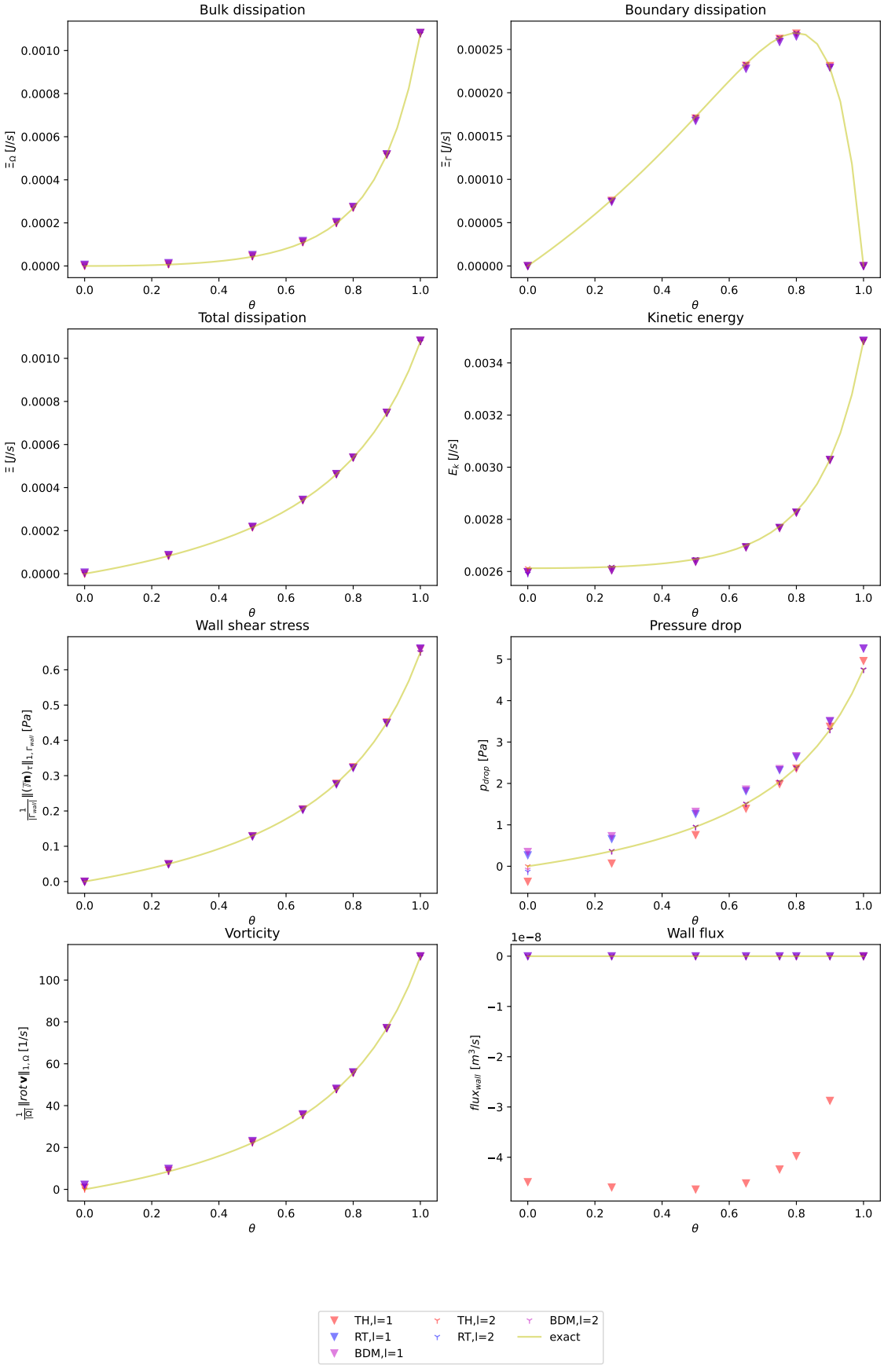

Figure 4.10: Flow quantities for values $\theta \in \{0, 0.25, 0.5, 0.65, 0.75, 0.8, 0.9, 1\}$ on fine mesh ($h_{min} = 7.62 \times 10^{-4}$) using piecewise linear $l = 1$ (triangles) and piecewise quadratic $l = 2$ (stars) boundary and for TH_2, RT_3, BDM_2 finite elements.

4.2 Simulations of flow in aortic root

Finally, we show the obtained results for the flow in the aortic root described by the equations (1.1)-(1.8). Numerical test are for values of constant parameters given in Table 4.3, which are taken from [34] also with dimensions of the computational domain, provided in Figure 3.5. The characteristic radius is $r_{char} = 16$ in the middle of the sinus extension, for either axially symmetric shape or shape with three sinuses, see Figure 3.6. We are interested in solution which are driven by the inflow velocity

Table 4.3: Chosen values of parameters for flow in the aortic root.

Symbol	Name	Value	Unit
ρ	density	1050	$\mathrm{kg.m^{-3}}$
μ	dynamic viscosity	3.896×10^{-3}	$\mathrm{kg.m^{-1}.s^{-1}}$
r_{char}	characteristic radius of the domain	16×10^{-3}	m
L	length of the domain	44×10^{-3}	m
γ	slip parameter	3.08	$\mathrm{m^2.s.kg^{-3}}$
V	mean inflow velocity	0.65	$\mathrm{m.s^{-1}}$

$\mathbf{v}_{\mathrm{in}}$ in form of the parabolic velocity profile, obtained by the Poiseuille flow (4.29), whose magnitude is scaled by the time-dependent factor, thus

$$\mathbf{v}_{\mathrm{in}}(\mathbf{x},t) = \left(0, 0, f(t)V\frac{4\mu\gamma R_{in}(1-\theta) + 2\theta(R_{in}^2 - r^2)}{R_{in}\left[4\gamma\mu(1-\theta) + \theta R_{in}\right]}\right), \tag{4.31}$$

where

$$f(t)\begin{cases} t & \text{if } 0 \le t \le 1 \\ 1 & \text{if } t > 1 \end{cases}$$

and $R_{in} = 0.012$ m is the radius on Γ_{in}.
At the beginning $t = 0$ s, we set zero inflow condition, which slowly increases in form of the parabolic profile up to $t = 1$ s. Then it remains as the fixed parabolic profile with set mean inflow velocity V. Thus the inflow boundary condition is after 1 second stationary. With such setting we investigate, how the solution behaves for bigger times, for example if they develop into stationary solutions or if they remains unsteady. In our case, we compute the solution up to a fixed time $T = 5$ seconds, as it appears that for states converging to stationary solutions, this convergence occurs within this time frame.
For discretisation in time we use the BDF2 scheme, presented in (3.6) with fixed time step $\Delta t = 0.005$ s. We use the weak formulation in (2) for discretising in space by Taylor-Hood (TH) element and weak formulation in (6) when using $\mathbf{H}(\mathrm{div}, \Omega)$-conforming Raviart-Thomas (RT) and Brezzi-Douglas-Marini (BDM) elements. In computations we will further use only BDM element from $\mathbf{H}(\mathrm{div}, \Omega)$-conforming methods, since it generally provides more accurate results, according to examples in section 4.1 and mainly it has less degrees of freedom than RT element (some examples of degrees of freedoms for both RT and BDM elements are for illustration in section 3.2.3).
The penalty parameters β, σ from Nitshce's method (3.3) and from penalisation term in weak formulation (6) respectively, are chosen as $\beta = 100$, $\sigma = 100$. For

both TH and BDM element we add the grad-div stabilisation (3.29) with $\alpha = 10$ and $\alpha = 100$ respectively. For BDM element we also use the upwind stabilisation.
We use finite element spaces that are piecewise quadratic in velocities and piecewise linear in pressure, i.e. TH_2, BDM_2 elements with both meshes with piecewise linear ($l = 1$) and piecewise quadratic ($l = 2$) boundary (for such setting the results in chapter 4.1 reveals improvement of the convergence with $l = 2$).
The problem will be tested on two meshes, axially symmetric one with minimal size of the element $h_{min} = 9.24 \times 10^{-4}$ and on one with three sinuses with $h_{min} = 8.91 \times 10^{-4}$, see Figure 3.6.
For all the solutions we compute the flow quantities, defined in section 4.

4.2.1 Flow in the axially symmetric domain

Firstly, we show the graphs for flow in axially symmetric domain, using both TH and BDM element with = 1 and $l = 2$. Figure 4.11 shows values of the flow quantities at $t = 5$ s, where we vary the Navier's slip parameter θ. As we will see on next figures, depending on θ, some solutions goes to stationary states. For those who do not, we get the value by averaging values in last two seconds.
The general behaviour depending on θ is as follows. It turns out that for low values of θ (bigger allowed slip), the solution is stationary (almost right after 1 second) and no vortices occur. After some critical value of θ, the flow becomes unsteady or even chaotic as the vortices in the sinus extension starts to generate. However for a higher values of θ, usually around 0.96, the solutions become steady with some slow recirculation in the sinus extension. The critical values of θ, where the vortices starts to generate are approximately as follows: $\theta = 0.65$ for TH $l = 1$, $\theta = 0.8$ for TH $l = 2$, $\theta = 0.5$ for BDM $l = 1$, $\theta = 0.8$ for BDM $l = 2$. It can be seen on Figures 4.12-4.16, which captures the evolution of the flow quantities for picked (critical) parameters θ. For example in Figure 4.13 with $\theta = 0.65$ can be seen the difference of flow character between $l = 1$ and $l = 2$ for both TH and BDM elements. For lower θ, for example $\theta = 0.5$ in Figure 4.12, the BDM element together with $l = 1$ goes to different, non-stationary, solution as opposed to the other options. For higher parameter θ, for example $\theta = 0.96$ in Figure 4.15, BDM method seems to stabilise more sooner then TH element.
Also note that the BDM element with $l = 2$ for all θ should give zero values of wall flux, due to the diverge-free property (3.35), as we see for solutions with $l = 1$ or as we demonstrated in the benchmark problems in section 4.1. We do not have explanation for this behaviour now and it is not clear whether there is a bug in our script or in software's libraries.
Figure 4.17 shows the surface velocities at $t = 5$ s for $l = 2$ for TH element and Figure 4.18 illustrates the different solution obtained by TH and BDM elements for $\theta = 0.96$, which can be seen in Figure 4.15. Figures 4.19 and 4.20 shows the velocity, instantaneous streamlines and vorticity on the cuts of the domain, illustrating the generation of vortices for different slip parameter, with $l = 2$ using TH. Figure 4.21 captures the periodic behaviour of the solution for $\theta = 0.65$, with $l = 1$, using TH element (see Figure 4.13). During the one period, a vortex begins to form in the sinusoidal extension (always in the same place), which increases in size and eventually flows out of the domain.

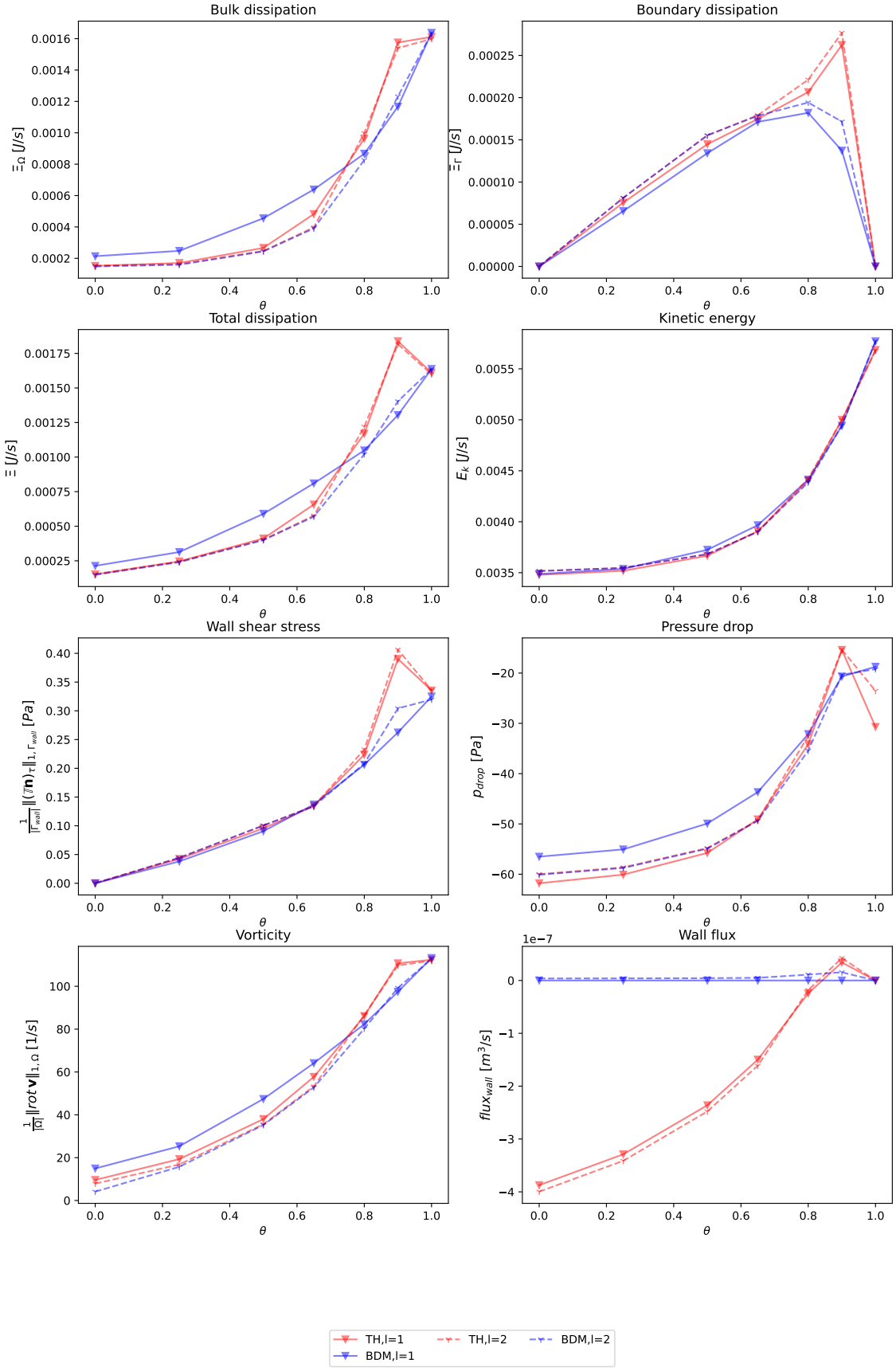

Figure 4.11: Flow quantities at time $t = 5$ s, for $\theta \in \{0.0, 0.5, 0.65, 0.8, 0.9, 1\}$, with both piecewise linear ($l = 1$) and quadratic ($l = 2$) boundary, using TH and BDM element on axially symmetric mesh.

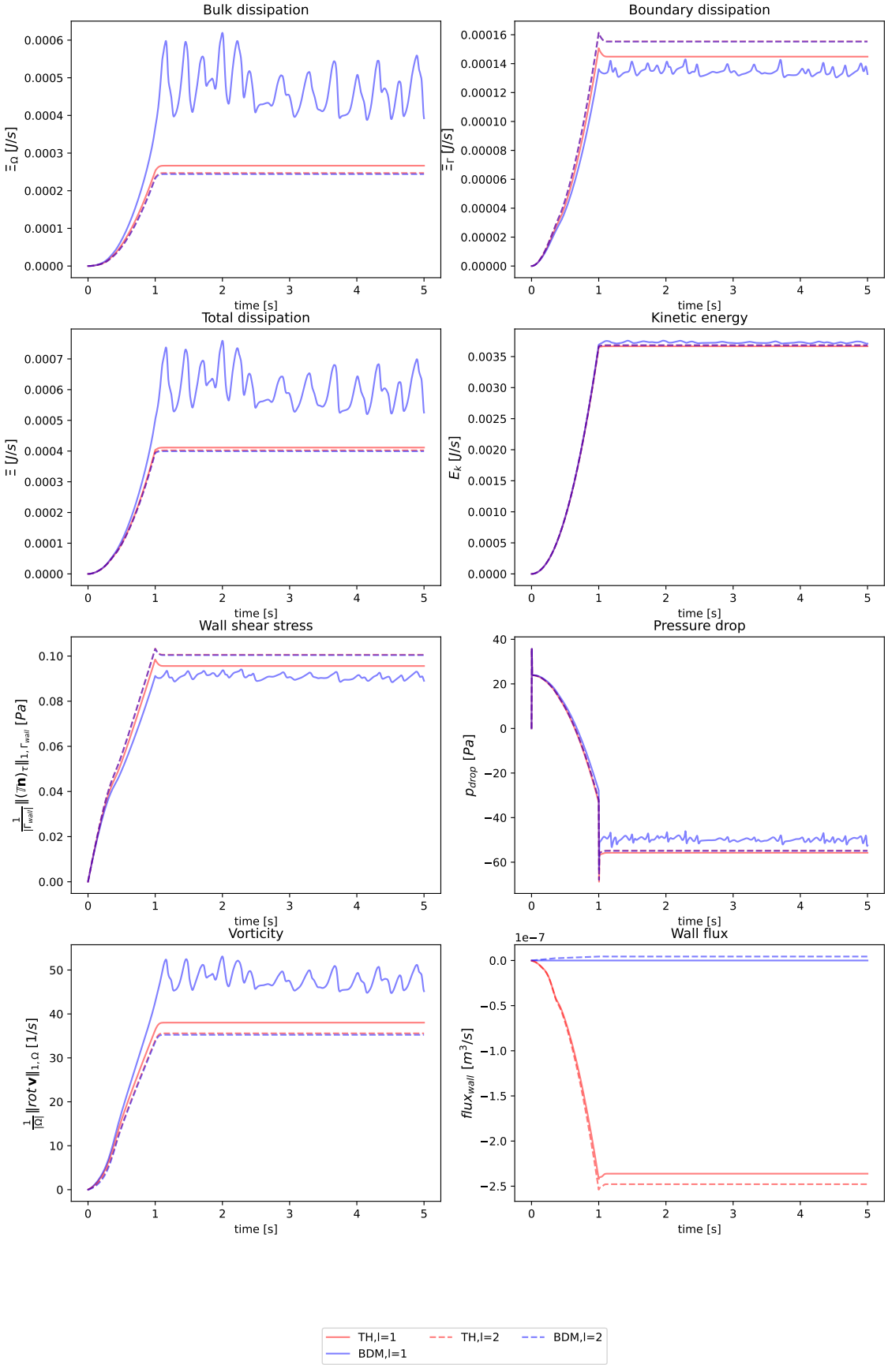

Figure 4.12: Flow quantities in time $t \in [0, 5]$ s for $\theta = 0.5$, with both piecewise linear ($l = 1$) and quadratic ($l = 2$) boundary, using TH and BDM element on axially symmetric mesh.

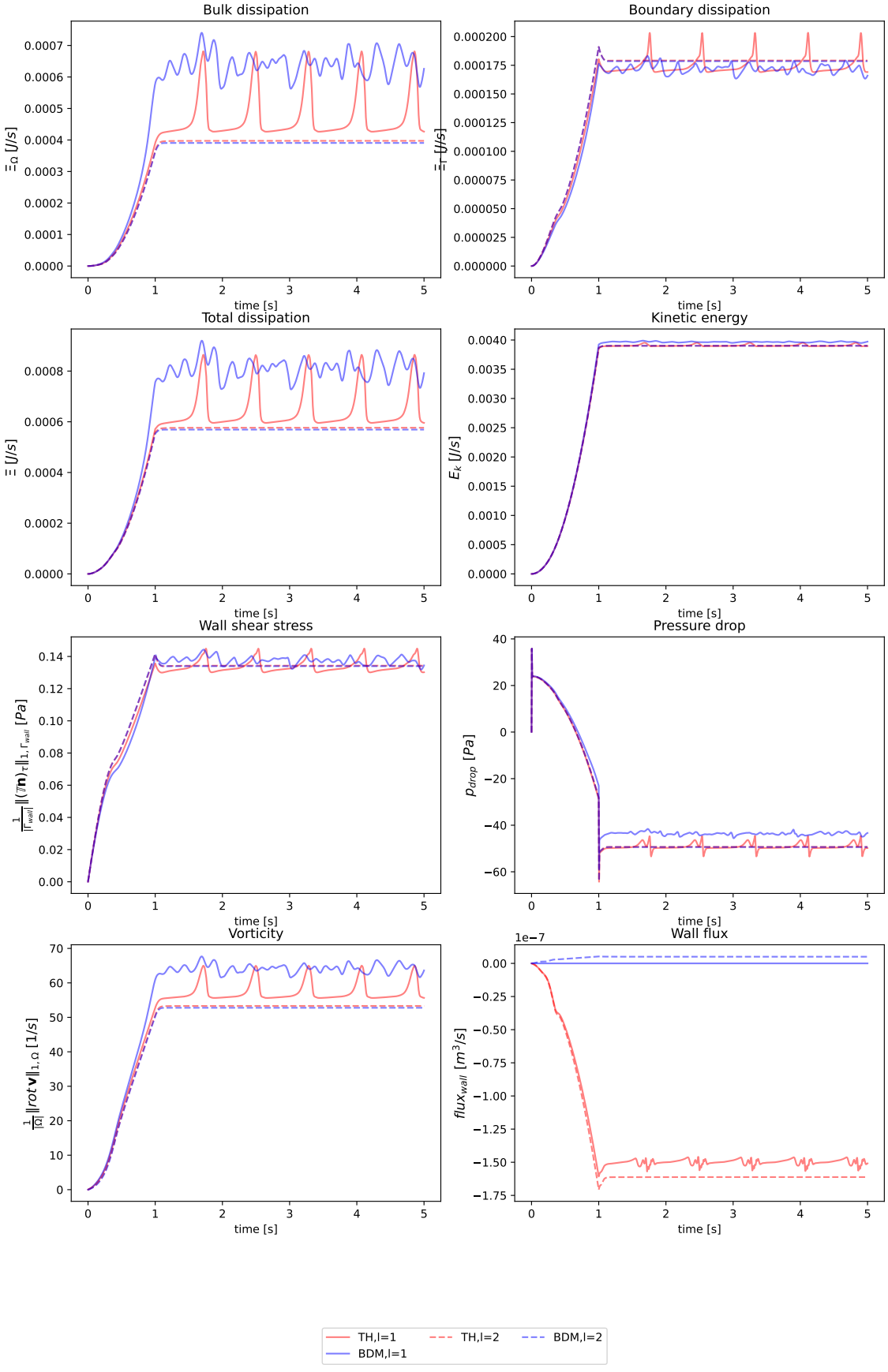

Figure 4.13: Flow quantities in time $t \in [0, 5]$ s for $\theta = 0.65$, with both piecewise linear ($l = 1$) and quadratic ($l = 2$) boundary, using TH and BDM element on axially symmetric mesh.

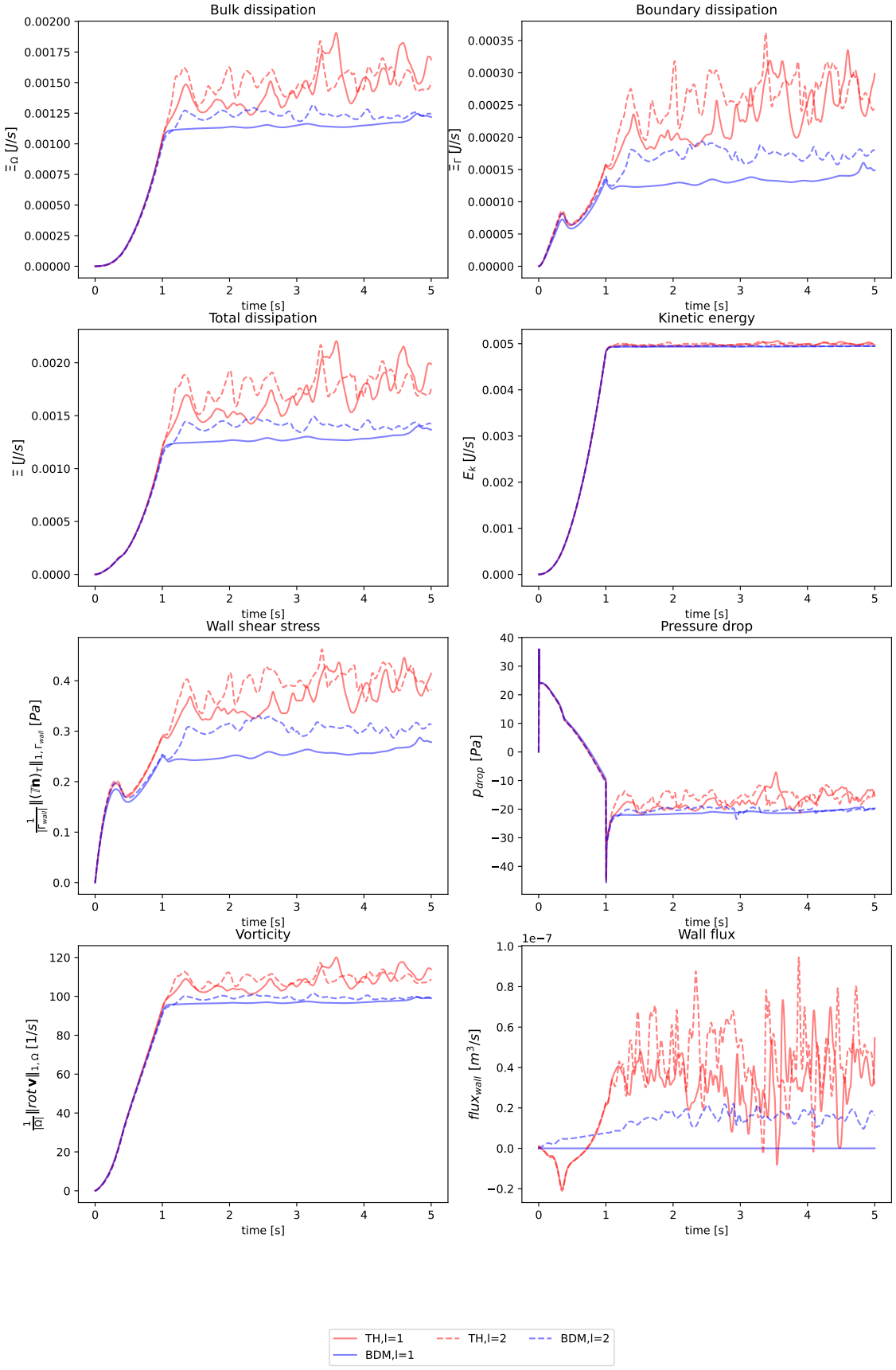

Figure 4.14: Flow quantities in time $t \in [0, 5]$ s for $\theta = 0.9$, with both piecewise linear ($l = 1$) and quadratic ($l = 2$) boundary, using TH and BDM element on axially symmetric mesh.

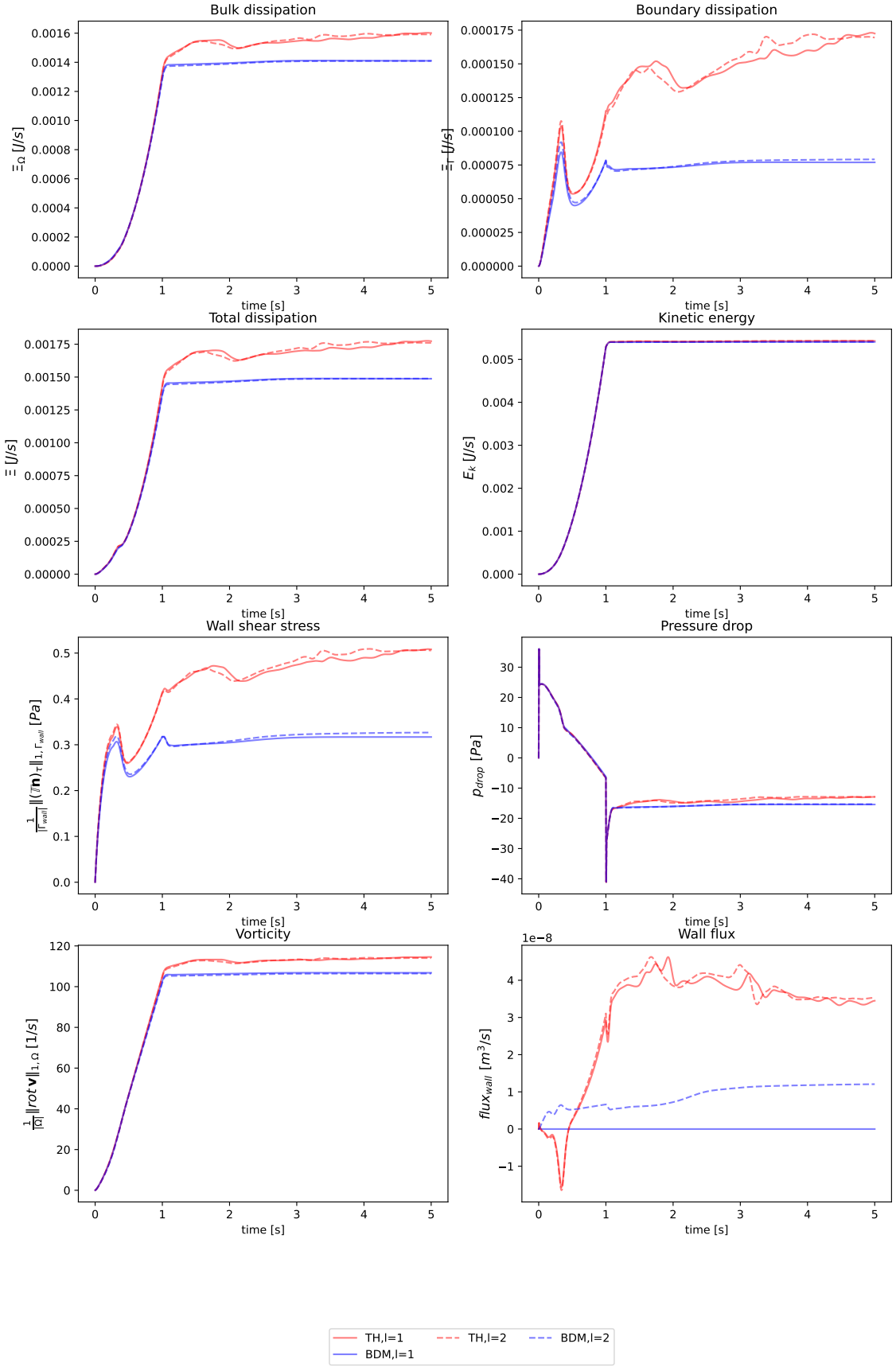

Figure 4.15: Flow quantities in time $t \in [0, 5]$ s for $\theta = 0.96$, with both piecewise linear ($l = 1$) and quadratic ($l = 2$) boundary, using TH and BDM element on axially symmetric mesh.

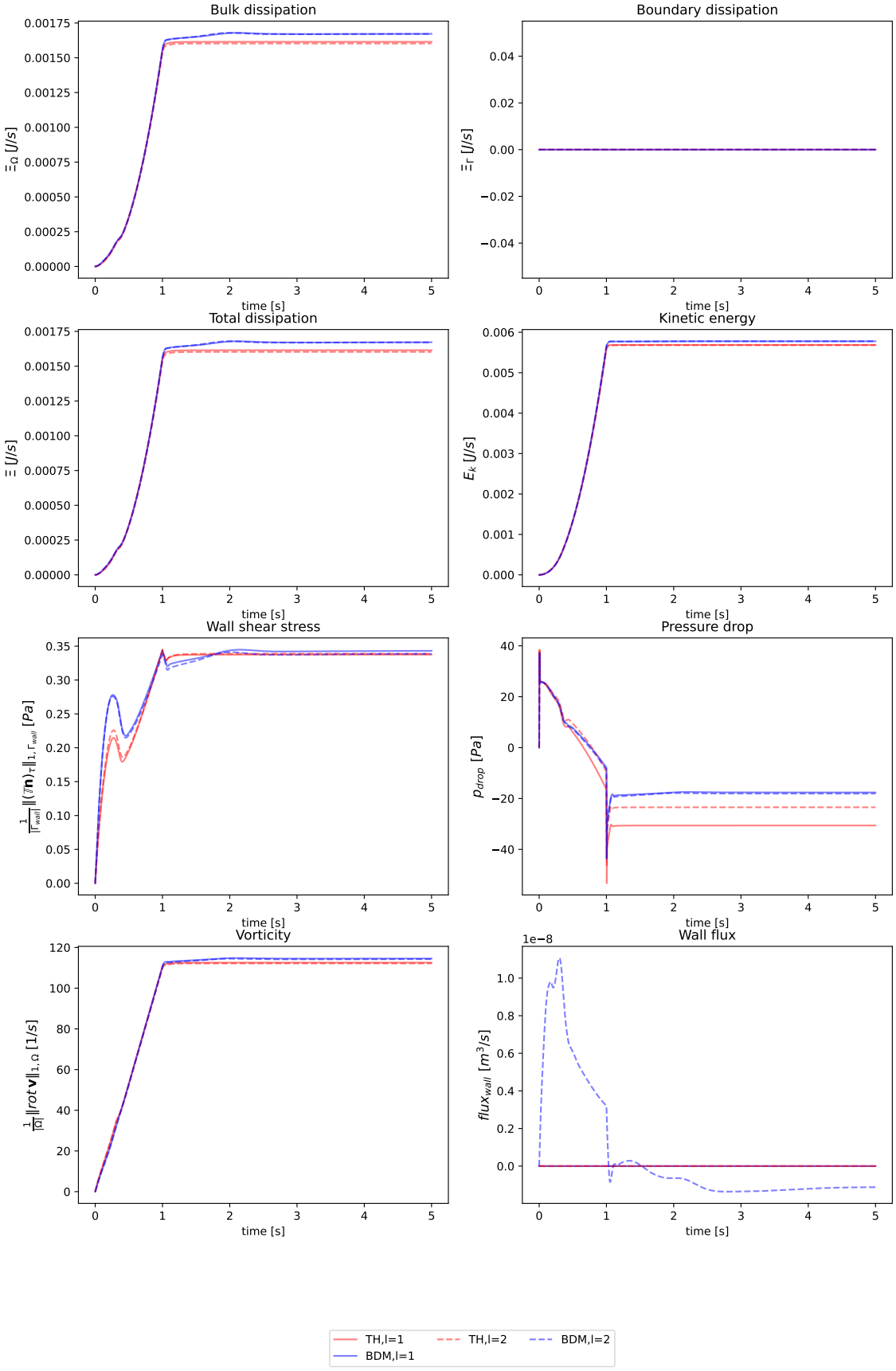

Figure 4.16: Flow quantities in time $t \in [0, 5]$ s for $\theta = 1$, with both piecewise linear ($l = 1$) and quadratic ($l = 2$) boundary, using TH and BDM element on axially symmetric mesh.

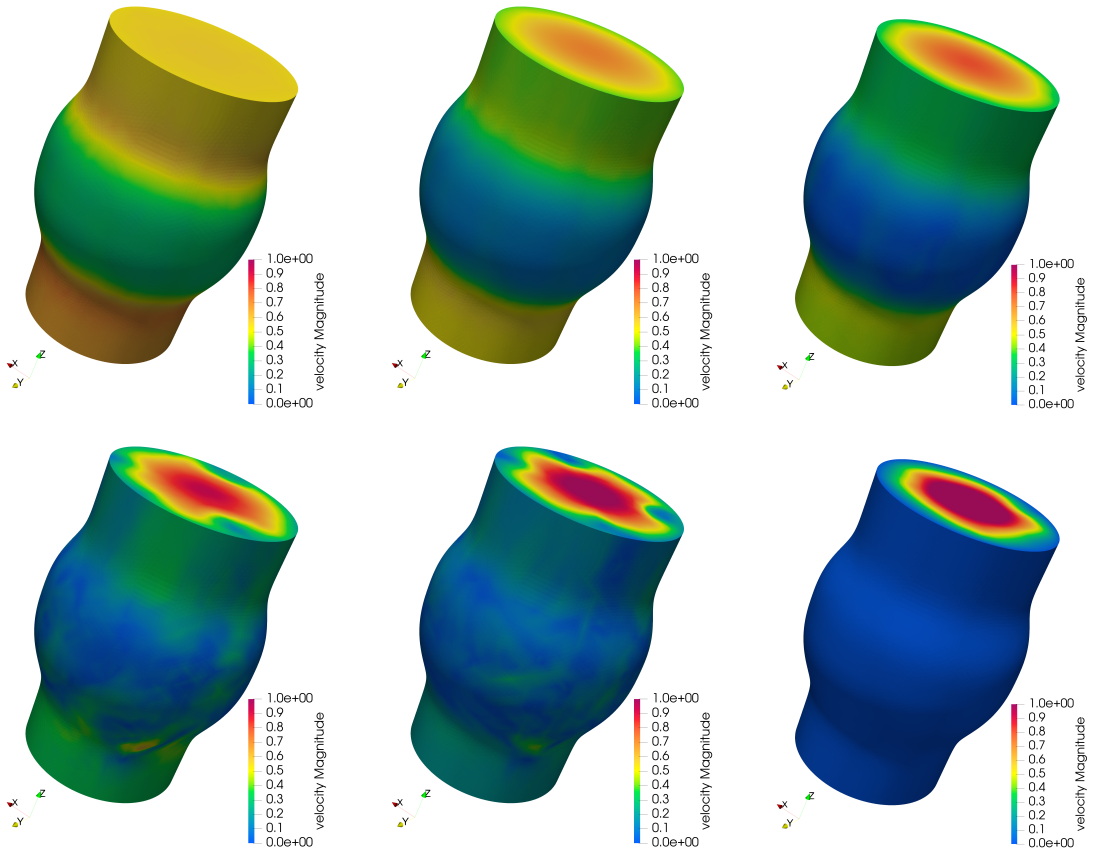

Figure 4.17: Surface velocities for flow in axially symmetric geometry, with $l = 2$, at time $t = 5$ s, using TH element, for $\theta \in \{0.0, 0.5, 0.65, 0.8, 0.9, 1\}$ respectively, on axially symmetric mesh.

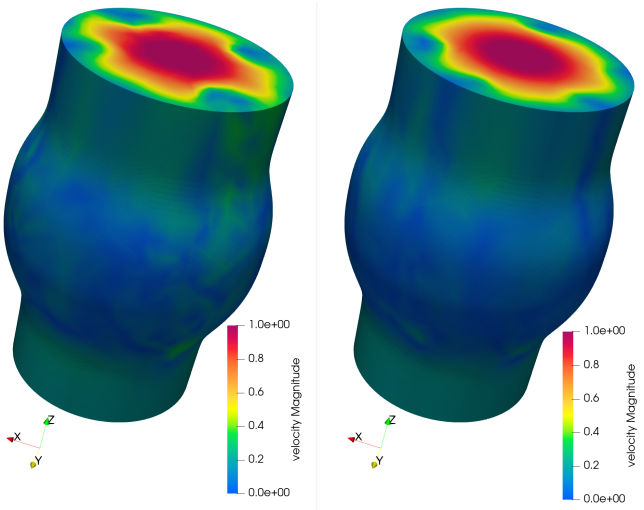

Figure 4.18: Surface velocities in time $t \in [0, 5]$ s for $\theta = 0.96$, with $l = 2$, using TH and BDM element on axially symmetric mesh.

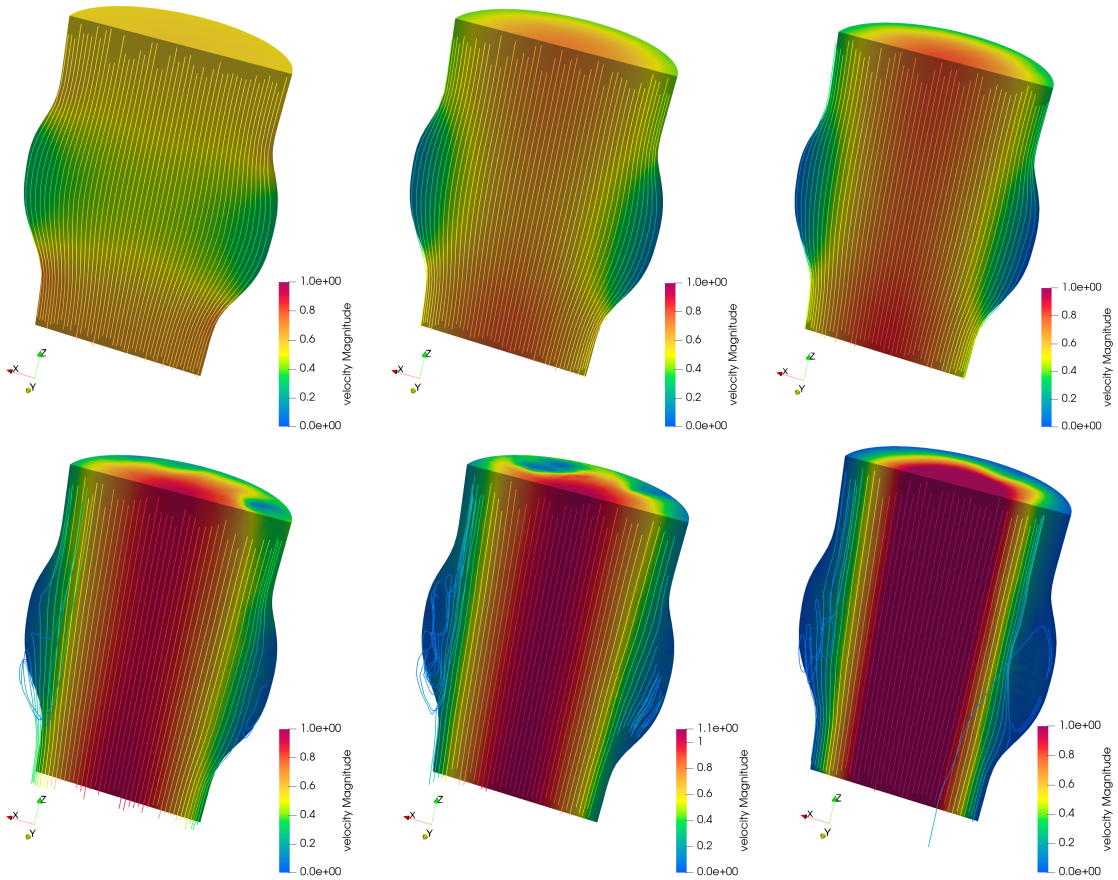

Figure 4.19: Velocity and streamlines on the cut of axially symmetric domain, at time $t = 5$ s, with $l = 2$, using TH element, for $\theta \in \{0.0, 0.5, 0.65, 0.8, 0.9, 1\}$.

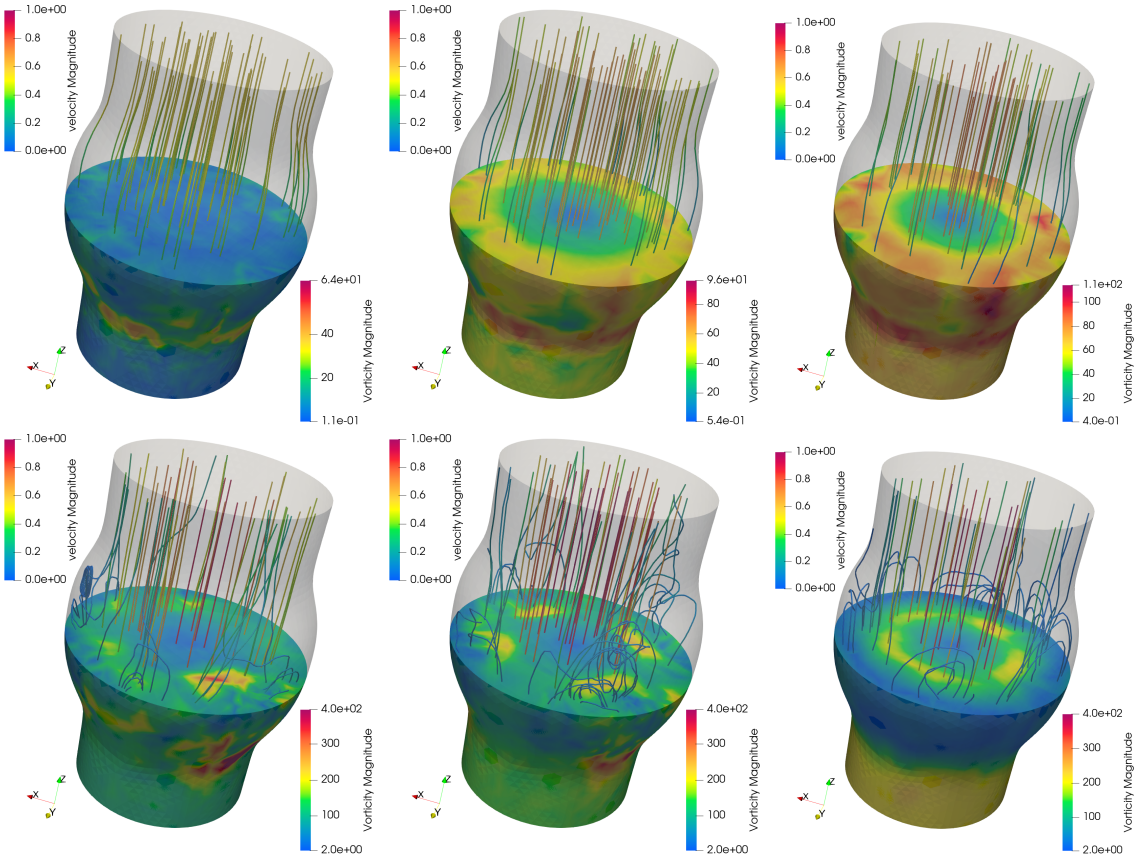

Figure 4.20: Streamlines coloured by velocity magnitude and vorticity on the cut of axially symmetric domain, at time $t = 5$ s, with $l = 2$, using TH element, for $\theta \in \{0.0, 0.5, 0.65, 0.8, 0.9, 1\}$.

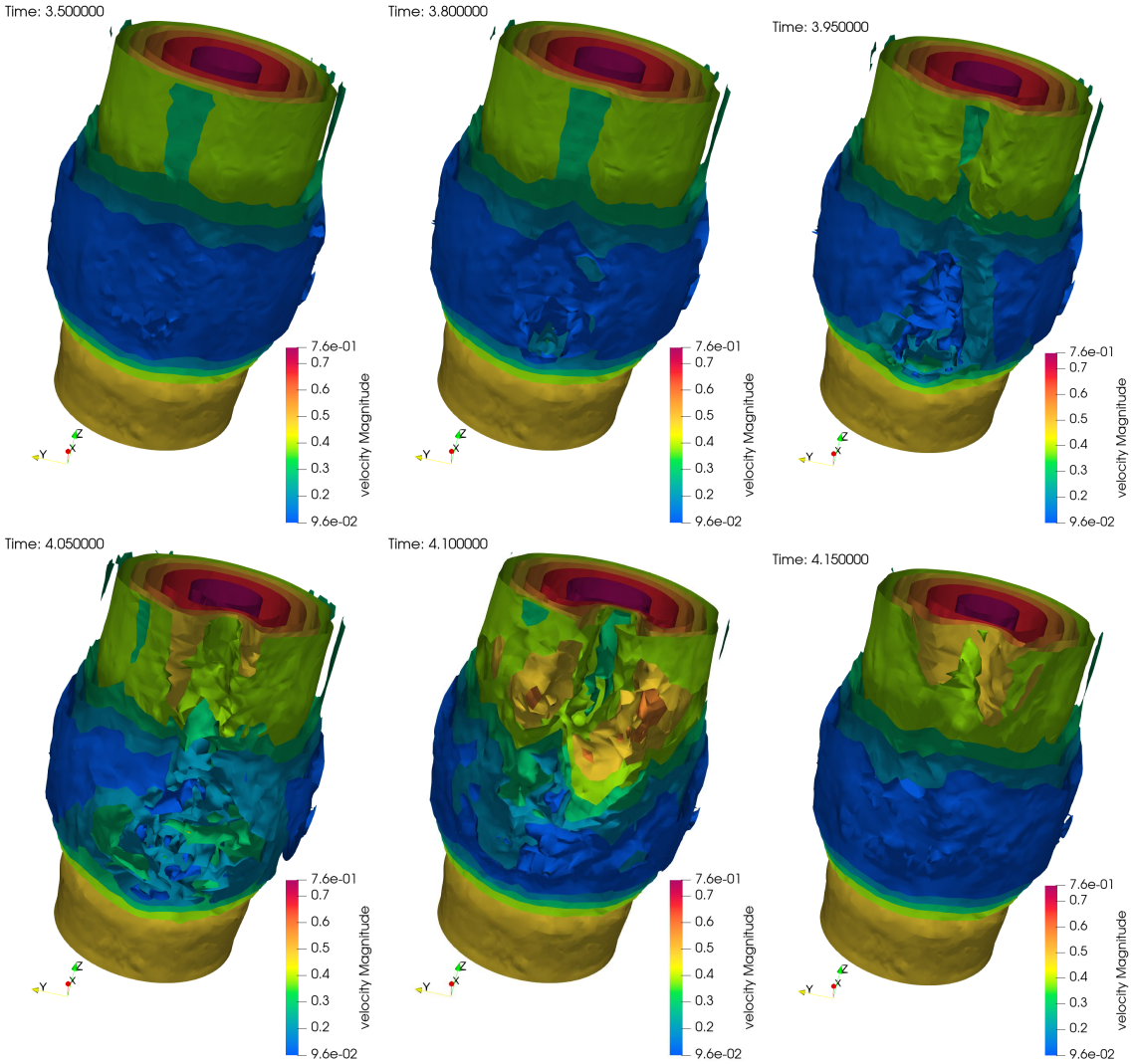

Figure 4.21: Magnitudes of velocities at times $t \in \{3.5, 3.8, 3.95, 4.05, 4.10, 4.15\}$ for flow in axially symmetric geometry with piecewise linear boundary, for $\theta = 0.65$, using TH element.

4.2.2 Flow in domain with three sinuses

Lastly, we show the graphs for flow in domain with three sinuses, using both TH and BDM element with = 1 and $l = 2$. Figure 4.22 shows values of the flow quantities at $t = 5$ s, where we vary the Navier's slip parameter θ. We observed, that the interval of parameters θ where the solution goes to stationary state, is more narrow. Here the critical values of θ, where the vortices starts to generate and the solution in unsteady are approximately as follows: $\theta = 0.33$ for TH and $l = 1$, $\theta = 0.4$ for TH and $l = 2$, $\theta = 0.4$ for BDM and $l = 2$. For BDM element and $l = 1$ we did not get a stationary solution for low values of θ, not even for $\theta = 0$, see Figure 4.23. Figures 4.24 again demonstrates the different solutions using piecewise linear and quadratic boundary for both elements. For a higher value $\theta = 0.9$, in 4.25, the BDM method seems to oscillates much less than the TH element and in 4.26 it stabilise more sooner.
Further, Figure 4.27 shows the surface velocities at $t = 5$ s for $l = 2$, for TH element. Figures 4.28 and 4.29 shows the velocity, instantaneous streamlines and vorticity on the cuts of the domain, illustrating the generation of vortices for different slip parameter, with $l = 2$ using TH element.

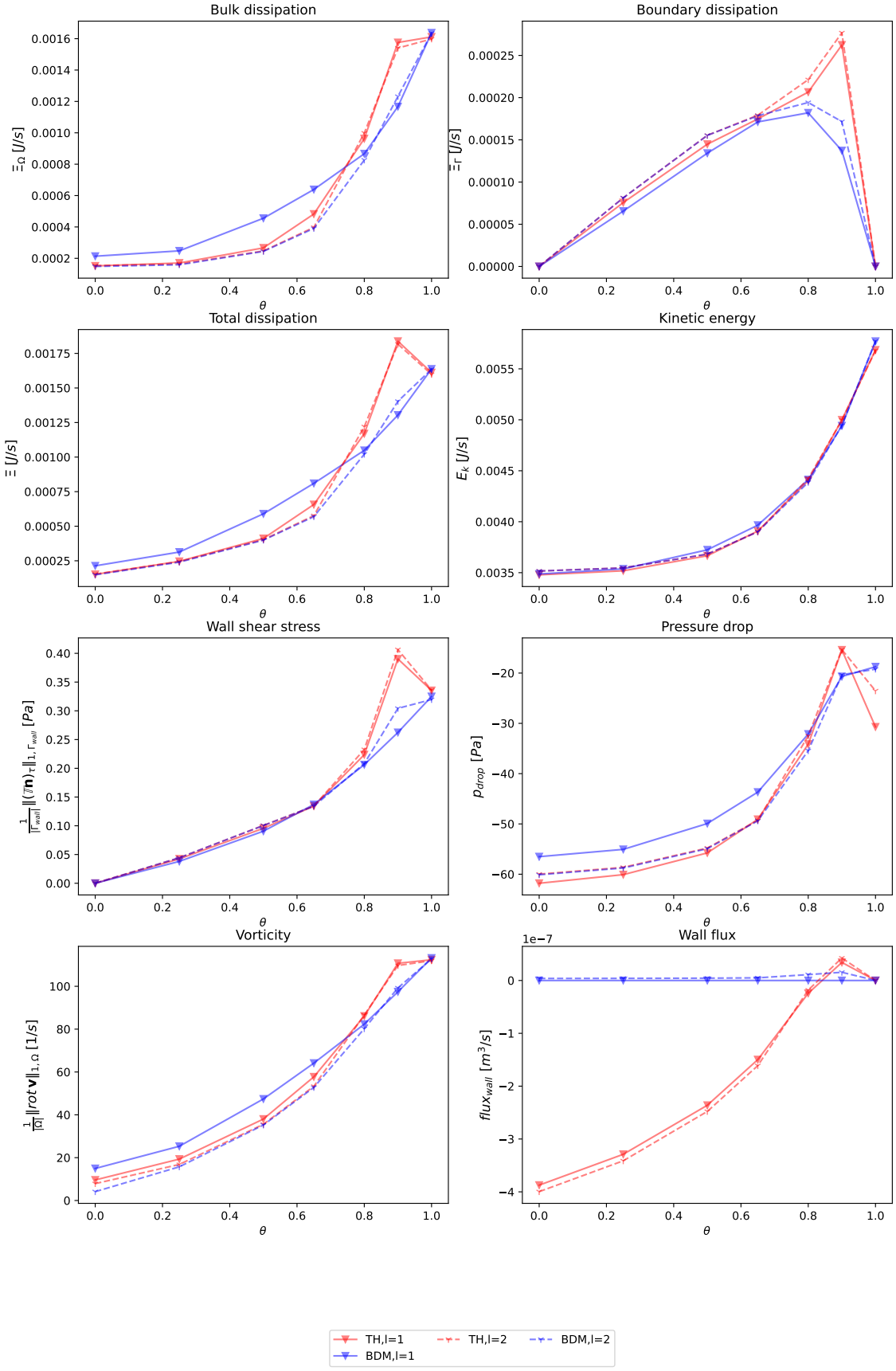

Figure 4.22: Flow quantities at time $t = 5$ s, for $\theta \in \{0.0, 0.5, 0.65, 0.8, 0.9, 1\}$, with both piecewise linear ($l = 1$) and quadratic ($l = 2$) boundary, using TH and BDM element on mesh with three sinuses.

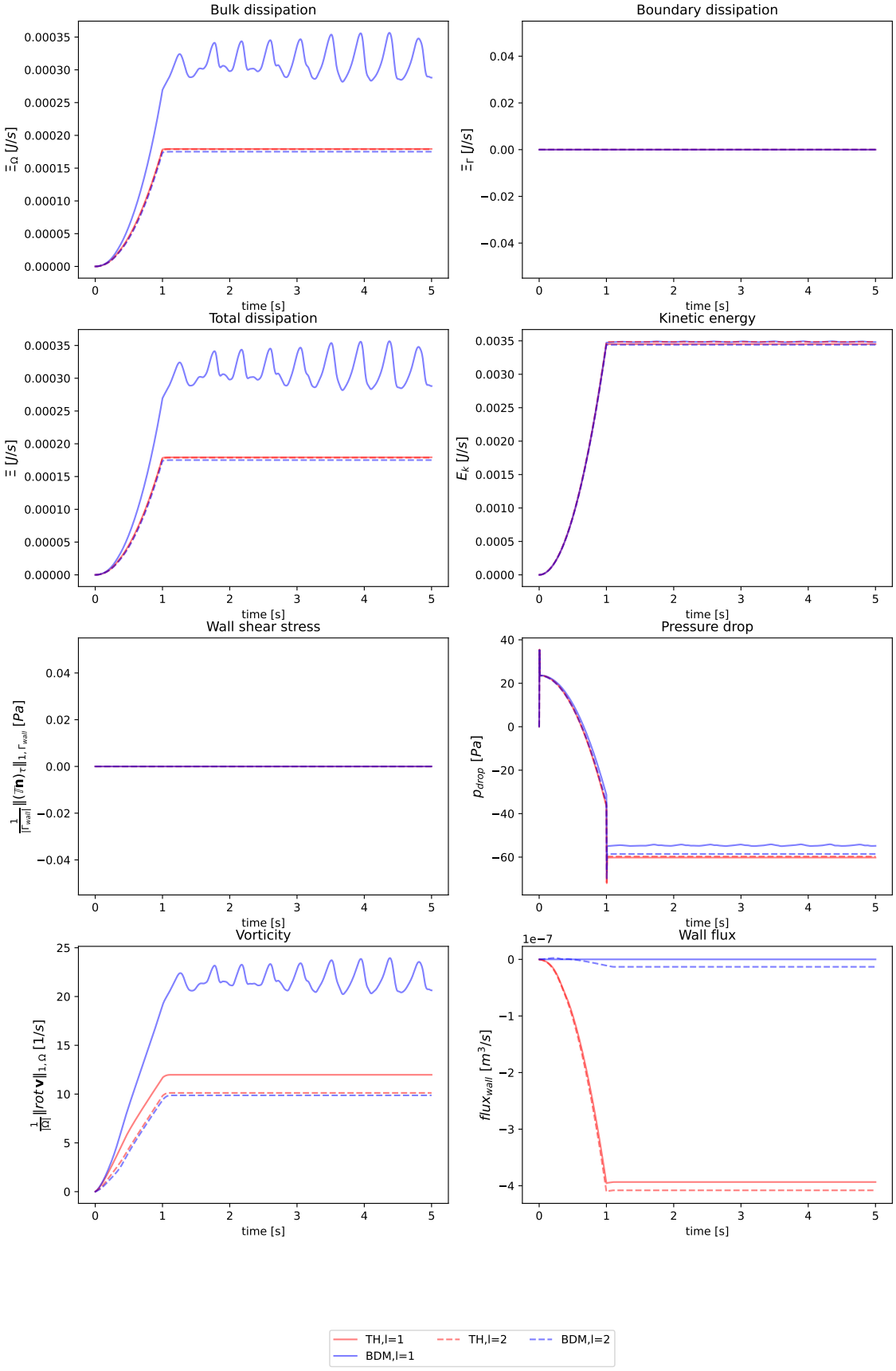

Figure 4.23: Flow quantities in time $t \in [0, 5]$ s for $\theta = 0.0$, with both piecewise linear ($l = 1$) and quadratic ($l = 2$) boundary, using TH and BDM element on mesh with three sinuses.

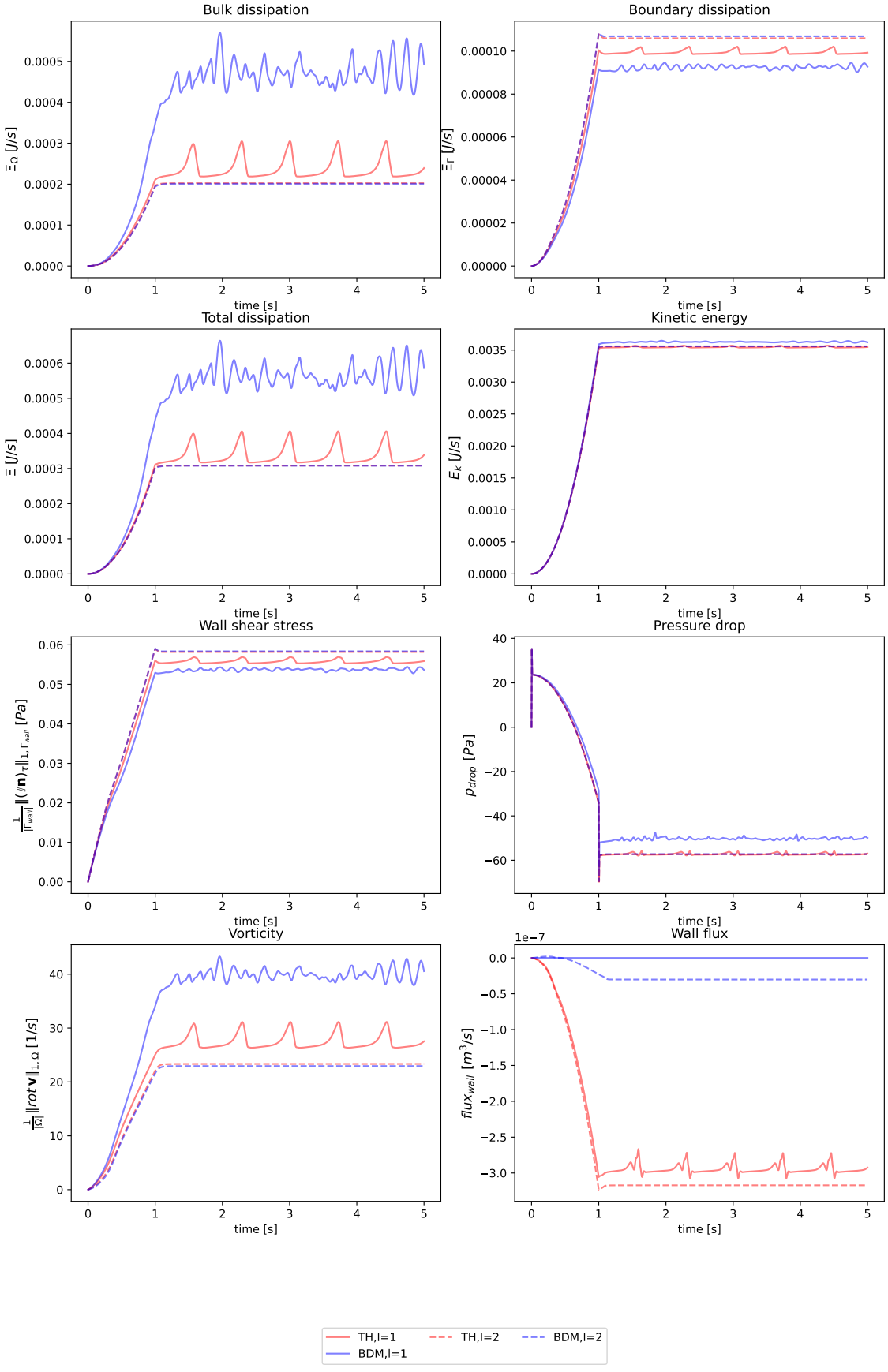

Figure 4.24: Flow quantities in time $t \in [0, 5]$ s for $\theta = 0.33$, with both piecewise linear ($l = 1$) and quadratic ($l = 2$) boundary, using TH and BDM element on mesh with three sinuses.

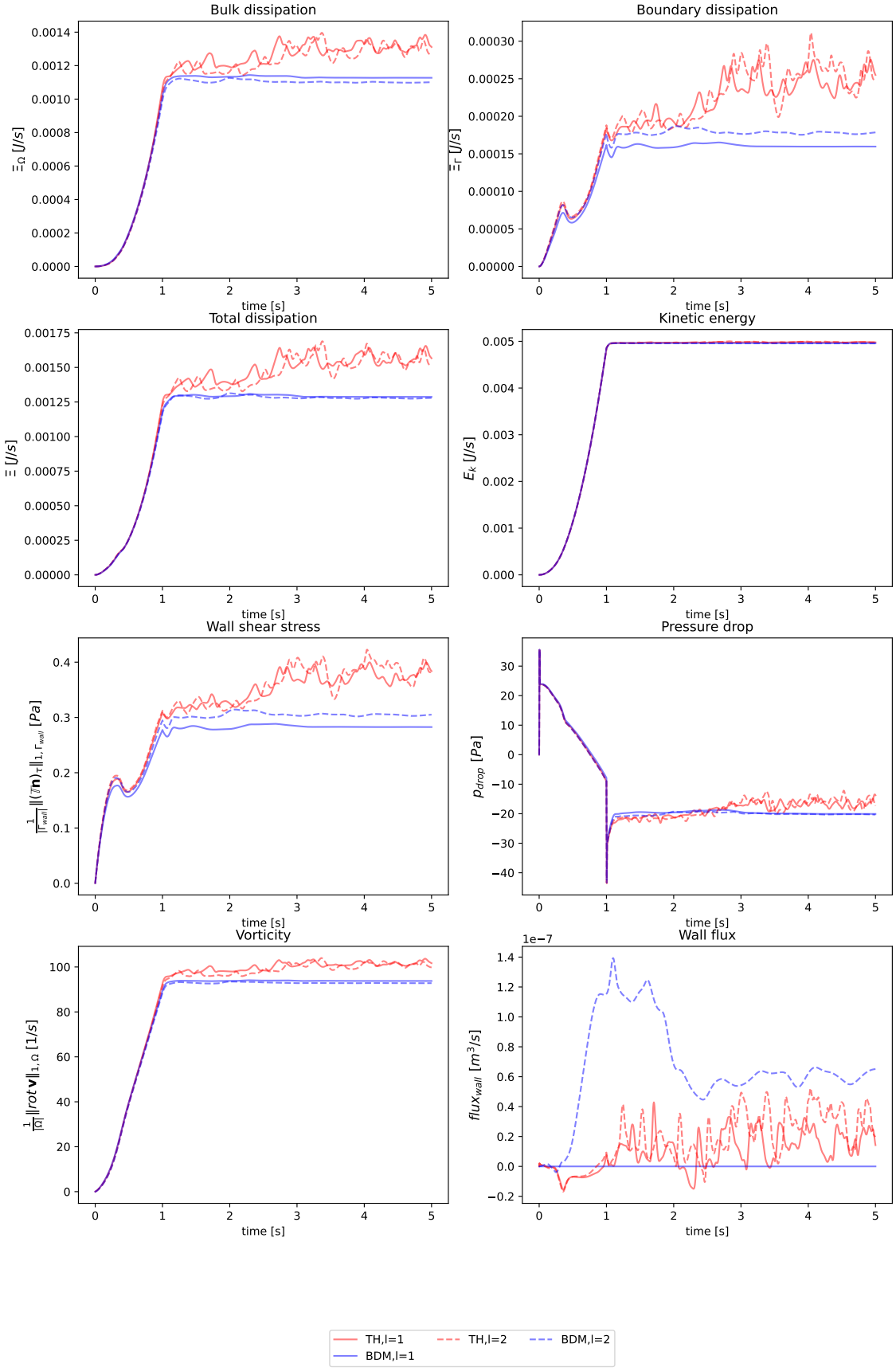

Figure 4.25: Flow quantities in time $t \in [0, 5]$ s for $\theta = 0.9$, with both piecewise linear ($l = 1$) and quadratic ($l = 2$) boundary, using TH and BDM element on mesh with three sinuses.

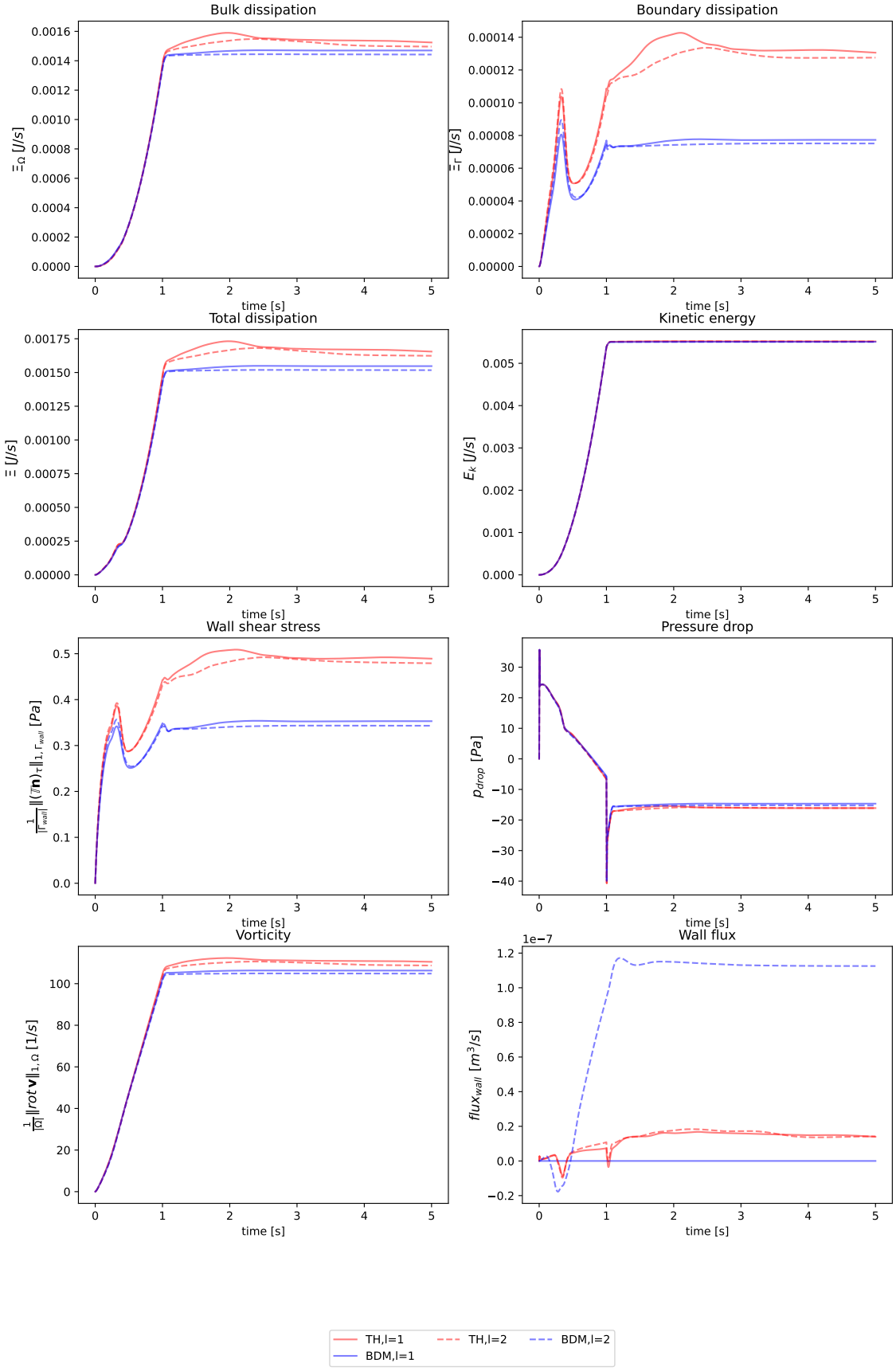

Figure 4.26: Flow quantities in time $t \in [0, 5]$ s for $\theta = 0.97$, with both piecewise linear ($l = 1$) and quadratic ($l = 2$) boundary, using TH and BDM element on mesh with three sinuses.

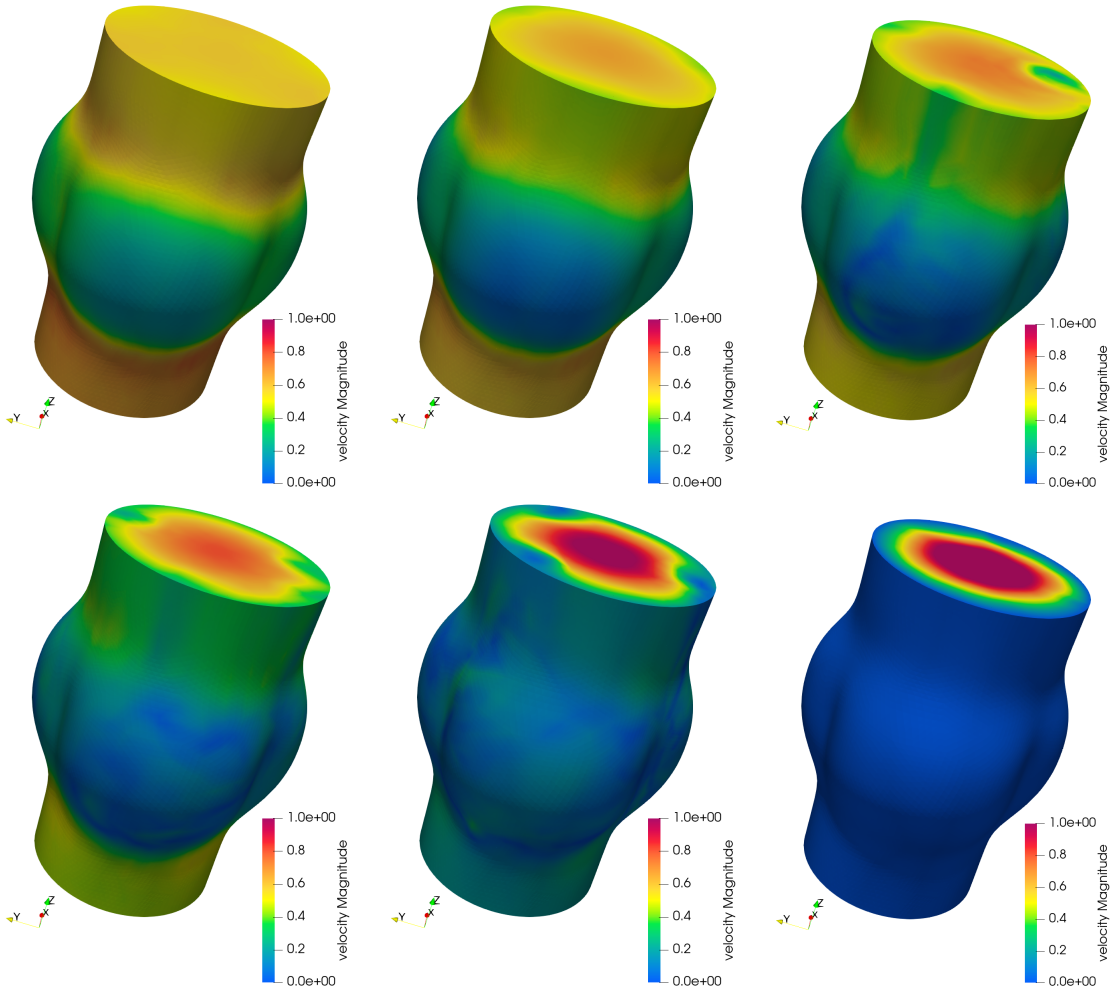

Figure 4.27: Surface velocities for flow in axially symmetric geometry, with $l = 2$, at time $t = 5$ s, using TH element, for $\theta \in \{0.0, 0.33, 0.5, 0.65, 0.9, 1\}$ respectively, on mesh with three sinuses.

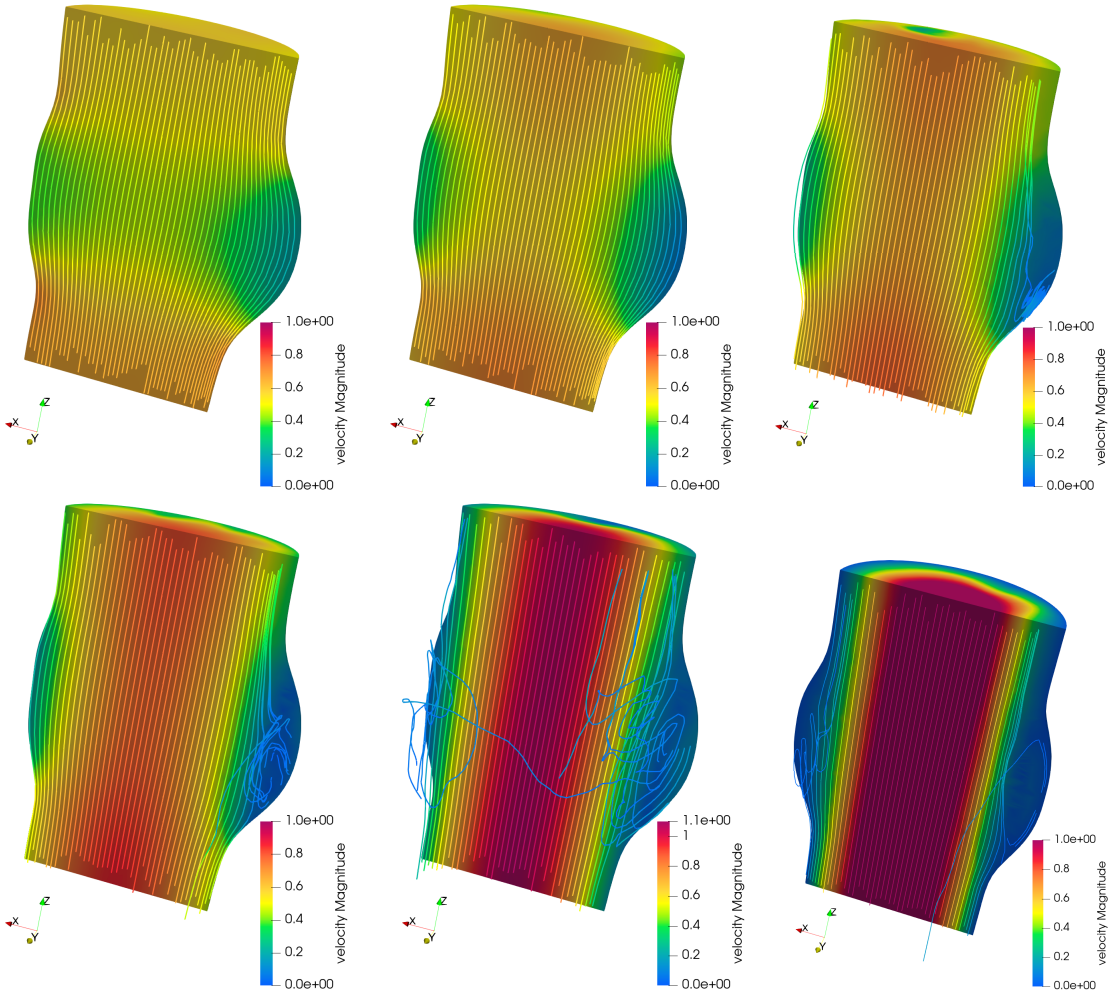

Figure 4.28: Streamlines and velocity on the cut of mesh with three sinuses, at time $t = 5$ s, with $l = 2$, using TH element, for $\theta \in \{0.0, 0.33, 0.5, 0.65, 0.9, 1\}$.

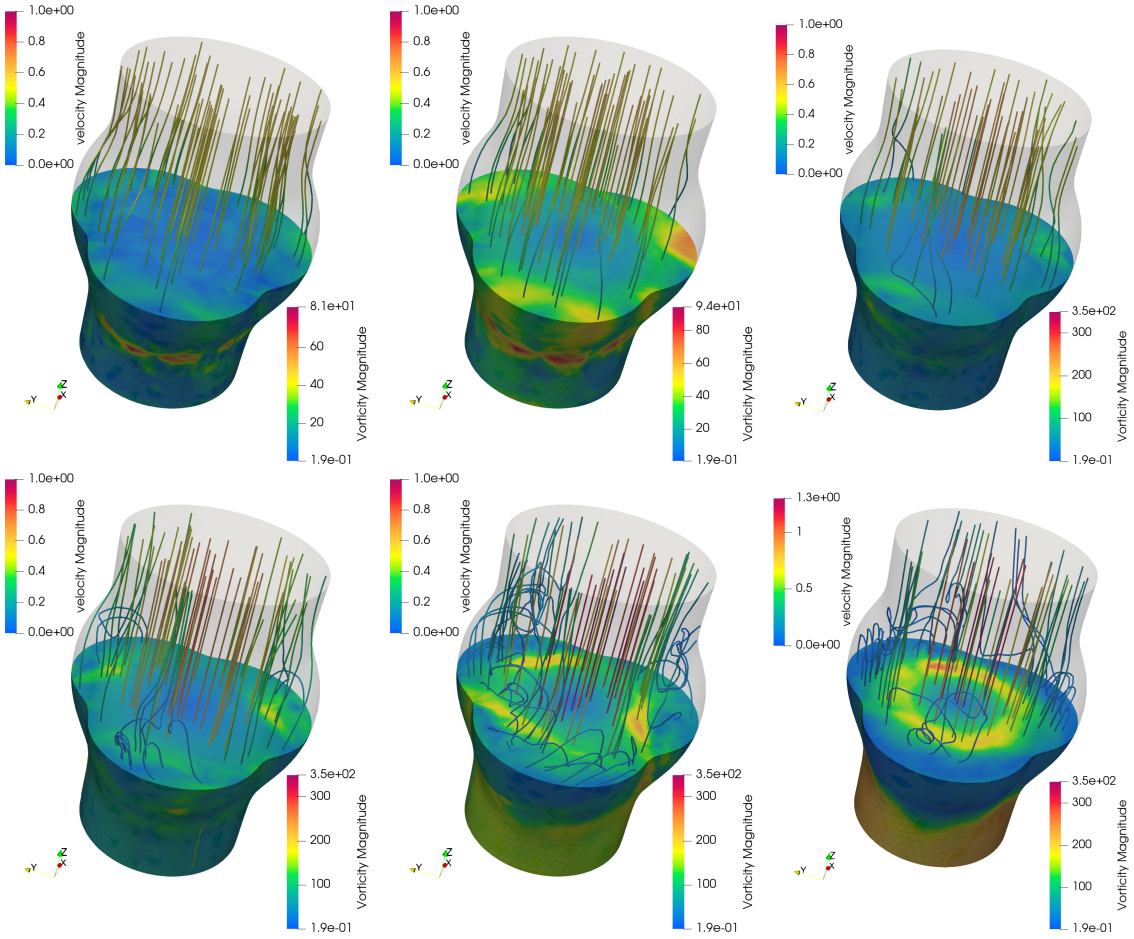

Figure 4.29: Streamlines coloured by magnitude of velocity and vorticity on the cut of mesh with three sinuses, at time $t = 5$ s, with $l = 2$, using TH element, for $\theta \in \{0.0, 0.33, 0.5, 0.65, 0.9, 1\}$.

Conclusion

We investigated unsteady three-dimensional flows in the region representing the aortic root when allowing the Navier's slip boundary condition on the wall. In the first chapter, we defined the initial-boundary-value problem and its weak formulation. In the second chapter, we rigorously proved the existence of the weak solution for our specific problem. With the weak formulation and the considered velocity spaces validated, we proceeded to the numerical and computational part.
We follow studies [9], [10] that aim to analyse flow in the aortic root, beginning with the most simplified model and progressively adding modifications, analyse their effect and deduce their significance. We developed computational codes for numerical simulations of flow in the aortic root, including three key aspects described in the third chapter. Firstly, we generated two types of geometry: an axially symmetric geometry and a more realistic geometry of the aortic root featuring three sinuses. Secondly, we approximated the boundary of the generated computational mesh by piecewise higher order polynomials rather then only piecewise linear. Thirdly, we compare results when using two discretization methods: the Taylor-Hood finite element and the $\mathbf{H}(\mathrm{div}, \Omega)$-conforming Brezzi-Douglas-Marini element. The last chapter discusses the results using relatively non-standard combinations of all the mentioned aspects together with varying Naviers's slip parameter θ on the wall.
From the benchmark problems such as Couette flow in two-dimensions and Poiseuille flow in three-dimensions, we observe that meshes with piecewise quadratic boundaries yield significantly more accurate results compared to those with piecewise linear boundaries, especially for $\mathbf{H}(\mathrm{div}, \Omega)$-conforming methods. That means that even for very fine meshes we can get two different solutions, depending on the smoothness of the boundary. The same effect occurs for flow in the aortic root, where there exists states, depending on the allowed slip on the boundary, where the solution for stationary data goes to stationary solution with piecewise quadratic boundary, but have non-stationary or even chaotic behaviour with piecewise linear boundary. Therefore we deduce that the better approximation of the boundary should be taken into account for further studies.
In case of the aortic root shape of the domain, the one with axially symmetric shape has a larger interval of allowed slip on the boundary for obtaining the stationary solutions, then the mesh with three sinuses.
Regarding the choice of the finite element discretisation, the Brezzi-Douglas-Marini finite element more likely goes to the chaotic state for piecewise linear boundary mainly for small values of θ, rather then Taylor-Hood. Moreover it has more degrees of freedom, hence the computation time is longer. However for larger values of θ the solution is not so oscillatory or chaotic as for Taylor-Hood. Nevertheless, the main reason for $\mathbf{H}(\mathrm{div}, \Omega)$-conforming methods to be considered is the possibility to develop efficient multigrid solvers. With our current method based on direct solver our computations in three dimensions are limited to relatively coarse discretizations and efficent multigrid solver could remove this limitation.

Bibliography

[1] R. A. Adams and J. J. Fournier. *Sobolev spaces*. Elsevier, 2003.

[2] P. Amestoy et al. "A Fully Asynchronous Multifrontal Solver Using Distributed Dynamic Scheduling". In: *SIAM Journal on Matrix Analysis and Applications* 23.1 (2001), pp. 15–41. DOI: 10.1137/S0895479899358194.

[3] M. Baltussen et al. "Weakly-imposed Dirichlet boundary conditions for non-Newtonian fluid flow". In: *Journal of non-newtonian fluid mechanics* 166.17-18 (2011), pp. 993–1003.

[4] J. Blechta, J. Málek, and K. R. Rajagopal. "On the Classification of Incompressible Fluids and a Mathematical Analysis of the Equations That Govern Their Motion". In: *SIAM Journal on Mathematical Analysis* 52.2 (Jan. 2020), pp. 1232–1289. ISSN: 1095-7154. DOI: 10.1137/19m1244895. URL: http://dx.doi.org/10.1137/19M1244895.

[5] D. Boffi, F. Brezzi, and M. Fortin. *Mixed Finite Element Methods and Applications*. Springer Berlin Heidelberg, 2013. ISBN: 9783642365195. DOI: 10.1007/978-3-642-36519-5. URL: http://dx.doi.org/10.1007/978-3-642-36519-5.

[6] B. Boon. "Leonardo da Vinci on atherosclerosis and the function of the sinuses of Valsalva". In: *Netherlands Heart Journal* 17.12 (Dec. 2009), pp. 496–499. ISSN: 1876-6250. DOI: 10.1007/bf03086311. URL: http://dx.doi.org/10.1007/BF03086311.

[7] C.-H. Bruneau and P. Fabrie. "New efficient boundary conditions for incompressible Navier-Stokes equations: a well-posedness result". In: *RAIRO Modél. Math. Anal. Numér.* 30.7 (1996), pp. 815–840. ISSN: 0764-583X. DOI: 10.1051/m2an/1996300708151. URL: https://doi.org/10.1051/m2an/1996300708151.

[8] E. Burman. "A Penalty-Free Nonsymmetric Nitsche-Type Method for the Weak Imposition of Boundary Conditions". In: *SIAM Journal on Numerical Analysis* 50.4 (Jan. 2012), pp. 1959–1981. ISSN: 1095-7170. DOI: 10.1137/10081784x. URL: http://dx.doi.org/10.1137/10081784X.

[9] R. Chabiniok et al. "A benchmark problem to evaluate implementational issues for three-dimensional flows of incompressible fluids subject to slip boundary conditions". In: *Applications in Engineering Science* 6 (June 2021), p. 100038. ISSN: 2666-4968. DOI: 10.1016/j.apples.2021.100038. URL: http://dx.doi.org/10.1016/j.apples.2021.100038.

[10] R. Chabiniok et al. "Three-dimensional flows of incompressible Navier–Stokes fluids in tubes containing a sinus, with varying slip conditions at the wall". In: *International Journal of Engineering Science* 180 (Oct. 2022), p. 103749. ISSN: 0020-7225. DOI: 10.1016/j.ijengsci.2022.103749. URL: http://dx.doi.org/10.1016/j.ijengsci.2022.103749.

[11] P. Ciarlet and P.-A. Raviart. “Interpolation theory over curved elements, with applications to finite element methods”. In: *Computer Methods in Applied Mechanics and Engineering* 1.2 (Aug. 1972), pp. 217–249. ISSN: 0045-7825. DOI: 10.1016/0045-7825(72)90006-0. URL: http://dx.doi.org/10.1016/0045-7825(72)90006-0.

[12] P. G. Ciarlet. *The finite element method for elliptic problems*. SIAM, 2002.

[13] P. Constantin and C. Foiaş. *Navier-Stokes equations*. University of Chicago press, 1988.

[14] L. D. Dalcin et al. “Parallel distributed computing using Python”. In: *Advances in Water Resources* 34.9 (2011). New Computational Methods and Software Tools, pp. 1124–1139. ISSN: 0309-1708. DOI: 10.1016/j.advwatres.2011.04.013.

[15] T. E. David. “Aortic Valve Sparing in Different Aortic Valve and Aortic Root Conditions”. In: *Journal of the American College of Cardiology* 68.6 (Aug. 2016), pp. 654–664. ISSN: 0735-1097. DOI: 10.1016/j.jacc.2016.04.062. URL: http://dx.doi.org/10.1016/j.jacc.2016.04.062.

[16] J. Fara et al. “Fluid–structure numerical solver for axi-symmetric flows with Navier’s slip interface condition between the viscoelastic solid and the Navier–Stokes fluid: Effects of deformable solids on the flow characteristics”. In: *Internat. J. Engrg. Sci.* 201 (2024), Paper No. 104088. ISSN: 0020-7225,1879-2197. DOI: 10.1016/j.ijengsci.2024.104088. URL: https://doi.org/10.1016/j.ijengsci.2024.104088.

[17] P. E. Farrell, L. Mitchell, and F. Wechsung. “An augmented Lagrangian preconditioner for the 3D stationary incompressible Navier-Stokes equations at high Reynolds number”. In: (2018). DOI: 10.48550/ARXIV.1810.03315. URL: https://arxiv.org/abs/1810.03315.

[18] L. P. Franca and T. J. Hughes. “Two classes of mixed finite element methods”. In: *Computer Methods in Applied Mechanics and Engineering* 69.1 (July 1988), pp. 89–129. ISSN: 0045-7825. DOI: 10.1016/0045-7825(88)90168-5. URL: http://dx.doi.org/10.1016/0045-7825(88)90168-5.

[19] C. Geuzaine and J.-F. Remacle. “Gmsh: A 3-D finite element mesh generator with built-in pre- and post-processing facilities”. In: *International Journal for Numerical Methods in Engineering* 79.11 (May 2009), pp. 1309–1331. ISSN: 1097-0207. DOI: 10.1002/nme.2579. URL: http://dx.doi.org/10.1002/nme.2579.

[20] M. Grigioni et al. “Three-dimensional Numeric Simulation of Flow Through an Aortic Bileaflet Valve in a Realistic Model of Aortic Root”. In: *ASAIO Journal* 51.3 (May 2005), pp. 176–183. ISSN: 1058-2916. DOI: 10.1097/01.mat.0000159384.36271.2c. URL: http://dx.doi.org/10.1097/01.mat.0000159384.36271.2c.

[21] D. A. Ham et al. *Firedrake User Manual*. First edition. Imperial College London et al. May 2023. DOI: 10.25561/104839.

[22] J. Hron et al. “Flows of Incompressible Fluids subject to Navier’s slip on the boundary”. In: *Computers amp; Mathematics with Applications* 56.8 (Oct. 2008), pp. 2128–2143. ISSN: 0898-1221. DOI: 10.1016/j.camwa.2008.03.058. URL: http://dx.doi.org/10.1016/j.camwa.2008.03.058.

[23] V. John. *Finite Element Methods for Incompressible Flow Problems*. Springer International Publishing, 2016. ISBN: 9783319457505. DOI: 10.1007/978-3-319-45750-5. URL: http://dx.doi.org/10.1007/978-3-319-45750-5.

[24] V. John et al. “On the Divergence Constraint in Mixed Finite Element Methods for Incompressible Flows”. In: *SIAM Review* 59.3 (Jan. 2017), pp. 492–544. ISSN: 1095-7200. DOI: 10.1137/15m1047696. URL: http://dx.doi.org/10.1137/15M1047696.

[25] M. Lanzendörfer and J. Hron. “On multiple solutions to the steady flow of incompressible fluids subject to do-nothing or constant traction boundary conditions on artificial boundaries”. In: *Journal of Mathematical Fluid Mechanics* 22.1 (2020), p. 11.

[26] J. Malék, M. Bulícek, and K. R. Rajagopal. “Navier’s slip and evolutionary Navier-Stokes-like systems with pressure and shear-rate dependent viscosity”. In: *Indiana University Mathematics Journal* 56.1 (2007), pp. 51–86. ISSN: 0022-2518. DOI: 10.1512/iumj.2007.56.2997. URL: http://dx.doi.org/10.1512/iumj.2007.56.2997.

[27] J. Málek et al. *Weak and Measure-Valued Solutions to Evolutionary PDEs*. Chapman and Hall/CRC, Aug. 2019. ISBN: 9780367810771. DOI: 10.1201/9780367810771. URL: http://dx.doi.org/10.1201/9780367810771.

[28] M. B. Mucha and P. Boguslaw. “Directional Do-Nothing Condition for the Navier–Stokes Equations”. In: *Journal of Computational Mathematics* 32.5 (June 2014), pp. 507–521. ISSN: 1991-7139. DOI: 10.4208/jcm.1405-m4347. URL: http://dx.doi.org/10.4208/jcm.1405-m4347.

[29] M. Neilan. *The Stokes complex: A review of exactly divergence–free finite element pairs for incompressible flows*. 2020. DOI: 10.1090/conm/754/15142. URL: http://dx.doi.org/10.1090/conm/754/15142.

[30] J. Nitsche. “Über ein Variationsprinzip zur Lösung von Dirichlet-Problemen bei Verwendung von Teilräumen, die keinen Randbedingungen unterworfen sind”. In: *Abhandlungen aus dem mathematischen Seminar der Universität Hamburg*. Vol. 36. Springer. 1971, pp. 9–15.

[31] M. Pokorný. *Navier-Stokes Equations*. Charles University, Prague, Czech Republic, 2022. URL: https://www.karlin.mff.cuni.cz/~pokorny/Lecture Notes/NavierandStokes_eng.pdf.

[32] H. Reul et al. “The geometry of the aortic root in health, at valve disease and after valve replacement”. In: *Journal of Biomechanics* 23.2 (Jan. 1990), pp. 181–191. ISSN: 0021-9290. DOI: 10.1016/0021-9290(90)90351-3. URL: http://dx.doi.org/10.1016/0021-9290(90)90351-3.

[33] M. E. Rognes, R. C. Kirby, and A. Logg. “Efficient Assembly of $H(\mathrm{div})$ and $H(\mathrm{curl})$ Conforming Finite Elements”. In: *SIAM Journal on Scientific Computing* 31.6 (Jan. 2010), pp. 4130–4151. ISSN: 1095-7197. DOI: 10.1137/08073901x. URL: http://dx.doi.org/10.1137/08073901X.

[34] H. Švihlová et al. “Determination of pressure data from velocity data with a view toward its application in cardiovascular mechanics. Part 1. Theoretical considerations”. In: *Internat. J. Engrg. Sci.* 105 (2016), pp. 108–127. ISSN: 0020-7225,1879-2197. DOI: 10.1016/j.ijengsci.2015.11.002. URL: https://doi.org/10.1016/j.ijengsci.2015.11.002.

[35] R. Temam. *Navier-Stokes Equations*. American Mathematical Society, Apr. 2001. ISBN: 9781470429942. DOI: 10.1090/chel/343. URL: http://dx.doi.org/10.1090/chel/343.

[36] T.-P. Tsai. *Lectures on Navier-Stokes Equations*. American Mathematical Society, Aug. 2018. ISBN: 9781470447786. DOI: 10.1090/gsm/192. URL: http://dx.doi.org/10.1090/gsm/192.

[37] M. D. de Tullio, G. Pedrizzetti, and R. Verzicco. “On the effect of aortic root geometry on the coronary entry-flow after a bileaflet mechanical heart valve implant: a numerical study”. In: *Acta Mechanica* 216.1–4 (July 2010), pp. 147–163. ISSN: 1619-6937. DOI: 10.1007/s00707-010-0361-2. URL: http://dx.doi.org/10.1007/s00707-010-0361-2.

[38] A.-V. Vuong. *Adaptive Hierarchical Isogeometric Finite Element Methods*. Vieweg Teubner Verlag, 2012. ISBN: 9783834824455. DOI: 10.1007/978-3-8348-2445-5.

[39] M. Weinreich, P.-J. Yu, and B. Trost. “Sinus of Valsalva Aneurysms: Review of the Literature and an Update on Management”. In: *Clinical Cardiology* 38.3 (Mar. 2015), pp. 185–189. ISSN: 1932-8737. DOI: 10.1002/clc.22359. URL: http://dx.doi.org/10.1002/clc.22359.

List of Figures

List of Tables